Towards embedding batteries into one-shot 3D printed smart devices

Muhammad Saqlain Iqbal

Towards embedding batteries into one-shot 3D printed smart devices

Thesis submitted for the degree of Philosophiae Doctor

Interuniversity Ph.D. Program in Industry 4.0
Politecnico di Bari

Supervisors

Prof. Engr. *Gianluca PERCOCO*

Prof. Engr. *Caterina CIMINELLI*

Referees

Prof. Cynthia Martinez Cisneros

Prof. Yonas Tadesse

Coordinator of PhD Program
Prof. Salvatore DIGIESI

Doctoral Student

Muhammad Saqlain IQBAL

2025

This doctoral research was supported by the PhD program (Industry 4.0) of Politecnico di Bari and the Università degli Studi di Bari Aldo Moro.

Dissertation submitted for the degree of *Philosophiae Doctor*
Interuniversity Ph.D. Program in Industry 4.0

Cycle:
38th (2022, November 1 – 2025, October 31)

Administrative Headquarters: Politecnico di Bari – Department of Electrical and Information Engineering

Hosting University:
Politecnico di Bari – Department of Electrical and Information Engineering (DEI)

Title: Towards embedding batteries into one-shot 3D printed smart devices

Ph.D Candidate:
Muhammad Saqlain Iqbal

Academic Discipline:
Technologies and Manufacturing Systems (Italian code: IIND-04/A, ex ING-IND/16)

Tutors:
Prof. Engr. Gianluca Percoco, Politecnico di Bari (Bari, Italy)
Prof. Engr. Caterina Ciminelli, Politecnico di Bari (Bari, Italy)

External Tutor:
Prof. Alejandro Varez, Univeristy of Carlos III Madrid (Madrid, Spain)

Coordinator:
Prof. Engr. Salvatore Digiesi, Politecnico di Bari (Bari, Italy)

External Reviewers:
Prof. Cynthia Martinez Cisneros, University of Carlos III Madrid (Madrid, Spain)

Prof. Yonas Tadesse, University of Texas at Dallas (Texas, USA)

Last version:
January 2nd, 2026

PhD Thesis

PhD Program in Industry 4.0

Department of Electrical and Information Engineering (DEI)

Politecnico di Bari

In partial fulfillment of the requirements for the degree of Doctor of Philosophy
at Politecnico di Bari

Thesis Title

TOWARDS EMBEDDING BATTERIES INTO ONE-SHOT 3D PRINTED SMART DEVICES

Written by

Muhammad Saqlain Iqbal

Defense: January 2026

Acknowledgments

This doctoral journey, conducted between 2022 and 2025, marks one of the most defining and transformative periods of my academic and personal life. Throughout these three years, I had the privilege to explore advanced concepts in additive manufacturing, materials science, and electrochemical energy storage, and to grow not only as a researcher but also as a person. The work presented in this thesis would not have been possible without the support, guidance, and encouragement of many exceptional individuals and institutions to whom I owe my deepest gratitude.

First and foremost, I would like to express my sincere appreciation to my supervisor, **Prof. Gianluca Percoco**, for his continuous guidance, mentorship, and trust throughout my doctoral studies at **Politecnico di Bari**. His expertise, intellectual generosity, and patient supervision have been instrumental in shaping both my scientific vision and professional discipline. I am profoundly grateful to **Politecnico di Bari** for granting me the opportunity and financial support to pursue this PhD and for providing an excellent research environment that made this work possible.

My heartfelt thanks also go to **Prof. Alejandro Várez** for welcoming me to the **SYPMAT Laboratory at Universidad Carlos III de Madrid** and for supervising me during my research stay in Spain. His insightful scientific discussions, continuous encouragement, and collaborative spirit made that year a period of immense learning and professional growth. I am equally thankful to all the members of the SYPMAT group for their technical assistance, kindness, and collegiality during my time in Madrid.

Special thanks are extended to **Dr. Gianni Stano**, whose technical expertise, practical guidance, and collaborative attitude proved invaluable during key experimental stages of this work. His willingness to share experience and provide support significantly facilitated the progression and reliability of the experimental results presented in this thesis.

Beyond the academic setting, I am deeply grateful to my father, **Mr. Iqbal**, and my brothers**, Waqas and Junaid**, whose unwavering love, sacrifices, and encouragement have been my

constant strength throughout this journey. Their belief in me has been the foundation upon which I could pursue and complete this demanding academic endeavor.

I also wish to remember my late mother, **Najma Bibi**, whose love, resilience, and unwavering faith in education profoundly shaped the person I am today. Although she is not here to witness this achievement, her values, prayers, and strength remain deeply embedded in every step of this journey. This work carries her memory within it, and it stands as a quiet tribute to her enduring influence on my life.

To all my colleagues, friends, and collaborators who shared this journey in Bari, Madrid, and beyond thank you for your support, constructive discussions, and the many moments of motivation and friendship that made this path memorable.

Finally, this thesis is dedicated to all those who believed in me, supported my aspirations, and stood by me with patience and understanding. Your trust and affection have been the driving forces behind every achievement contained in these pages.

Somewhere, something incredible is waiting to be known

Carl Sagan

List of Publications

This thesis presents the research outcomes developed over the three-year duration of the PhD program. Part of the work has already resulted in one peer-reviewed publication directly related to the solvent-based post-treatment methodology. The remaining results reported in this thesis represent original and unpublished research that is currently being prepared for submission to international peer-reviewed journals. Together, these studies reflect the coherent scientific contribution and experimental efforts carried out during the PhD period.

Iqbal, Muhammed Saqlain, Gianni Stano, Valentina Triminì, and Gianluca Percoco. "Low-cost method to reduce interlayer voids in material extrusion: in situ layer-by-layer solvent treatment." The International Journal of Advanced Manufacturing Technology 133, no. 11 (2024): 5333-5342.

Iqbal Muhammad Saqlain, Alejandro Várez**,** Bidhan Pandit**,** Gianluca Percoco "Carbon nanofiber–reinforced polylactic acid/$Li_4Ti_5O_{12}$ composites for one-shot 3D printing of lithium-ion battery electrodes" (Processing…)

Scientific Communications and Conferences

During the PhD program, the research activities described in this thesis were disseminated through participation in international conferences. These contributions enabled discussion of evolving research with the scientific community and supported the progressive refinement of the proposed methodologies.

Sustainable Printed Electronics Conference 2025, Thessaloniki, Greece

Oral presentation: Presentation of PhD research on "3D-printed lithium-ion batteries, with emphasis on sustainable materials and printed energy storage concepts"

XIX Conference of the European Ceramic Society (ECerS XIX), Dresden, Germany (2025)

Poster presentation on topic "CNF/PLA/LTO composites for the fabrication of 3D-printed lithium-ion batteries"

Functional Ceramics for Electronics and Energy (Electrocerámica XVII), Pamplona, Spain (2025)

Oral presentation on topic "Carbon nanofiber–polylactic acid $Li_4Ti_5O_{12}$ composite for the fabrication of 3D-printed lithium-ion batteries"

Ceramic Additive Manufacturing (AM) Summit, Berlin, Germany, *2025* (Participation)

Summary of the Thesis

The rapid expansion of smart devices, autonomous systems, and distributed electronics has intensified the demand for compact, safe, and structurally integrated energy storage solutions. Conventional lithium-ion batteries, while highly optimized at the cell level, remain largely incompatible with emerging manufacturing paradigms that seek to merge structural functionality and energy storage within a single component. In this context, additive manufacturing offers a transformative opportunity to redesign batteries not as discrete components, but as embedded, multifunctional elements fabricated in a single manufacturing step.

This doctoral thesis addresses this challenge by developing and demonstrating one-shot 3D-printed lithium-ion battery architectures, with a specific focus on lithium titanate (LTO) based composite electrodes processed through fused filament fabrication. LTO is selected as a model anode material due to its zero-strain lithiation mechanism, high operating potential (~1.55 V vs. Li/Li^+), absence of lithium dendrite formation, and exceptional cycling stability, which make it particularly attractive for structural and embedded battery concepts where safety and durability are paramount. However, its low intrinsic electronic conductivity and moderate theoretical capacity (175 $mAh.g^{-1}$) impose significant challenges for direct integration into 3D-printed architectures.

Building upon the current state of the art in printed electronics, functional polymers, and composite battery electrodes, this thesis systematically explores how materials design, composite formulation, and post-processing strategies can be combined to overcome these limitations while maintaining manufacturability. The work advances beyond conventional slurry-cast electrodes by focusing on filament-based additive manufacturing, a scalable and industry-relevant process aligned with Industry 4.0 principles.

The thesis is structured into eight chapters, encompassing a comprehensive literature review, detailed experimental methodology, and in-depth results and discussion sections.

Chapters 1 and 2 establish the scientific and technological context of the research. A critical review of lithium-ion battery materials is presented, highlighting the trade-offs between energy density, safety, and manufacturability. Particular attention is devoted to the emerging field of

3D-printed batteries, where current approaches often rely on multi-step fabrication, low active-material loading, or laboratory-scale printing techniques. The review identifies a clear research gap: the lack of robust, filament-based, one-shot printing strategies capable of producing mechanically stable and electrochemically functional battery electrodes suitable for integration into real devices.

Chapter 3 details the materials selection, composite formulation, filament extrusion, and printing protocols developed in this work. LTO is combined with thermoplastic polymer matrices and conductive carbon additives, including CNFs, to form printable composites. A key contribution of this chapter is the introduction of solvent-assisted post-treatment as a means to selectively modify interlayer bonding, porosity, and conductive pathways without compromising the overall geometry of the printed structures. This approach bridges polymer processing concepts with electrochemical electrode engineering.

Chapter 4 presents a comprehensive structure–processing–property–performance relationship analysis. Morphological and microstructural characterization reveals how printing parameters and solvent exposure influence surface roughness, pore formation, and interlayer densification. These structural features are directly correlated with electrochemical behavior, demonstrating stable lithium insertion/extraction, high Coulombic efficiency, and long-term cycling stability. Importantly, the results confirm that electrochemical performance can be achieved without excessive carbon loading, preserving the active material fraction and maintaining structural integrity.

Subsequent chapters focus on the role of conductive networks within the printed electrodes. The incorporation of CNFs is shown to significantly enhance electronic percolation and reduce charge-transfer resistance by forming interconnected, one-dimensional conductive pathways throughout the composite. Rather than maximizing conductivity alone, the thesis emphasizes a balanced design philosophy, in which electrical performance, mechanical robustness, and printability are simultaneously optimized. This perspective distinguishes the present work from conventional electrode optimization studies that neglect manufacturing constraints.

Collectively, the results demonstrate that LTO based composite electrodes can be successfully fabricated via one-shot 3D printing, yielding structures that are mechanically stable, electrochemically reliable, and compatible with embedded battery concepts. The thesis

provides design guidelines for material composition, filament formulation, printing parameters, and post-processing strategies, offering a practical pathway toward structurally integrated energy storage.

This work advances the state of the art in additive manufacturing of lithium-ion batteries by demonstrating that safety-oriented anode chemistries such as LTO can be effectively combined with scalable 3D printing processes. The outcomes of this thesis contribute to the broader vision of multifunctional, additively manufactured smart systems, and they lay the groundwork for future research into fully integrated, device-embedded energy storage solutions.

Contents

General Introduction

The global demand for energy has been on a steep upward trajectory over the past few decades, and this trend is expected to continue well into the future. Several factors contribute to this dramatic rise in energy demand, including rapid industrialization, urbanization, and population growth. As nations develop economically, their energy consumption increases, driven by the expanding needs of industries, transportation, and residential sectors. The demand for energy is also propelled by the growing consumption of electronic devices, the shift towards electric mobility, and the rise of digital technologies that require massive amounts of power to operate. Moreover, developing nations, particularly in Asia and Africa, are experiencing significant increases in energy use as they undergo urban transformation and economic growth (Gehring & Cand, 2024; Menyhart, 2024; Njema, Ouma, & Kibet, 2024; Paraschiv, Paraschiv, & Alexandru, 2025).

Amidst this growing demand, the integration of energy storage systems becomes critical, especially in built environments, to ensure sustainability and efficient energy management. Researchers like Droste-Franke and colleagues (Akinyele & Rayudu, 2014) have highlighted the urgent need for proposals that create synergies between energy supply and demand, emphasizing the importance of energy storage in mitigating the economic and environmental impacts of rising energy demand. Weather-dependent renewable energy sources, such as solar and wind, present a unique challenge, as they require energy storage solutions to capture excess energy during high-generation periods for use during low- or no-generation times. This approach enhances the reliability and efficiency of renewable energy integration into the grid, while reducing the effects of intermittent supply. Additionally, energy storage systems offer the flexibility needed for ancillary services in electricity supply and demand networks, improving grid resilience by smoothing fluctuations, responding to sudden power outages or surges, and stabilizing the overall energy supply (Allehyani, 2025; Carnegie, Gotham, Nderitu, & Preckel, 2013; Islam et al., 2024; Mayyas, Chadly, Amer, & Azar, 2022). Thus, energy storage plays a crucial role in ensuring that renewable energy is maximized and that the grid remains stable and resilient amidst increasing global energy consumption.

According to the International Energy Agency (IEA), global energy demand is projected to increase by nearly 25% between 2020 and 2040, with the majority of the growth expected in developing countries. As populations rise and new industrial sectors emerge, the need forenergy to power homes, factories, transportation, and services becomes more acute. Urbanization, in particular, plays a key role in this demand surge, as cities consume vast amounts of energy for transportation, infrastructure, and public services. By 2030, nearly 60% of the world's population is expected to live in urban areas, significantly increasing energy consumption in these regions (Ghasemian et al., 2024; Vandaele & Porter, 2015).

In parallel with this demand growth, there is a strong push for energy transition strategies aimed at mitigating the environmental impact of conventional energy systems. The global consensus on the need for reducing carbon emissions to combat climate change has led to a significant shift from fossil-fuel-based energy sources to renewable sources such as solar, wind, and hydropower. These renewable sources, while abundant and environmentally friendly, have their own challenges chief among them being their intermittent nature. Renewable energy generation, particularly solar and wind, can be unpredictable and geographically specific, posing significant challenges to grid stability and energy availability. This challenge has propelled the development and adoption of energy storage systems (ESS) to address the gaps created by these intermittent energy sources. Energy storage technologies are essential to ensure a consistent and reliable energy supply, allowing excess energy generated during peak production times (such as sunny or windy days) to be stored for later use, particularly during periods of low renewable energy generation. These systems also play a crucial role in improving grid stability, facilitating the integration of renewable energy, and enabling energy conservation at the consumer level. The growing reliance on renewable energy sources makes energy storage an indispensable component of the modern energy infrastructure (Admase, Asrade, & Fanta, 2025; Amir et al., 2023; De Carne et al., 2024).

The global energy storage systems market is rapidly expanding, and it is expected to reach a market size of USD 738 billion by 2034, growing from USD 184 billion in 2024. This represents a compound annual growth rate (CAGR) of 14.9% from 2025 to 2034. The increasing adoption of renewable energy technologies, government incentives, and the need for more resilient energy grids are driving this growth. Energy storage systems, which include

technologies such as batteries, thermal storage, pumped hydro, and mechanical storage systems, are becoming essential for balancing energy supply and demand, especially as more regions integrate renewable energy into their grids. These technologies not only provide solutions for intermittent power supply but also enhance the ability to meet peak demand, reduce energy wastage, and lower operational costs across multiple sectors (Market.Us, 2025).

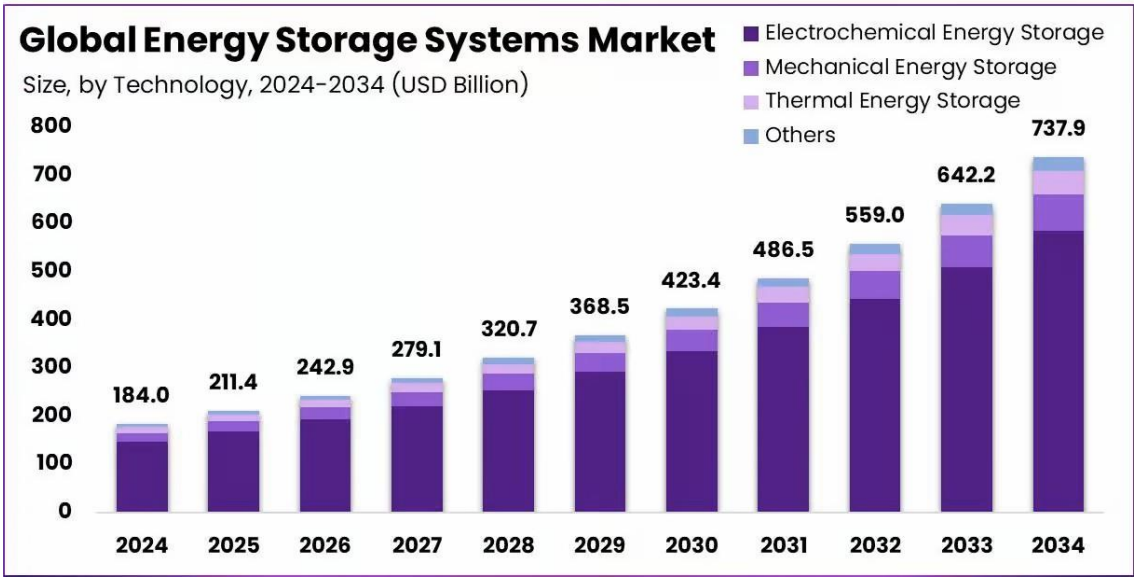

Figure I. Projected Growth of the Global Energy Storage Systems Market (Market.Us, 2025).

Energy storage devices, particularly lithium-ion batteries (LIBs), have emerged as key components in facilitating the effective utilization of renewable energy. LIBs are crucial not only for storing energy from intermittent sources like solar and wind but also for enabling the transition to electrified transportation systems, such as electric vehicles, which are seen as a viable solution to reduce carbon emissions from the transportation sector (Asamoah et al., 2024; Audu, Mafo, Jegede, Tarasenko, & Kozak, 2025; Thermtest., 2024). However, to fully realize the potential of lithium-ion technology and its widespread adoption, it is essential to address the challenges posed by current battery materials, particularly in terms of energy density, safety, cycle life, and cost. As such, there is an increasing need for the discovery and development of novel materials that can enhance the performance of energy storage devices, making them more efficient, durable, and environmentally friendly.

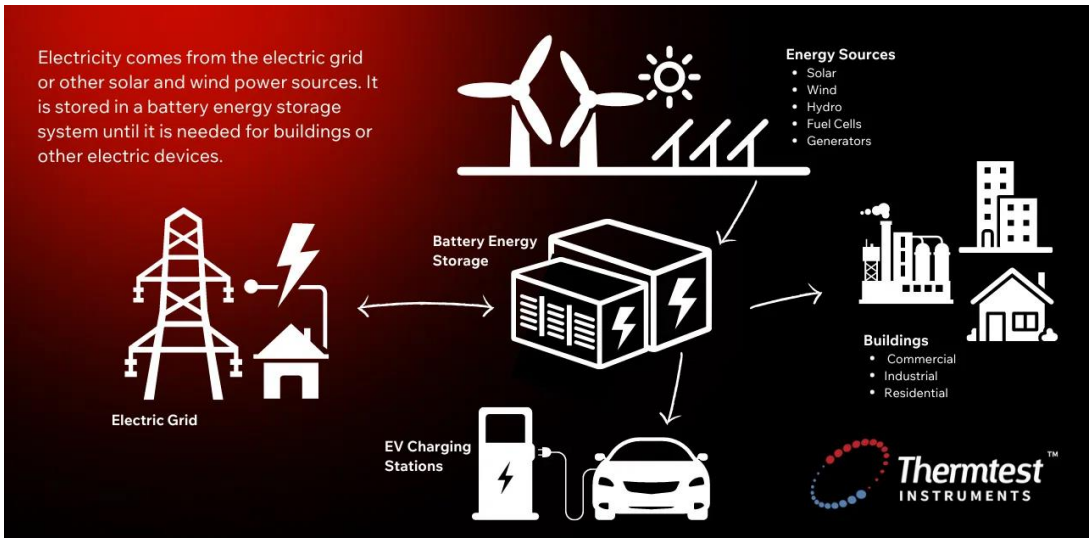

Figure II. Schematic representation illustrating the flow and utilization of stored energy within a renewable energy system (Thermtest., 2024).

A promising solution lies in the exploration of advanced anode materials for LIBs. Traditional graphite-based anodes, while widely used, have limitations in terms of energy density and rate capability, which restrict their performance in high-demand applications such as EVs and large-scale energy storage systems. Consequently, there has been a growing interest in alternative anode materials, such as lithium titanate oxide (LTO), which offers superior stability and safety characteristics compared to graphite but suffers from lower conductivity. To overcome this limitation, the incorporation of conductive additives, such as advance carbon additives has been proposed as a means to enhance the conductivity of LTO-based anodes, thereby improving their electrochemical performance (Feng et al., 2025; X. Han, Ouyang, Lu, & Li, 2014; Koech, Mwandila, Mulolani, & Mwaanga, 2025)

In portable electronics, LIBs have revolutionized the design and functionality of modern devices such as smartphones, laptops, medical implants, and unmanned aerial systems. Their high gravimetric and volumetric energy densities allow these devices to be smaller, lighter, and more efficient, while maintaining prolonged operational time between charges. Furthermore their low self-discharge rate ensures that stored energy remains stable even when

devices are idle for extended periods, supporting the growing demand for constant connectivity and mobility in a digital society. Continuous innovations in electrode chemistry and electrolyte formulations have also improved safety, charge retention, and performance reliability in compact form factors a critical factor in miniaturized technologies (Ghafari, Bayat, Akbari, & Yeklangi, 2023; Parvizi, Jalilian, Amidi, Zangeneh, & Riba, 2025).

In the EV sector, LiB have become the cornerstone of global electrification efforts. The shift from internal combustion engines to battery-driven propulsion systems is largely enabled by the superior power density and rechargeability of LIBs. Their ability to deliver high bursts of energy allows rapid acceleration, while their deep-discharge tolerance extends vehicle range without compromising longevity. LIB technology also supports vehicle-to-grid (V2G) and smart charging capabilities, transforming EVs from mere transportation devices into mobile energy assets that can stabilize and supplement the electrical grid. The ongoing evolution of cell chemistry from nickel manganese–cobalt (NMC) to lithium iron phosphate (LFP) and emerging solid-state designs continues to enhance energy output, reduce charging times, and improve safety standards, paving the way for widespread electric mobility adoption (Hasan et al., 2025; Mojumder, Ahmed Antara, Hasanuzzaman, Alamri, & Alsharef, 2022; Sang, Duong, Zhou, & Arranz, 2024). Within the domain of renewable energy storage, LIBs provide a critical link between intermittent energy sources and consistent power supply. Solar and wind systems inherently produce fluctuating outputs that do not always align with real-time demand. LIB-based battery energy storage systems (BESS) mitigate this challenge by storing surplus energy generated during peak production and discharging it when generation is low or demand spikes. Their fast response time and high round-trip efficiency make them ideal for grid stabilization, frequency regulation, and backup services. Furthermore, their scalability and modularity allow deployment across diverse applications from residential solar storage systems to utility-scale renewable energy plants contributing significantly to grid resilience, carbon reduction, and energy democratization (Eroğlu & Kurtuluş, 2025; Q. Zhang, Soham, Liang, & Wan, 2025).

Beyond their direct technical functions, LiB embody the global transition toward a decarbonized, electrified future. Their integration into portable technologies, transportation networks, and renewable infrastructures illustrates their role as both an enabler of innovation

and a driver of sustainability. As research advances toward next-generation LIB incorporating solid-state electrolytes, silicon- or lithium-metal anodes, and recyclable materials, the technology is poised to deliver even higher performance, safety, and environmental compatibility. Thus, LIBs not only underpin present-day energy systems but also chart the course toward a cleaner and more efficient energy future (Heath, Ravikumar, Hansen, & Kupets, 2022; Ngoy et al., 2025; Schichtel et al., 2022)

Chapter 1.

Literature review

Chapter 1. State of the art review on Lithium Ion batteries

1.1. Role of the Anode in Lithium-Ion Batteries

The anode plays a decisive role in defining the electrochemical performance, safety, and lifespan of LIBs. Its ability to reversibly host lithium ions determines the cell's specific capacity, rate capability, and overall energy density. Among all potential materials, graphite has been the most commercially successful and widely adopted anode material since its introduction in the early 1990s. This prominence stems from its low lithiation potential (≈ 0.1–0.2 V vs. Li^+/Li), high reversibility, chemical stability, low cost, and mechanical robustness. The intercalation mechanism of graphite allows lithium ions to be inserted between its graphene layers during charging and removed during discharging, offering a stable and predictable electrochemical process. However, as the demand for higher-performing and energy-dense batteries continues to rise driven by electric vehicles, portable electronics, and large-scale renewable energy storage the inherent limitations of graphite are becoming increasingly evident (Nandihalli, 2024; Yingying Wang et al., 2025).

1.2. Limitations of Graphite Anodes

The theoretical specific capacity of graphite is approximately 372 mAh/g**,** which imposes a ceiling on the energy density achievable by current LiB (Joy et al., 2022). This limitation is particularly critical for applications requiring extended driving ranges or high-energy storage capacity, where graphite's relatively modest capacity restricts the full potential of next-generation cells. Moreover, graphite's intercalation mechanism, though stable, relies on the diffusion of lithium ions between tightly packed carbon layers. This diffusion process is inherently slow and can become a bottleneck during high-rate charging and discharging (AlJaber, AlShammari, & AlOtaibi, 2025; Zhong, Weng, Wang, Zhan, & Wang, 2023). When the charging rate (C-rate) exceeds the intrinsic diffusion rate of Li^+ ions into the graphite lattice, a significant concentration gradient develops across the anode–electrolyte interface. Under these non-equilibrium conditions, the local potential at the graphite surface can transiently drop below 0 V versus Li^+/Li, triggering lithium plating on the anode surface instead of intercalation into graphite layers. The metallic lithium deposits that form on the surface can nucleate and grow as dendritic structures, which may penetrate the separator,

leading to internal short circuits and potentially inducing thermal runaway or catastrophic cell failure. Beyond safety concerns, the plating process also consumes active lithium inventory, as the deposited Lithium is often electrochemically irreversible, resulting in capacity fading, reduced Coulombic efficiency (CE), and shortened cycle life during repeated charge–discharge cycles. In particular, lithium plating is exacerbated under high state-of-charge (SOC), low-temperature operation, or fast-charging conditions, where limited Li^+ diffusion within the graphite lattice and blocked transport pathways promote surface accumulation of Li^+ near the interface (Figure 1.1A-E).

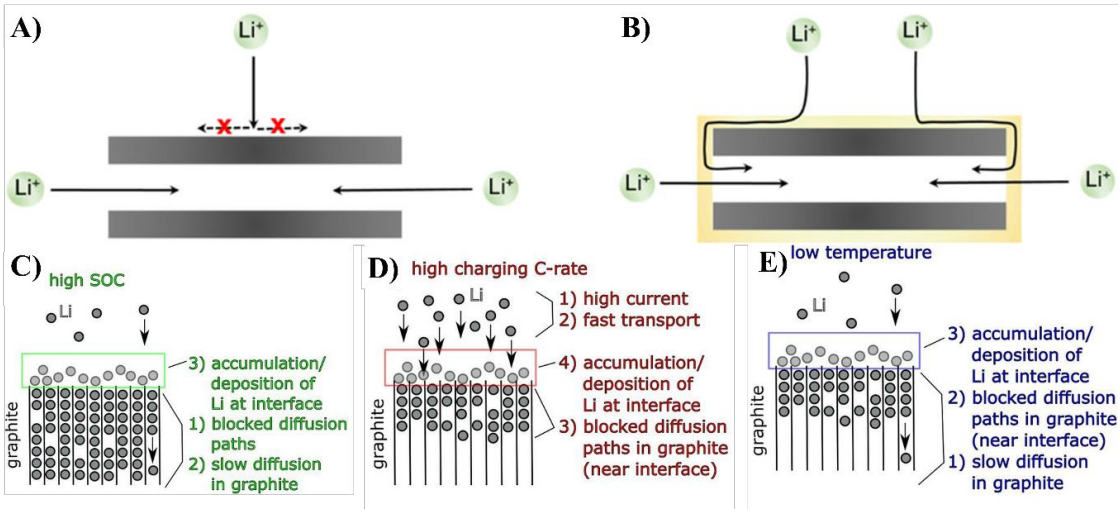

Figure 1.1. Schematic illustration of lithium plating phenomena under different electrochemical conditions. (A) At low charging rates, Li^+ ions diffuse uniformly into the graphite lattice without surface accumulation, (B) When the charging rate surpasses the Li^+ diffusion rate, surface deposition of metallic Li occurs, [A,B] reproduced with permission (Cai et al., 2020) (C–E) Mechanistic visualization of Li^+ behavior under (C) high SOC, (D) high C-rate, and (E) low temperature, showing progressive accumulation and deposition of lithium near the graphite interface due to blocked diffusion paths reproduced with permission (Waldmann et al., 2016).

1.3. Solid Electrolyte Interphase (SEI) Formation and Growth Mechanisms

Another fundamental issue associated with graphite anodes is the formation and stability of the solid electrolyte interphase (SEI). The SEI is a passivation layer that forms on the anode

surface during initial cycling due to electrolyte decomposition. Although a stable SEI is necessary for preventing continuous electrolyte breakdown, it is also fragile and prone to cracking during repeated lithiation and delithiation. Every time the SEI ruptures, fresh electrolyte decomposes to reform it, consuming active lithium ions and leading to irreversible capacity loss. This process contributes to a gradual decline in CE and accelerates electrode degradation. At elevated temperatures or during rapid charging, the SEI layer becomes increasingly unstable, leading to gas evolution, impedance rise, and reduced battery performance. Furthermore, despite graphite's relatively low volumetric change (~10%) during cycling, mechanical stress can accumulate within particles under high-rate or long-term operation, causing microcracks that further destabilize the SEI and reduce electrical contact between particles. Kamyab [78] developed a mixed-mode SEI growth model integrating solvent reduction kinetics and solvent diffusion across the SEI layer (Figure 1.2A). Numerical analysis allowed prediction of solvent concentration, SEI thickness, and capacity fade, with model fitting showing strong agreement with experimental data under constant-voltage conditions (Kamyab, Weidner, & White, 2019) Similarly, Wagner-Henke et al. [79] employed a combined kMC–continuum framework to simulate early SEI formation on lithium metal in carbonate electrolytes (**Figure 1.2B**), revealing a LiF-rich SEI above Li_2CO_3/Li and highlighting the influence of salt concentration on SEI morphology and passivation rate (Wagner-Henke et al., 2023).

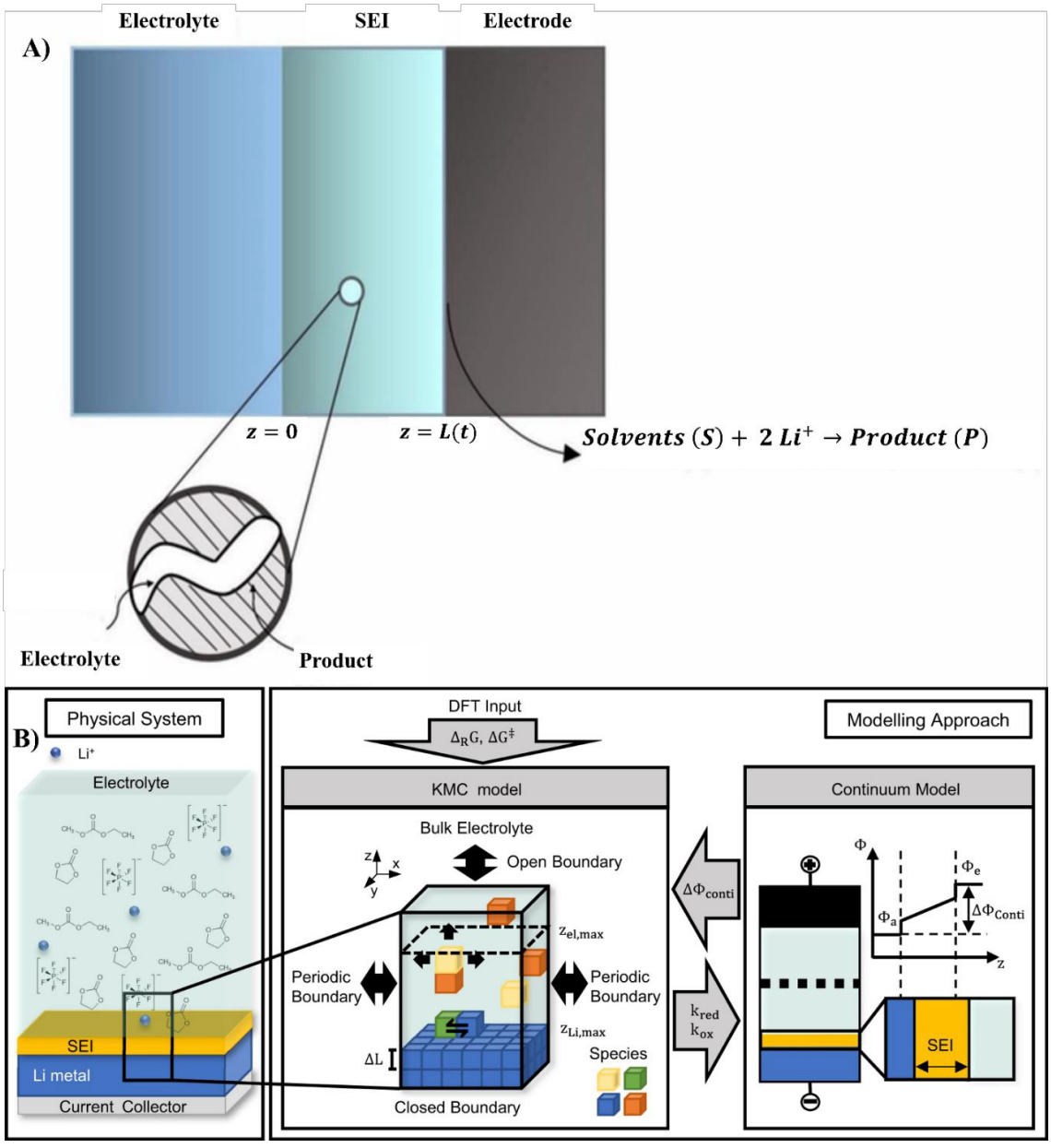

Figure 1.2. A) Schematic illustration of the SEI formation process at the SEI/electrode interface. Solvent molecules (S) and lithium ions from the electrolyte diffuse through the porous SEI layer and react with electrons at the electrode surface, generating insoluble decomposition products (P) that contribute to SEI growth. Reproduced with permission from the original source (Kamyab et al., 2019). B) Conceptual schematic illustrating the modeled mechanism of SEI formation on a lithium metal surface. Reproduced with permission from the original source (Wagner-Henke et al., 2023).

1.4. Strategies to Enhance Graphite Performance and Explore Alternative Anode Materials

To address these challenges, researchers have proposed numerous approaches to enhance the electrochemical performance of graphite or to identify alternative anode materials capable of higher energy storage. Modifications such as surface etching (Gallego et al., 2014; Y. Han, Chandio, Soni, Ciucci, & Cheong, 2025; Kim & Shim, 2020), chemical doping (Markey et al., 2020; Yang et al., 2021; H. Yu, Chen, Zhou, Wang, & Qiu, 2023), and nanostructuring (Ghanooni Ahmadabadi, Rahman, & Chen, 2023; Yumei Wang, Song, Huang, Lang, & Zhang, 2023) have been used to shorten lithium-ion diffusion paths and improve electrode kinetics. Expanding the interlayer spacing of graphite can facilitate faster ion transport, while coatings and artificial SEI layers can stabilize the electrode–electrolyte interface. Nonetheless, these modifications often provide incremental improvements rather than breakthroughs. Consequently, the focus of current research has shifted toward developing new anode materials with substantially higher specific capacities and improved kinetic behavior.

Silicon has emerged as one of the most promising alternatives due to its extremely high theoretical specific capacity of about 4200 mAh g^{-1}**,** nearly ten times that of graphite (Cui, 2021). However, silicon's practical application faces major obstacles, particularly its significant volumetric expansion of around 280–300% during lithiation. This expansion induces severe mechanical strain, leading to pulverization of the electrode, repeated SEI breakdown, and rapid capacity fading (Ko, Chae, & Cho, 2015; H. Li et al., 2023). Efforts to mitigate these issues include designing silicon–graphite composites, which combine the stability of graphite with the high energy capacity of silicon, thereby achieving a balance between performance and durability. These composite electrodes can partially suppress volume expansion, distribute mechanical stress, and enhance electronic conductivity, but the optimization of silicon content and binder elasticity remains a challenge (Jang & Kwon, 2025; Otero, Heim, Leiva, Wagner, & Friedrich, 2018). Beyond silicon-based systems, other advanced materials are being explored, including conversion-type anodes such as metal oxides and sulfides (Simpson, Redor, Titirici, & Lander, 2025; Tomboc, Wang, Wang, Li, & Lee, 2021; Z. Yan et al., 2025), and alloying-type anodes (Peng et al., 2022) based on tin, germanium, and aluminum. While these materials offer higher theoretical capacities, they also

suffer from drawbacks such as large voltage hysteresis, poor electrical conductivity, and structural degradation caused by significant volume fluctuations during cycling. In contrast, intercalation-type oxides like $Li_4Ti_5O_{12}$ and niobium-based compounds provide exceptional stability, high-rate capability, and enhanced safety; however, their higher operating potentials reduce the overall energy density of the battery, see the figure 1.3.

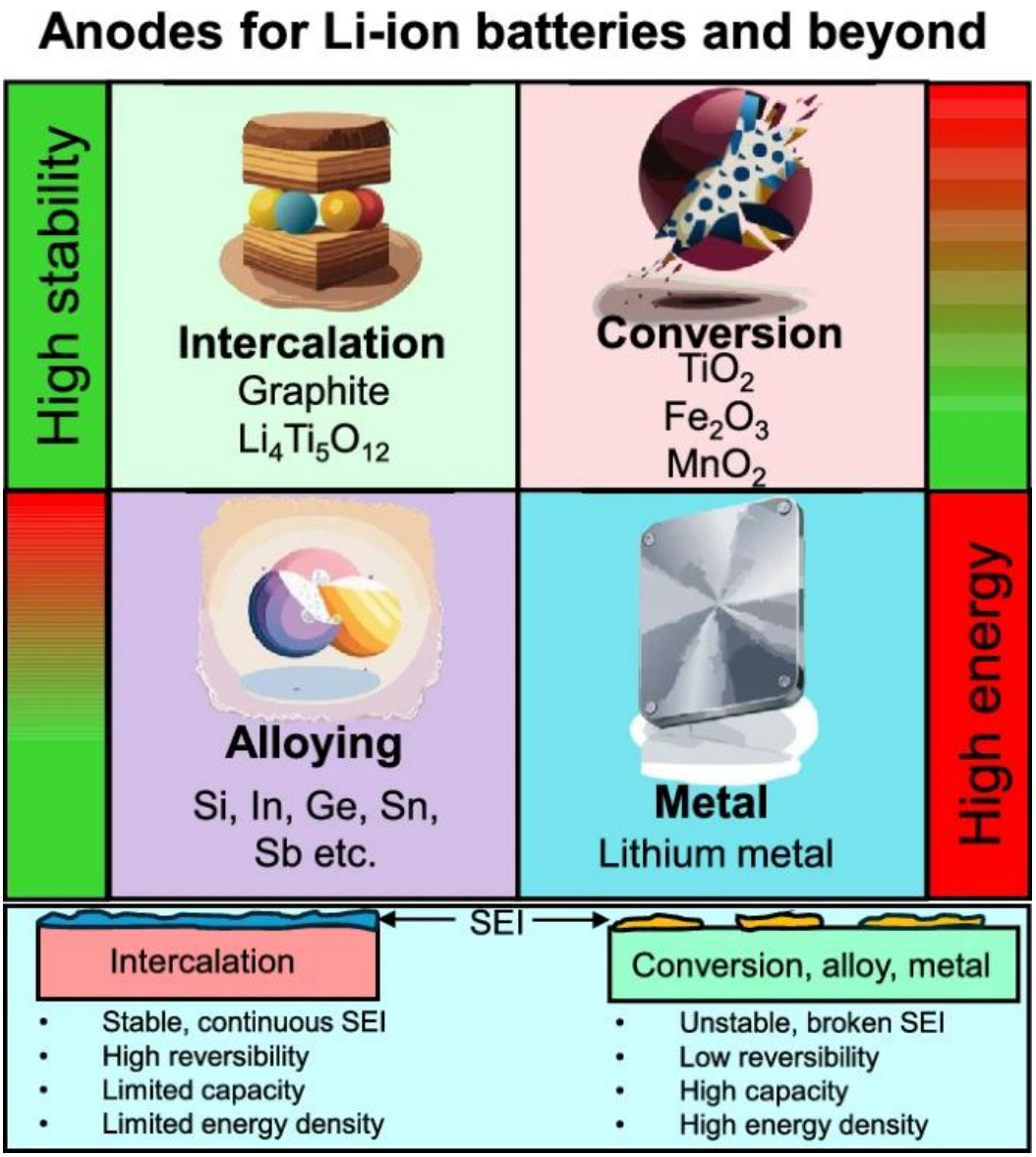

Figure 1.3. Comparison of major anode types for Li-ion batteries and beyond, highlighting their relative energy density, stability, and SEI characteristics, reprinted with permission (Rahman, Nisar, Abouimrane, Belharouak, & Amin, 2025).

Ultimately, the performance and longevity of LiB are intrinsically governed by the design, composition, and interfacial chemistry of the anode material. Graphite's dominance in commercial batteries is well deserved due to its stability, efficiency, and cost-effectiveness, but its energy density ceiling and rate limitations underscore the need for next-generation anodes. The transition toward high-capacity anode systems must therefore be approached through multi-dimensional optimization combining materials innovation, microstructural engineering, electrolyte formulation, and interfacial control. Only through such integrated strategies can future lithium-ion batteries achieve the high energy, fast charging, and long cycling performance required for advanced technologies and sustainable energy systems (W. Zhao, Zhao, Wu, Li, & Zhang, 2024).

1.5. Crystal Structure and Electrochemical Mechanism of LTO

LTO is a spinel-type compound with the empirical formula $Li_4Ti_5O_{12}$, and its crystal chemistry underpins its exceptional stability and unique electrochemical behavior. Structurally, it crystallizes in a cubic spinel lattice belonging to the space group $Fd\bar{3}m$ (No. 227), where lithium, titanium, and oxygen occupy well-defined crystallographic sites that create a robust three-dimensional framework for lithium-ion diffusion (Kia et al., 2023). The unit-cell parameter is approximately a = 8.359 Å**,** and the atomic arrangement can be described using Wyckoff positions as follows:

$$[\mathbf{Li_3}]_{\mathbf{8a}}[]_{\mathbf{16c}}[\mathbf{Ti_{5/3}Li_{1/3}}]_{\mathbf{16d}}[\mathbf{O_{12}}]_{\mathbf{32e}} \text{ ……..(1)}$$

Here (1), Li^+ ions occupy the 8a tetrahedral sites, Ti^{4+}ions mainly occupy the 16d octahedral sites, and O^{2-} anions form a close-packed cubic sublattice at the 32e sites. The vacant 16c octahedral positions act as interstitial sites that can accommodate additional lithium during lithiation. The resulting three-dimensional network provides interconnected pathways for Li^+ migration between adjacent interstitial sites, which is the basis of LTO's highly reversible electrochemical activity (Kitta et al., 2014).

1.6. Lattice Transition during Lithiation and Delithiation

The charge–discharge reaction of LTO involves a topotactic transformation between two closely related spinel phases, $Li_4Ti_5O_{12}$ and $Li_7T_5O_{12}$, without any phase collapse or long-range structural distortion. The overall electrochemical reaction can be expressed as:

$$\mathbf{Li_4Ti_5O_{12} + 3Li^+ + 3}\boldsymbol{e^-} \leftrightarrow \mathbf{Li_7Ti_5O_{12}} \ldots\ldots \mathbf{(2)}$$

In this reaction (2), three lithium ions per formula unit are intercalated into the crystal lattice, accompanied by the partial reduction of Ti^{4+} to Ti^{3+}. Structurally, Li^+ ions migrate from the tetrahedral 8a sites in the spinel phase to the octahedral 16c sites in the rock-salt phase, while the Ti-occupied 16d framework remains intact as shown in the equation (3). This well-defined topotactic transformation stores exactly three electrons per formula unit, which, when normalized to the molar mass of $Li_4Ti_5O_{12}$, yields the theoretical capacity of 175 mA h g^{-1}. A distinctive feature of this reaction is its negligible lattice strain, with a volume change of less than 1% during the spinel–rock-salt phase transition. This "zero-strain" characteristic is directly responsible for the exceptional structural reversibility and long cycle life of LTO anodes, even under high-rate charge–discharge conditions. However, the same crystallographic stability inherently limits the number of electrons that can be reversibly transferred, thereby constraining the theoretical capacity compared to alloying-type anodes such as silicon or lithium metal.

As emphasized in recent state-of-the-art studies includes the moderate theoretical capacity of LTO should therefore be regarded as an intrinsic materials limitation rooted in its robust spinel framework rather than a kinetic or morphological deficiency. Consequently, current research efforts have shifted toward strategies such as surface engineering, heterogeneous phase control, and controlled overlithiation to partially surpass the conventional 175 mAh.g^{-1} limit, albeit often at the expense of reversibility or structural stability (Shuting Fu et al., 2021; Shen, Uchaker, Zhang, & Cao, 2012).

The corresponding movement can be schematically represented as:

$$\mathbf{[Li]_{8a}\,[Li_{1/3}Ti_{5/3}]_{16d}[\square]_{16c}} \xrightarrow{\textbf{Lithiation}} \mathbf{[\square]_{8a}[Li^{1/3}Ti_{5/3}]_{16d}[Li_3]_{16c}} \ldots\ldots\ldots \mathbf{(3)}$$

This topotactic two-phase reaction (3) proceeds without structural collapse, preserving the cubic spinel framework and ensuring excellent cycling stability due to negligible volume change during lithiation and delithiation (Christian M. Julien & Alain Mauger, 2024).

This results in the rock-salt-type phase $Li_7Ti_5O_{12}$ in which all octahedral sites (16c + 16d) become fully occupied by cations. Because both the parent and lithiated phases share nearly identical cubic symmetry and lattice constants, the unit-cell expansion is less than 0.2 %**,** as reported by Kang et al. (2020) and confirmed by neutron diffraction and in-situ XRD studies. This minute lattice change is the physical basis for the so-called "zero-strain" property, which prevents particle pulverization, maintains electrode integrity, and enables outstanding cycle life often exceeding 10,000 cycles at minimal capacity loss.

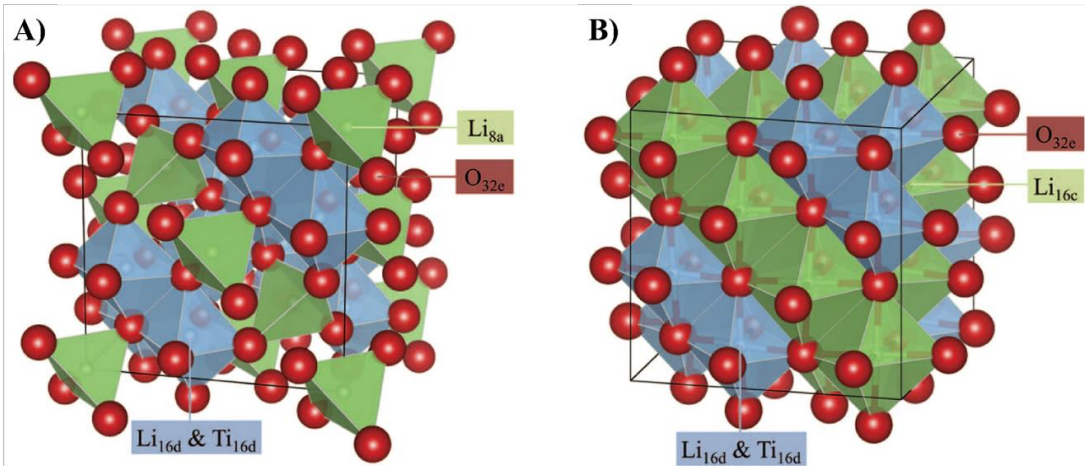

Figure 1.4. Structural evolution of the $Li_4Ti_5O_{12}$ spinel during lithiation: (a) delithiated $Li_4Ti_5O_{12}$ showing Li^+ at 8a sites and vacant 16c sites; (b) lithiated $Li_7Ti_5O_{12}$ with Li^+ fully occupying 16c octahedral sites, forming a rock-salt-like configuration. Reprinted with permission from (Tsai, Hsu, & Lin, 2014).

1.7. Electronic Structure and Redox Mechanism

The electrochemical activity of LTO is governed by the Ti^{4+}/Ti^{3+} redox couple. During lithiation, each inserted Li^+ is charge-compensated by an electron that reduces Ti^{4+} to Ti^{3+}, as described by:

$$Ti^{4+} + e^{-} \rightarrow Ti^{3+} \ldots\ldots\ldots (4)$$

First-principles density functional theory (DFT) analyses indicate that the conduction band of $Li_4Ti_5O_{12}$ is predominantly derived from Ti 3d t_2g orbitals, whereas the valence band is mainly contributed by O 2p states. Upon lithiation, the inserted lithium donates electrons to Ti 3d orbitals, forming localized Ti^{3+} centers that mediate electron transport through a small-polaron hopping mechanism. Because of the relatively wide bandgap (≈ 2.0–2.3 eV), the intrinsic electronic conductivity remains extremely low (~10^{-13} S cm^{-1}). This limited electronic mobility accounts for the poor high-rate performance of pristine LTO and provides the rationale for subsequent efforts involving doping and composite engineering to enhance its conductivity (Yi et al., 2012).

The redox reaction produces a distinct flat voltage plateau around 1.55 V vs Li^+/Li, as observed in galvanostatic charge–discharge curves (Figure 1.5). This plateau corresponds to a two-phase coexistence region between $Li_4Ti_5O_{12}$ and $Li_7Ti_5O_{12}$, a characteristic that ensures stable output voltage and high reversibility. Because this potential is well above the electrochemical reduction threshold of common carbonate electrolytes, it effectively suppresses electrolyte decomposition and SEI formation, enhancing overall cell safety (Kozlova, Uvarov, & Ulihin, 2022)

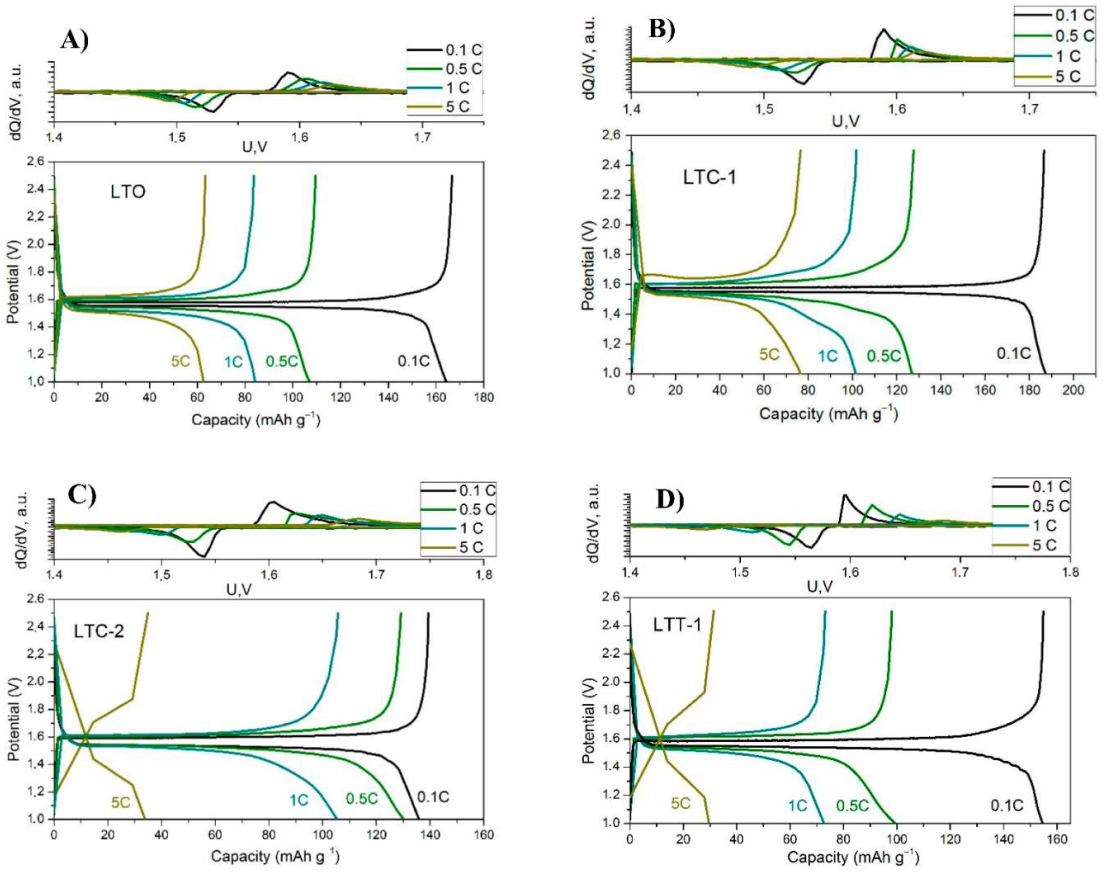

Figure 1.5. Galvanostatic charge–discharge profile of a Li/$Li_4Ti_5O_{12}$ half-cell measured at 0.1 C, showing a broad plateau around 1.55 V corresponding to the Ti^{4+}/Ti^{3+} redox transition. The inset illustrates the dQ/dV curve marking the two-phase transformation region. Reproduced with permission from Kozlova et al., Materials 15 (17), 6079 (2022) (Kozlova et al., 2022).

1.8. Lithium-Ion Diffusion Kinetics

LTO possesses a three-dimensional network of lithium-ion pathways oriented along the ⟨100⟩ and ⟨110⟩ directions of its spinel lattice. Lithium transport proceeds through successive hops between neighboring 8a and 16c sites via shared oxygen tetrahedral octahedral connections. Experimental electrochemical impedance spectroscopy and first-principles calculations consistently report an activation barrier of approximately 0.35–0.52 eV, reflecting efficient ionic migration compared with layered or olivine-type hosts. The lithium-ion diffusion coefficient (D_{li}) typically ranges from 10^{-8} to 10^{-9} cm^2 s^{-1} at room temperature, allowing for rapid insertion and extraction at practical current rates. Despite favorable ion transport, charge

transfer at the electrode is constrained by the intrinsically low electronic conductivity of the LTO framework. Enhancements through particle downsizing, conductive coatings, or aliovalent doping are therefore critical to optimize its electrochemical performance (Selvamurugan, Karthikeyan, & Karuppuchamy, 2017).

The rate performance can be described by the simplified Butler–Volmer relation for charge-transfer kinetics:

$$\boldsymbol{i = i_0\ [\exp\left(\frac{anF\eta}{RT}\right) - \exp\left(-\frac{(1-a)aF\eta}{RT}\right)]} \ldots\ldots\ldots \textbf{(5)}$$

where In the Butler–Volmer equation (5), the term $i$denotes the current density, representing the overall rate of electrochemical charge transfer across th e electrode–electrolyte interface, while i_0 corresponds to the exchange current density, which characterizes the intrinsic reaction rate under equilibrium conditions. The parameter η defines the overpotential, indicating the deviation from equilibrium potential that drives the reaction. The number of electrons involved in the redox process is expressed as n, and $F$is the Faraday constant (96,485 C mol^{-1}), linking charge and moles of electrons. R refers to the universal gas constant (8.314 J mol^{-1} K^{-1}), and T is the absolute temperature in kelvin. The coefficients $\alpha_a$and α_c represent the anodic and cathodic charge-transfer coefficients, typically ranging between 0.3 and 0.7, and they describe how the applied potential is partitioned between the forward and reverse reaction directions (de Pauli et al., 2019).

1.9. Thermodynamic and Structural Stability

The unique combination of cubic symmetry, strong Ti–O bonding, and uniform charge distribution contributes to the remarkable thermodynamic stability of LTO. Upon lithiation, the lattice parameter changes minimally from 8.3595 Å ($Li_4Ti_5O_{12}$) to 8.3598 Å ($Li_7Ti_5O_{12}$) corresponding to a mere 0.027 % unit-cell expansion. This feature eliminates the mechanical stress typically associated with repeated Li insertion, preventing electrode cracking and SEI disruption. Moreover, the high reaction onset temperature (> 300 °C) for LTO electrolyte interactions ensures that exothermic side reactions are minimized, which drastically reduces the risk of thermal runaway compared to graphite (≈ 150 °C onset) (Gu, Guo, & Liu, 2014). The enthalpy of lithiation (ΔH_1) for LTO is relatively small (~ −18 kJ/mol Li^+), implying low heat generation during cycling. This property, coupled with negligible gas

evolution, accounts for its exceptional safety record in abuse tests such as nail penetration, overcharge, and thermal shock.

1.10. Crystal-Chemical Formula Representation

From a crystallographic standpoint, the $Li_4Ti_5O_{12}$ spinel structure (6) consists of a three-dimensional framework of TiO_6 octahedra and LiO_4 tetrahedra interconnected through shared oxygen atoms. In the general spinel formula AB_2O_4, the A-site corresponds to the tetrahedral position and the B-site to the octahedral one. Accordingly, the structural formula of $Li_4Ti_5O_{12}$ can be represented as $Li[Li_{1/3}Ti_{5/3}]O_4$, or equivalently $Li^A[Li_{1/3}Ti_{5/3}]^BO_4$, where Li^+ occupies the tetrahedral (8a) sites, while Ti^{4+} and a fraction of Li^+ share the octahedral (16d) sites within the spinel lattice:

$$\boldsymbol{Li_4Ti_5O_{12}} \equiv \mathbf{Li}[\mathbf{Li}_{1/3}\boldsymbol{Ti}_{5/3}]\boldsymbol{O_4} \equiv \boldsymbol{Li^A}[\mathbf{Li}_{1/3}\boldsymbol{Ti}_{5/3}]^{\boldsymbol{B}}\boldsymbol{O_4} \qquad \text{.....(6)}$$

Thus, LTO can be considered a defect spinel where additional lithium occupies B-site octahedra, giving rise to its unique stoichiometry. The slight non-stoichiometry often observed in experimental samples $Li_{4+x}Ti_{5-x}O_{12-}\delta$ further influences its electronic and ionic transport by introducing Ti^{3+} centers and oxygen vacancies.

1.11. Visualization of Structural Integrity during Cycling

Among all known anode materials, LTO stands out for its exceptional structural stability during repeated charge–discharge cycling. The spinel lattice undergoes a highly reversible topotactic transformation to $Li_7Ti_5O_{12}$ upon lithiation without noticeable lattice distortion or phase collapse. This remarkable dimensional invariance often termed the “zero-strain” property distinguishes LTO from conventional intercalation or alloying anodes and is a key reason for its outstanding mechanical robustness, long cycle life, and intrinsic safety in high-power lithium-ion systems.

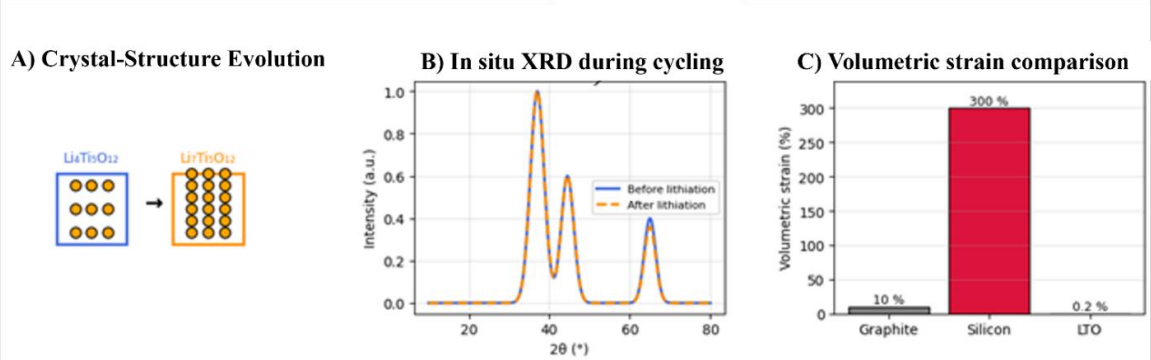

Figure 1.6. State-of-the-art visualization of the structural and mechanical integrity of spinel $Li_4Ti_5O_{12}$ during electrochemical cycling. (A) Schematic representation of the reversible phase evolution ($Li_4Ti_5O_{12} \rightarrow Li_7Ti_5O_{12}$) exhibiting negligible lattice expansion. (B) In-situ XRD profiles recorded during galvanostatic cycling, showing invariant peak positions that confirm full structural reversibility, redrawn from the published concept (H. Liu et al., 2019) (C) Comparative volumetric strain of common anodes [Graphite ≈ 10 %, Silicon ≈ 300 %, and LTO ≈ 0.2 %] highlighting the mechanical stability of the spinel framework

This Figure 1.6. underscores the key advantage of LTO's spinel network mechanical and dimensional stability. Because of this invariance, particle cracking, electrical disconnection, and SEI rupture are virtually eliminated, leading to outstanding cycle life even under harsh electrochemical conditions.

Table 1.1. Summary of the key structural, electrochemical, and transport properties of spinel $Li_4Ti_5O_{12}$, highlighting its high structural stability, moderate capacity, and superior safety characteristics compared with conventional anode materials.

Property	Symbol / Value	Significance
Crystal structure	Cubic spinel, $Fd\bar{3}m$	Three-dimensional Li^+ pathways; mechanically robust framework
Lattice parameter	$a \approx 8.359$ Å	Remains nearly constant throughout cycling
Operating potential	1.55 V vs Li^+/Li	Prevents lithium plating; enhances safety
Theoretical capacity	175 mAh g^{-1}	Moderate capacity with excellent reversibility
Volume change	< 0.2 %	"Zero-strain" lattice ensures long-term stability
Bandgap	2.0–2.3 eV	Explains low intrinsic electronic conductivity

Electronic conductivity	~10^{-13} S cm^{-1}	Main kinetic limitation
Li^+ diffusion coefficient	10^{-8}–10^{-9} cm^2/s	Enables high-rate capability
Reaction onset temperature	> 300 °C	Reflects outstanding thermal stability
Principal redox couple	Ti^{4+}/Ti^{3+}	Fully reversible intercalation mechanism

1.12. Safety and Thermal Stability Advantages of LTO

Safety is among the most critical performance parameters in LIB design, especially as applications extend to electric transportation, aerospace systems, and large-scale stationary storage where thermal and electrochemical abuse can cause catastrophic failure. In this context, LTO has emerged as a benchmark anode material due to its exceptional safety margin, outstanding thermal stability, and chemical inertness toward common electrolytes. Unlike conventional graphite, which operates close to the potential of lithium metal (≈ 0.1– 0.2 V vs Li^+/Li) and is therefore susceptible to lithium plating, LTO functions at a significantly higher and safer potential of approximately 1.55 V vs Li^+/Li, effectively eliminating one of the key triggers of thermal runaway. This elevated operating voltage fundamentally changes the anode–electrolyte interface chemistry, enabling stable, dendrite-free operation and significantly reducing parasitic reactions that degrade performance over time (Madani et al., 2025; Murugan et al., 2025).

1.12.1. High Operating Potential and Suppression of Lithium Plating

In graphite-based LIBs, fast charging or low-temperature operation often causes the electrode potential to drop below 0 V vs Li^+/Li, leading to metallic lithium deposition on the surface. This deposited lithium can grow into dendritic structures that pierce the separator, causing internal short circuits, thermal hotspots, and under severe conditions combustion or explosion. In contrast, the 1.55 V plateau of LTO lies well above the lithium plating potential, entirely eliminating this failure mechanism even at high C-rates or subzero temperatures (K. Li et al., 2025).

The intercalation reaction in LTO:

$$\mathbf{Li_4Ti_5O_{12} + 3Li^+ + 3e^- \leftrightarrow Li_7Ti_5O_{12}} \quad \mathbf{(7)}$$

In addition, the higher lithiation potential minimizes electrochemical stress and overpotential-induced heating**,** particularly during rapid charge–discharge cycles. As a result, LTO-based cells can safely tolerate fast-charging conditions that would cause thermal instability in graphite electrodes. This property is one of the primary reasons LTO is chosen for high-power battery systems such as hybrid buses, forklifts, and backup power units, where repeated rapid cycling and high C-rates are common (Tomaszewska et al., 2019).

1.12.2. Thermal Stability and Resistance to Exothermic Reactions

Thermal stability is a defining advantage of LTO. Calorimetric and differential scanning calorimetry (DSC) studies demonstrate that the onset temperature of exothermic reactions between LTO and carbonate-based electrolytes exceeds 300–350 °C, compared with approximately 120–150 °C for graphite electrodes. This high onset temperature is attributed to the chemical inertness of the Ti–O framework and the absence of highly reactive lithiated carbon species (Bhutia, Grugeon, El Mejdoubi, Laruelle, & Marlair, 2024). LTO's insertion potential yields small reversible (entropic) heat during cycling and avoids electrolyte reduction, lowering heat generation compared with lower-voltage anodes. In situ/operando studies show a two-phase transition with zero-strain, which underpins high thermal and mechanical stability. SEI formation and gas evolution are strongly suppressed at this voltage; recent cell-level work even reports complete suppression of gas evolution during cyclic aging after proper formation. These traits are advantageous in large-format cells where thermal management is challenging (Yi, Yang, & Xie, 2015).

LTO's spinel lattice also acts as a heat sink**,** dispersing localized thermal gradients that might otherwise lead to hot spots. The high thermal conductivity of the oxide framework further assists in homogenizing temperature distribution across the electrode, mitigating the risk of thermal runaway in multi-cell modules. Figure 1.7 compares the thermal behavior of fully lithiated graphite and LTO anodes using DSC. In panel (A), the red curve (graphite) exhibits

multiple sharp exothermic peaks beginning around 130–150 °C, corresponding to SEI decomposition and subsequent electrolyte reduction reactions. These reactions release large amounts of heat ($\Delta H \approx 2750$ J g^{-1}), which can trigger thermal runaway in conventional Li-ion cells. In contrast, the blue dashed curve (LTO) shows only minor and broad heat flow features with a much smaller total heat release ($\Delta H \approx 383$ J g^{-1}), confirming its superior thermal stability. Panel (B) presents the accumulated heat versus temperature for both materials. The graphite anode shows a steep increase in total exothermic output, while LTO maintains a nearly flat profile up to ~350 °C, illustrating its intrinsic safety advantage. This stability arises from LTO's higher lithiation potential (~1.55 V vs Li^+/Li), which prevents SEI formation and electrolyte decomposition even under elevated temperature conditions (Z. Chen, Belharouak, Sun, & Amine, 2013).

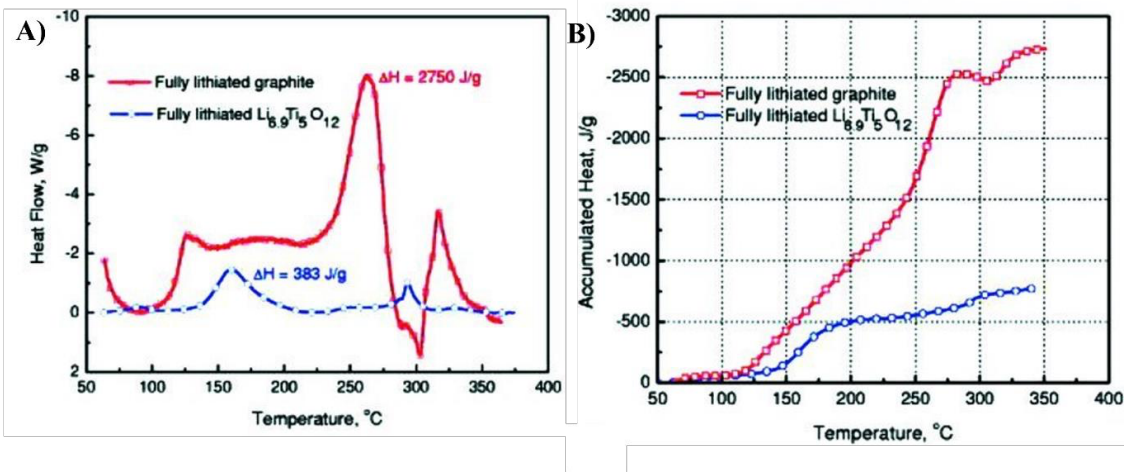

Figure 1.7. DSC profiles of graphite and LTO anodes with standard carbonate electrolyte. Graphite shows sharp exothermic peaks around 130 °C (SEI decomposition) and 200–250 °C (electrolyte reaction), whereas LTO remains stable up to 350 °C, confirming its superior thermal resilience (Z. Chen et al., 2013).

1.12.3. Wide Temperature Operability and Abuse Tolerance

LTO's stability extends across a remarkably wide operating temperature range. Electrochemical studies report that LTO anodes maintain over 90 % of their room-temperature capacity even at −30 °C, where graphite performance typically collapses due to lithium plating and sluggish diffusion kinetics. At elevated temperatures (up to 55–60 °C), LTO cells exhibit

stable cycling with minimal capacity fade, while graphite-based cells suffer accelerated SEI degradation (Abdelrahman et al., 2025).

In addition to temperature resilience, LTO demonstrates excellent tolerance to overcharge and short-circuit conditions**.** In overcharge tests up to 250 %, no significant voltage or temperature spikes were observed, and the cells retained their structural integrity. Similarly, nail-penetration and crush tests revealed no thermal propagation or ignition contrasting sharply with conventional LIBs. These results reinforce LTO's status as a "non-explosive anode"**,** capable of safe operation under conditions that would typically induce catastrophic failure in graphite or silicon systems. Recent advancements in sensor-integrated lithium-ion battery architectures have substantially improved real-time safety monitoring, thermal management, and tolerance to mechanical and electrochemical abuse. Figure 1.8A illustrates the fabrication and integration of MEMS-based multifunctional micro-sensors for in-situ temperature, pressure, and gas-evolution detection within lithium-ion cells. Figure 1.8B shows the packaging sequence of a modified coin cell where a MEMS sensing platform with a Fabry–Perot window is embedded to enable optical and electrical readout during high-temperature cycling.

Figure 1.8C details the microfabrication steps of the flexible three-in-one sensor using thin-film deposition, photolithography, and polyimide substrates, while Figure 1.8D displays the finished device and its micrograph. This schematically depicts the coin-cell assembly, highlighting the integration of the flexible sensor between the anode and separator layers without compromising cell integrity. Figure 1.8E extends this concept to a battery-pack scale, illustrating how distributeds sensing modules and bus-bar separators can monitor local temperature and pressure gradients. Finally, Figure 1.8F presents the dynamic gas-response behavior of a $TiO_2/CuO/Cu_2O$ thin-film sensor at 350 °C toward incremental concentrations of $C_4H_{10}O_2$ vapors, demonstrating fast, stable, and reversible detection. These integrated micro-sensors enable wide-temperature operability by providing localized diagnostics of heat generation and gas evolution during abuse events such as overcharge or thermal runaway. Their inclusion enhances abuse tolerance and early-warning capability, which are critical for high-energy cells operating under extreme or high-temperature environments.

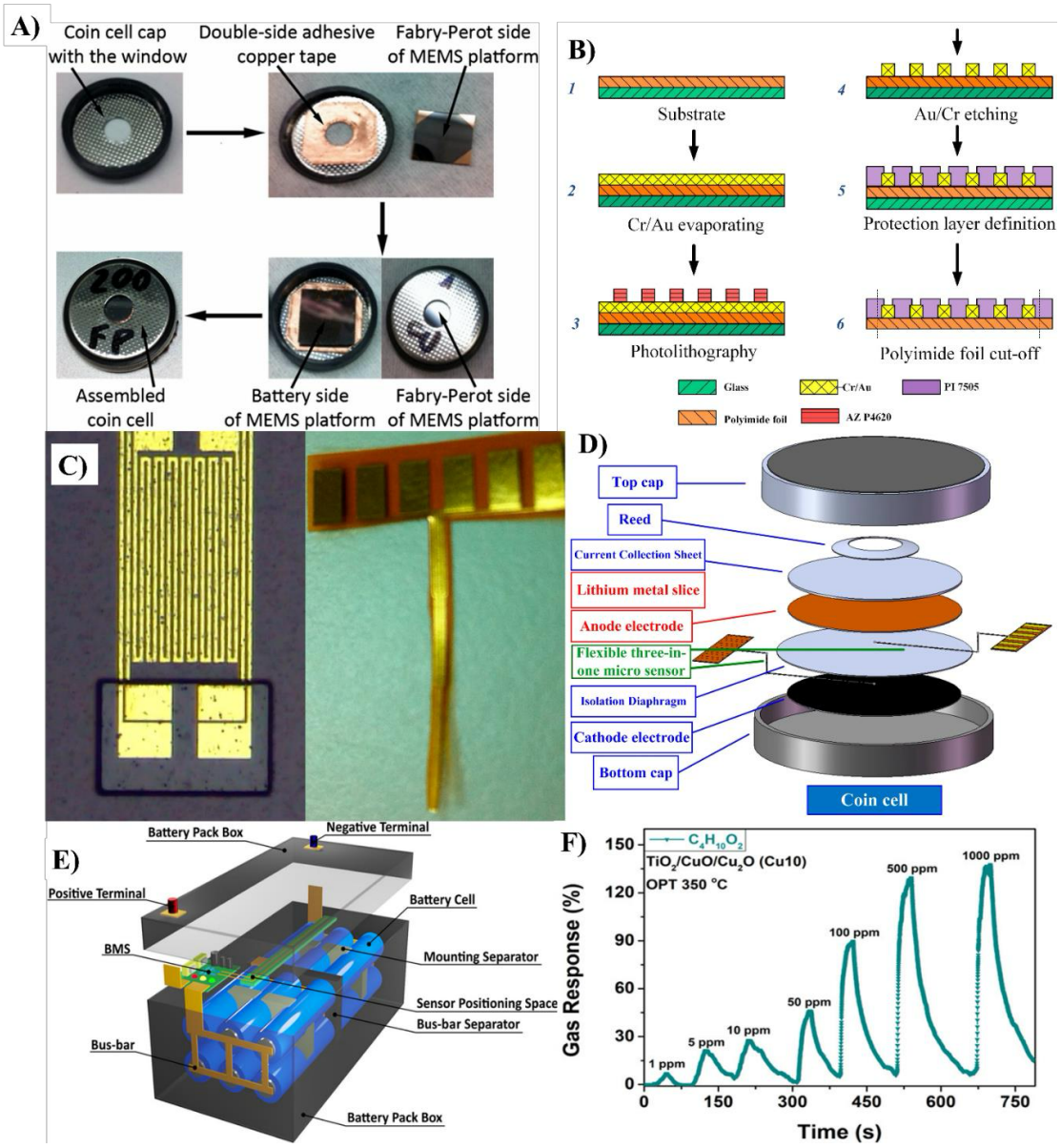

Figure 1.8. Fabrication and integration of MEMS-based microsensor technology for in situ monitoring of lithium-ion batteries. A) Packaging process of the modified coin cell, featuring a machined window and the installation of a MEMS platform using conductive adhesive tape, followed by electrolyte and lithium assembly within an inert environment, (Pomerantseva et al., 2013) B) Stepwise fabrication of a flexible three-in-one microsensor through photolithography and metal deposition, enabling multifunctional sensing on a single substrate. C) Photograph and optical micrograph of the finalized microsensor device. D) Structural schematic showing the integration of the flexible sensor within a Li-ion coin cell architecture, (B-D) reproduced with permission (C.-Y. Lee et al., 2015) E) Conceptual

3D model of a battery pack with integrated monitoring system and battery management module. F) Dynamic gas-sensing performance of TiO_2/CuO/Cu_2O (10 nm) films at 350 °C toward various concentrations of $C_4H_{10}O_2$ vapors, demonstrating selective response characteristics, (E-F) reproduced with permission (Lupan et al., 2023).

1.12.4. Relationship between Thermal Stability and Structural Chemistry

The exceptional safety of LTO can be rationalized by its strong Ti–O covalency and fully oxidized framework. Titanium exists predominantly in the +4 oxidation state, which is chemically stable and nonreactive toward the electrolyte. The absence of metallic lithium or low-valent species means there are no spontaneous reduction reactions that generate heat or gases. Additionally, the cubic close-packed oxygen sublattice and high lattice energy (~ −5000 kJ mol^{-1}) provide thermal robustness, preventing decomposition even at high temperatures (Llaín-Jiménez et al., 2022). Theoretical thermodynamic modeling further confirms that the Gibbs free energy of decomposition (ΔG_decomp) for LTO remains positive up to 700 °C, whereas for lithiated graphite, it becomes negative near 200 °C, indicating spontaneous degradation at relatively low temperatures. This highlights the intrinsic thermal stability advantage of oxide-based anodes over carbonaceous ones. In-situ synchrotron X-ray diffraction studies (Figure 1.9) have directly visualized the structural degradation of lithiated graphite under thermal stress. As temperature increases beyond ~120 °C, LiC_6 progressively transforms through intermediate LiC_{12} and LiC_{18} phases, accompanied by LiF and Li_2O formation from electrolyte decomposition and lithium leaching. Above ~250 °C, the graphite lattice collapses and gas evolution intensifies, marking the onset of exothermic reactions that drive thermal runaway in conventional anodes (X. Liu et al., 2021).

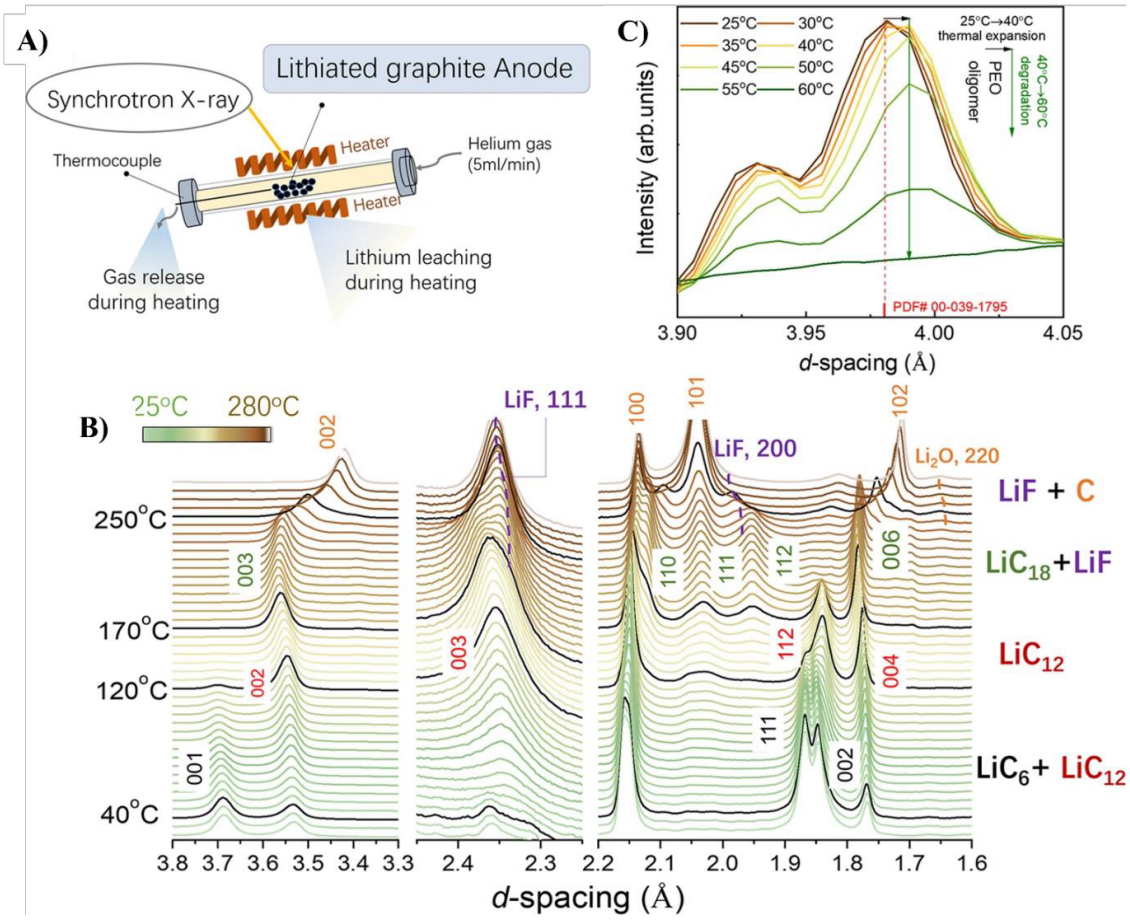

Figure 1.9. In-situ synchrotron X-ray diffraction analysis of lithiated graphite during thermal heating. (a) Schematic of the experimental setup showing gas release and lithium leaching during temperature ramping. (b) Temperature-dependent XRD patterns (25–280 °C) revealing structural decomposition and phase evolution from $LiC_6 \rightarrow LiC_{12} \rightarrow LiC_{18} \rightarrow$ carbon + LiF. (c) Detailed d-spacing evolution of the (002) reflection, highlighting thermal expansion and subsequent degradation of the electrode/electrolyte interface. Reproduced with permission from Liu et al., Nature Communications 12 (2021) 3844 (X. Liu et al., 2021).

The unique safety characteristics of LTO have profound implications for battery system architecture. Because LTO virtually eliminates thermal runaway, pack designers can reduce the need for heavy protective casings and complex cooling systems, improving gravimetric and volumetric energy efficiency at the system level. The material's high rate capability and low heat generation enable fast charging with minimal thermal management requirements, supporting ultra-fast charging infrastructure for electric buses, taxis, and industrial vehicles

(Mahek et al., 2025). Furthermore, LTO's wide electrochemical window and stability against electrolytes make it compatible with solid-state and aqueous lithium-ion chemistries, both of which are being explored for next-generation safe energy storage systems. The non-reactive nature of LTO also simplifies recycling and end-of-life processing, as it does not produce hazardous or flammable residues (Kazemi et al., 2025a).

Despite its outstanding thermal safety, chemical stability, and mechanical robustness LTO faces a fundamental drawback that restricts its widespread adoption in energy-dense battery systems its poor intrinsic electrical conductivity and moderate lithium-ion diffusion rate. These transport-related limitations arise directly from its electronic band structure and ionic migration energetics, both of which are dictated by its spinel crystal geometry and titanium oxidation states. Understanding the origins of these limitations, quantifying their impacts, and exploring strategies to mitigate them are essential steps toward optimizing LTO for high-performance LIBs (Shuai Fu et al., 2022; C. Han et al., 2015; Y. Yu, Zhu, Zhang, & Jiang, 2026).

1.13. Electronic Structure and Bandgap Characteristics

The electrical conductivity of a material depends on the availability of free charge carriers and the ease of their transport through the lattice. In the case of LTO, first-principles DFT calculations reveal that it is an n-type wide bandgap semiconductor with a bandgap energy (E9) ranging between 2.0 and 2.3 eV, depending on the specific crystal orientation and defect concentration. The valence band is dominated by oxygen 2p orbitals, while the conduction band is primarily composed of Ti 3d t_2g states. However, instead of forming delocalized conduction bands, these additional electrons localize around Ti^{3+} centers, leading to small polaron formation. Charge transport then proceeds via a thermally activated small-polaron hopping mechanism, in which electrons hop between adjacent Ti^{3+} and Ti^{4+} sites. This process is characterized by an activation energy (E_a) of approximately 0.3–0.5 eV. The electrical conductivity (σ) can thus be expressed by an Arrhenius-type equation (8):

$$\sigma = \sigma_0 \exp\left(-\frac{E_a}{k_b T}\right) \ldots\ldots\ldots (8)$$

where σ_0 is the pre-exponential factor, k_b is Boltzmann's constant, and T is the absolute temperature. Experimental studies report that the room-temperature electronic conductivity of pristine LTO is on the order of 10^{-13} S·cm^{-1}, which is six to eight orders of magnitude lower than that of graphite (~10^{-5} S·cm^{-1}). Such a low conductivity introduces severe charge-transfer polarization and limits the high-rate capability of LTO-based cells.

Figure 1.10 compiles advanced optical and electronic analyses of GaN/AlN semiconductor systems, demonstrating how their dielectric and excitonic properties evolve with crystal orientation and confinement effects. The imaginary dielectric function varies significantly along different crystallographic directions, revealing pronounced optical anisotropy linked to interband transitions. The calculated dielectric spectra further highlight polarization-dependent electronic behavior intrinsic to nitride heterostructures. As the barrier thickness in GaN/AlN quantum wells decreases, the optical transition energies exhibit a blue shift while exciton binding energies increase, confirming strong quantum confinement. Experimental absorption data at 300 K show distinct weak and high-band absorption regions, consistent with theoretical predictions. The comparison between experimental spectra and Bethe–Salpeter equation–based simulations, incorporating quasiparticle and excitonic screening corrections, validates the computational framework and emphasizes its accuracy in reproducing the optical response of wide-bandgap materials (Bayerl & Kioupakis, 2019; Kioupakis et al., 2021; Schleife et al., 2018; Varley & Schleife, 2015; Zacharias & Giustino, 2016)

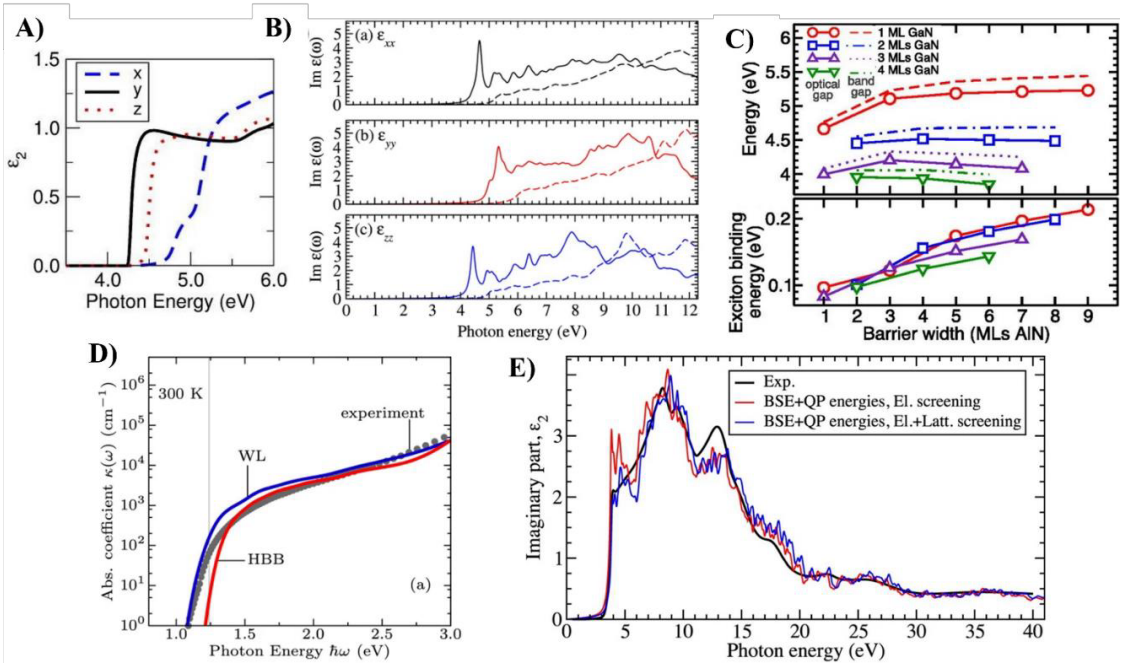

Figure 1.10. Optical and dielectric characteristics of wide-bandgap GaN/AlN semiconductor systems. (A) Direction-dependent imaginary dielectric function (ε_2) showing optical anisotropy, reproduced with permission (Kioupakis et al., 2021) (B) Calculated dielectric spectra along the principal crystallographic axes, illustrating interband transition features, reproduced with permission (Varley & Schleife, 2015) (C) Variation of transition and exciton binding energies with GaN barrier thickness in multiple quantum wells, evidencing strong quantum confinement reproduced with permission (Bayerl & Kioupakis, 2019) (D) Experimental absorption coefficient of GaN at 300 K with defined weak and high-band absorption region, reproduced with permission (Zacharias & Giustino, 2016) (E) Comparison of experimental and Bethe–Salpeter equation (BSE) + quasiparticle (QP) simulated spectra, confirming theoretical–experimental agreement, reproduced with permission (Schleife et al., 2018).

1.13.1. Ionic Conductivity and Lithium-Ion Diffusion Kinetics

Beyond electronic limitations, lithium-ion transport within the LTO lattice also exhibits moderate diffusion kinetics. Lithium migration occurs between the 8a (tetrahedral) and 16c (octahedral) sites through shared faces of TiO_6 octahedra and LiO_4 tetrahedra (Christian M. Julien & Alain Mauger, 2024). The activation barrier for Li^+ diffusion (E_d) is typically reported to be between 0.35–0.52 eV, as derived from both electrochemical impedance

spectroscopy (EIS) and DFT modeling (Chekushkin, Merenkov, Smirnov, Kislenko, & Nikitina, 2021). The lithium diffusion coefficient D_{Li^+} is consequently in the range of:

$$\mathbf{D_{Li^+} = 10^{-8} \rightarrow 10^{-8}\ cm^2 s^{-1}} \quad \text{..... (9)}$$

While this diffusivity is sufficient for moderate charge–discharge rates, it becomes limiting during ultra-fast charging (>10C) or low-temperature operation, where ionic mobility decreases exponentially with temperature according to the Nernst–Einstein relation:

$$\mathbf{\sigma_{ion} = n_{Li^+} q^2 D_{Li^+} / (k_b T)} \quad \text{..... (10)}$$

where $n_{\mathrm{Li}^+}$is the concentration of mobile lithium ions and q is the elementary charge.

At subzero temperatures, D_{Li^+} may decrease by more than two orders of magnitude, resulting in diffusion-controlled polarization and incomplete lithiation of the electrode. Thus, both electronic and ionic conductivities act as bottlenecks that collectively constrain the power performance of LTO (Jung, Dutta, Martha, Jun, & Pol, 2025).

1.13.2. Interfacial Charge-Transfer Limitations

The slow charge-transfer kinetics of LTO at the electrode–electrolyte interface further compound its intrinsic conductivity issues. The charge-transfer resistance (R_{ct}) observed in EIS studies of LTO is typically higher than 150 Ω·cm² for unmodified electrodes, compared to less than 10 Ω·cm² for conductive carbons. This high resistance is attributed to the combination of poor electronic percolation within the bulk electrode and limited active surface sites for charge exchange (Lou & Chen, 2015; Stolz, Winter, & Kasnatscheew, 2024). The impedance behavior can be represented by an equivalent circuit model consisting of a Warburg element (W) for diffusion, a double-layer capacitor (C_{dl}), and a R_{ct} connected in series with the ohmic resistance (R_s):

$$\mathbf{Z(\omega) = R_s + \frac{R_{ct}}{1 + j\omega R_{ct} C_{dl}} + \sigma_W (j\omega)^{-1/2}} \quad \text{..... (11)}$$

This model illustrates how R_{ct} and diffusion-related impedance dominate the low-frequency region of the Nyquist plot for pristine LTO. Enhancing conductivity therefore requires reducing R_{ct} through either surface modification or the creation of conductive networks.

1.14. Temperature Dependence of Conductivity

The temperature dependence of LTO's conductivity reveals the underlying thermally activated transport mechanism. Experimental Arrhenius plots of $In(\sigma T)$ versus $^{1}/_{T}$ show linear behavior, confirming semiconducting behavior consistent with small-polaron hopping. The activation energy is typically 0.45–0.55 eV for electronic transport, and 0.35–0.40 eV for ionic diffusion. Elevated temperatures enhance both ionic and electronic conductivities, but excessive heating may accelerate side reactions or degrade binders in composite electrodes. As a result, thermal management in high-power LTO cells involves maintaining operating temperatures between 25–55 °C, which balances enhanced transport kinetics with long-term electrode stability. This wide operational window is another reason LTO performs reliably in harsh conditions where conventional anodes degrade rapidly (Zhou, Xu, Chen, & Tian, 2025).

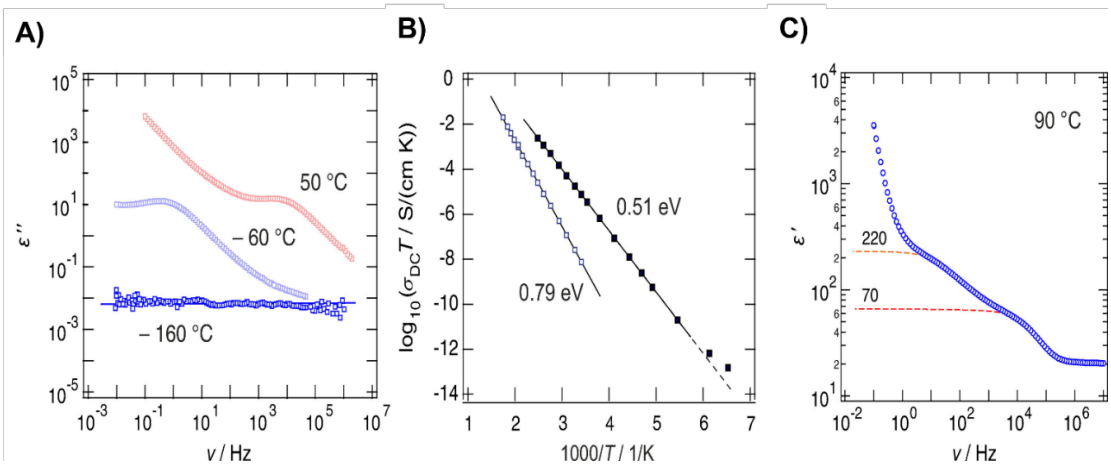

Figure 1.11. A) Permittivity isotherms demonstrating near-constant loss (NCL) behavior at low temperatures, where the imaginary permittivity component (ε″) remains nearly frequency independent. B) Arrhenius representation of DC conductivity (σDC.T vs 1/T) derived from the frequency-independent plateau regions of the conductivity spectra, with corresponding activation energies

indicated. C) Frequency dependence of the real permittivity (ε′), showing two distinct responses with ε′ values of approximately 70 and 220, reflecting separate polarization mechanisms, reproduced with permission (Gadermaier, Hogrefe, Heitjans, & Wilkening, 2021).

1.15. Strategies to Overcome Conductivity Limitations

Over the past decade, extensive research has focused on improving both electronic and ionic conductivity of LTO through four main strategies: **(i)** nanostructuring, **(ii)** doping and defect engineering, **(iii)** carbon or conductive coating, and **(iv)** composite hybridization with advanced materials.

1.15.1. Nanostructuring

Reducing LTO particle size to the nanoscale dramatically shortens Li^+ diffusion paths and increases surface area for charge transfer. Nanostructured morphologies such as nanotubes, nanorods, hollow spheres, and mesoporous frameworks enable faster kinetics and improved power density. For instance, Kang et al. (2020) demonstrated that nanosized LTO (50–100 nm) synthesized via sol-gel route exhibited a threefold increase in rate capability compared with bulk LTO due to enhanced surface diffusion and shortened diffusion lengths. However, excessive nanosizing may increase surface reactivity and reduce tap density, compromising volumetric energy density (Kang, Krajewski, & Lin, 2021). In another study by Wang et al., a micro/nanostructured $Li_4Ti_5O_{12}$ anode material was fabricated through a controlled sol–gel route, during which the precursor gel was processed to yield primary particles in the 50–100 nm range and assembled into hierarchical aggregates. Calcination under optimized conditions ensured phase-pure spinel formation and increased crystallinity, while particle size reduction significantly shortened Li^+ diffusion lengths and increased electrode/electrolyte interface area. As a result, the nanostructured LTO exhibited a multi-fold enhancement in high-rate capability compared to conventionally synthesized bulk particles, attributed to faster surface kinetics and improved Li-ion transport across the nano-domains (Yuanyu Wang & Zhu, 2020). Mao et al. (2015) reported a *one-step continuous aerosolization* method for synthesizing spherical LTO/graphene composites. In this process, an aerosolized graphene oxide suspension containing Li^+ and Ti^{4+} precursors was passed through a high-temperature furnace, promoting simultaneous LTO crystallization and GO crumpling into conductive 3D graphene

spheres. The resulting nanocomposite demonstrated superior electronic conductivity and cycling stability, see Figure 1.12A (Mao et al., 2015).

1.15.2. Doping and Defect Engineering

Aliovalent doping has proven to be one of the most effective routes to improving LTO's conductivity. Substituting Ti^{4+} with cations of different valence states introduces either oxygen vacancies or extra electrons, enhancing carrier concentration. Representative doping reactions (11) include:

$$\mathbf{Nb_{Ti}^{5+} \rightarrow Ti_{Ti}^{4+} + e^{-} \text{ and } Mg_{Ti}^{2+} + V_{O}^{\cdot\cdot} \rightarrow 2Ti_{Ti}^{4+} \ldots\ldots\ldots (12)}$$

These mechanisms either create Ti^{3+} sites or generate oxygen vacancies that improve both electronic and ionic conduction pathways. Nb, Mg, Cr, and Fe doped LTOs have demonstrated conductivity enhancements of up to 10^6 times relative to pristine LTO, with improved rate capability and cycle stability. For instance, Nb^{5+} doping reduced the activation energy for electron hopping by ~0.1 eV, increasing σ to ~10^{-6} S·cm^{-1} without affecting the zero-strain structure. Jiang et al. (2023) developed a *dual-modification route* combining Fe-doping and carbon coating using industrial H_2TiO_3 as a Ti precursor. The process involved mixing, grinding, and spraying of LCO, Fe^{2+}, and glucose, followed by annealing under a carbon-reducing atmosphere to form a uniform carbon-coated Fe-doped LTO composite as shown in the Figure 1.12B. The method simultaneously enhanced conductivity and structural integrity (Jiang et al., 2023).

1.15.3. Carbon Coating and Conductive Additives

Carbon coatings are widely employed to create a conductive network around LTO particles. Amorphous carbon, graphene, or carbon nanotube (CNT) coatings enhance electronic conductivity and reduce interfacial impedance. Thin carbon shells deposited via pyrolysis or chemical vapor deposition (CVD) provide continuous electron pathways, while maintaining ionic accessibility. Apostolopoulou et al. demonstrated that a graphene-wrapped LTO composite achieved 95 % capacity retention at 10C**,** compared to only 62 % for uncoated

LTO. The carbon layer also acts as a protective barrier against electrolyte corrosion and surface phase transformation (M. Apostolopoulou, D. Vernardou, & S. Passerini, 2024). Ma et al. (2013) synthesized F-doped $Li_4Ti_5O_{12}$ (C-FLTO) using a *two-step hybrid hydrothermal–solid-state route*. TiF_4, citric acid, and glucose precursors underwent hydrothermal synthesis to form anatase-TiO_2 intermediates, followed by high-temperature solid-state lithiation with LiF and $LiOAc \cdot 2H_2O$, as shown in Figure 1.12C The carbon encapsulation preserved the ball-in-ball morphology, providing excellent rate capability and reduced charge-transfer resistance (Y. Ma, Ding, Ji, & Lee, 2013).

1.15.4. MXene and 2D Hybrid Composites

Recent advancements in MXene–LTO composites have significantly bridged the intrinsic conductivity gap of LTO anodes. MXenes, particularly $Ti_3C_2T_x$, exhibit metallic-level electrical conductivity (>10^3 $S \cdot cm^{-1}$), large aspect ratios, and hydrophilic, chemically active surfaces, rendering them highly effective conductive scaffolds for electrochemical energy storage. In MXene–LTO heterostructures, the two-dimensional MXene layers function as continuous electron highways and lithium-ion diffusion corridors, thereby markedly reducing charge-transfer resistance (R_ct) and enhancing interfacial reaction kinetics. As a result, $Ti_3C_2T_x$–LTO composites have been reported to sustain high specific capacities (~165 mAh g^{-1}) even at ultrahigh rates (20 C), while maintaining excellent cycling stability over thousands of cycles.

More recently, Feng et al. (2025) demonstrated a multifunctional MXene–LTO electrode architecture in which $Ti_3C_2T_x$ MXene replaces conventional insulating polymer binders and simultaneously serves as a conductive matrix and electrochemically active component. Owing to its metallic conductivity, rich surface chemistry, and strong adhesion to the current collector, the MXene binder forms a continuously percolated conductive network that suppresses pore blockage and facilitates rapid ion/electron transport throughout the electrode. Consequently, the MXene-integrated LTO anode delivers a high reversible capacity of 197.7 mAh g^{-1} at 0.5 C, outstanding rate capability of 127.1 mAh g^{-1} at 20 C, and exceptional long-term stability with 93.4% capacity retention over 10,000 cycles. When paired with a $LiFePO_4$ cathode, the resulting full cell achieves an energy density of 150.7 Wh kg^{-1}, highlighting the critical role of MXene-enabled conductive and structural synergy in advancing LTO-based

anodes toward high-energy, high-power, and long-life lithium-ion batteries.

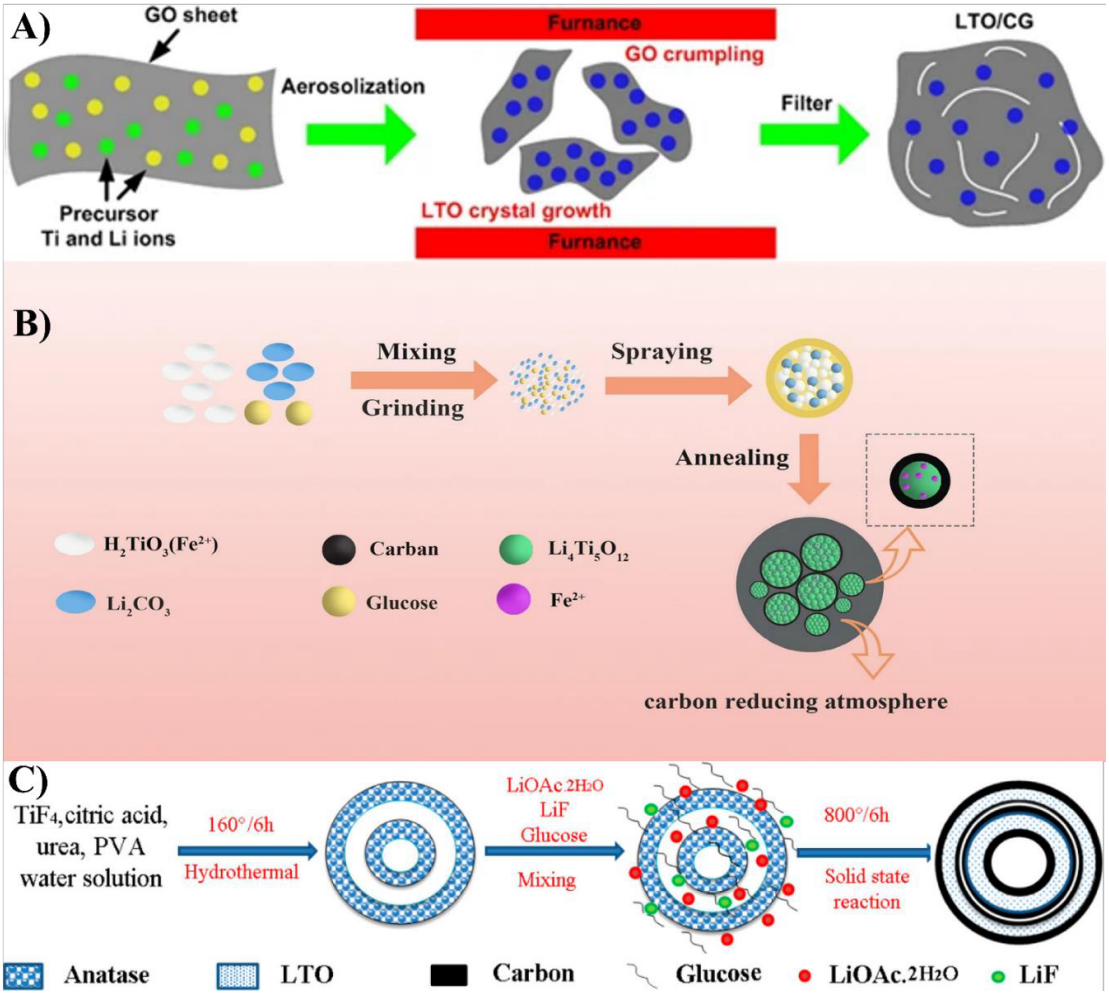

Figure 1.12. Schematic illustration of various synthesis routes for conductive LTO composites: (A) One-step aerosolized growth of LTO/graphene spheres through GO-assisted crystallization (Mao et al., 2015). B) Carbon-reduction synthesis of Fe-doped, carbon-coated LTO using industrial H_2TiO_3 and glucose precursors (Jiang et al., 2023); Hydrothermal-assisted solid-state synthesis of F-doped, carbon-encapsulated LTO composites (Y. Ma et al., 2013).

The combined effect of these modifications can be quantitatively evaluated by comparing charge-transfer resistance and diffusion coefficients before and after enhancement. Representative improvements are summarized below in table 1.2

Table 1.2. Summary of transport properties and electrochemical performance improvements of pristine and modified $Li_4Ti_5O_{12}$ anodes reported in the literature.

Modification Strategy	σ ($S \cdot cm^{-1}$)	D_Li$^+$ ($cm^2 \cdot s^{-1}$)	R_ct ($\Omega \cdot cm^2$)	Performance Gain	Ref.
Pristine LTO	1×10^{-13}	1×10^{-9}	>150	Baseline	(Yi et al., 2012)
Nanostructured LTO	1×10^{-11}	5×10^{-9}	80	Moderate	(Yuanyu Wang & Zhu, 2020)
Nb-doped LTO	1×10^{-6}	1×10^{-8}	40	High-rate capability	(Chandrasekhar, Dhananjaya, Hussain, Mauger, & Julien, 2021)
C-coated LTO	1×10^{-5}	2×10^{-8}	25	High conductivity	(Maria Apostolopoulou, Dimitra Vernardou, & Stefano Passerini, 2024; M. Apostolopoulou et al., 2024)
MXene–LTO hybrid	1×10^{-3}	5×10^{-8}	<10	Near-metallic performance	(F. Han et al., 2023)

Such data demonstrate that through a combination of defect engineering and composite design, LTO can achieve several orders of magnitude improvement in electrical conductivity, transforming it from an insulating oxide to a quasi-conductive high-power anode suitable for modern lithium-ion applications.

1.16. Applications of LTO-Based Composites in Energy Storage Systems

The growing demand for high-performance, safe, and long-lasting energy storage technologies has elevated LTO from a laboratory curiosity to a commercially relevant anode material. The structural stability, intrinsic safety, and long cycle life of LTO, combined with ongoing advancements in composite engineering and conductivity enhancement, have opened diverse application avenues from EVs and public transportation fleets to large-scale grid storage and hybrid electrochemical capacitors. In these sectors, performance metrics such as cycle life, power density, temperature resilience, and safety are often prioritized over absolute energy density. Consequently, LTO-based systems represent a vital balance between energy

and safety in next-generation electrochemical energy storage (Kazemi et al., 2025b; J. Liu et al., 2020).

1.16.1. LTO-Based Composites in Electric Vehicles (EVs)

1.16.1.1 Requirements for EV Anode Materials

EV propulsion demands anode materials that can sustain high power output, fast charging, and long cycle stability, without compromising safety. Graphite anodes, while offering high capacity, suffer from lithium plating and thermal instability during rapid charging, leading to reduced lifetime and potential safety hazards. The zero-strain structure and elevated operating potential (1.55 V vs Li^+/Li) of LTO eliminate such risks, enabling rapid charge–discharge cycles and operation under extreme conditions (Celadon, Sun, Sun, & Zhang, 2024).

However, pristine LTO's relatively low energy density (175 $mAh \cdot g^{-1}$) has limited its use in long-range EVs. Recent developments in LTO composites particularly with carbonaceous materials (graphene, CNTs) and MXene-based frameworks have drastically improved both power density and rate capability, making LTO viable for short- and medium-range EV platforms such as electric buses, hybrid taxis, and delivery fleets.

1.16.1.2. Performance of LTO Composites in EV Systems

Advanced LTO–carbon composites exhibit superior electrochemical performance under high C-rate cycling. Apostolopoulou et al. (2024) demonstrated that graphene-coated LTO (LTO@rGO) electrodes achieved >95% capacity retention at 10C rate and more than 5000 stable cycles, due to enhanced electron percolation and improved electrolyte–electrode interaction. Similarly, CNT-integrated LTO networks have achieved reversible capacities exceeding 165 $mAh \cdot g^{-1}$ at 20C, outperforming conventional LTO cells by more than threefold in power output (Maria Apostolopoulou et al., 2024).

In large EV packs, thermal stability is equally critical. LTO's high exothermic onset (>300 °C) and resistance to lithium plating provide substantial safety margins. As a result, many commercial EV battery modules such as the Altairnano (Altairnano., 2025) and Microvast (Microvast Holdings, 2024) systems employ LTO-based anodes for urban mobility fleets. These modules can be charged to 80% capacity in less than 10 minutes, maintaining over 20,000 cycles with minimal degradation.

1.16.1.3. Challenges and Outlook for EV Adoption

While LTO's high power and safety are unmatched, its energy density remains modest (90–110 $Wh \cdot kg^{-1}$ at cell level), limiting range compared to graphite–silicon anodes (>200 $Wh \cdot kg^{-1}$). Future EV applications will likely focus on hybrid electrode architectures, such as LTO/Si–C composites, which combine LTO's safety with the high capacity of silicon (Sturman et al., 2021; Wei et al., 2021). Moreover, with advances in solid-state electrolytes and fast-charging infrastructure, LTO's intrinsic advantages particularly in reliability and lifecycle economics are expected to outweigh its energy deficit in heavy-duty and fast-charging EV sectors

1.16.2. LTO Composites for Grid-Scale and Stationary Energy Storage

1.16.2.1. Importance of Stability and Cycle Life

Grid-scale energy storage systems (ESS) require materials that can provide high power density, long service life, and excellent operational stability. Safety and cost-per-cycle are more critical than gravimetric energy density. LTO's ability to maintain structural and electrochemical integrity over tens of thousands of cycles, combined with its high round-trip efficiency (~90–95%), makes it an ideal anode for such applications. The zero-strain lattice ensures mechanical integrity over decades of operation, while the stable SEI layer minimizes electrolyte decomposition and capacity fading. LTO's wide operating temperature window (−30 °C to 60 °C) is particularly beneficial for renewable integration, where batteries must perform under fluctuating environmental conditions and variable charge–discharge rates (BIELEWSKI, 2022; Hesse, Schimpe, Kucevic, & Jossen, 2017).

1.16.2.2. Performance of Advanced LTO Composites in Grid Applications

In stationary storage applications, LTO–MXene and LTO–graphene composites have demonstrated extraordinary durability. Liu et al. (2023) demonstrated that an in-situ grown LTO–$Ti_3C_2T_x$ MXene composite maintained over 90 % capacity after 10,000 cycles at 10C, with minimal impedance rise, owing to synergistic ionic and electronic transport through the 2D MXene framework, which also acted as an effective thermal buffer under high-current operation (F. Han et al., 2023). Furthermore, Nb-doped LTO exhibits improved conductivity and reduced charge-transfer resistance, contributing to higher energy throughput per cycle. When integrated into large-scale grid modules, doped-LTO cells deliver over 20,000 cycles at >85% capacity retention, outperforming most commercial lithium-ion technologies (Chandrasekhar et al., 2021).

LTO's inherent safety also enables simplified thermal management, reducing system cost by up to 30%. Its compatibility with aqueous and solid electrolytes further broadens its potential for stationary energy storage in harsh environments, such as desert-based solar farms or offshore wind-buffering installations.

The long cycle life of LTO reduces levelized cost of storage (LCOS) by minimizing replacement frequency. LTO is also more environmentally benign than nickel- or cobalt-based electrodes due to its non-toxic titanium composition and ease of recycling. End-of-life LTO electrodes can be directly reused after washing or mild thermal regeneration, as the structural degradation is minimal compared to layered oxides or graphite. These sustainability factors align with global clean-energy objectives and circular-economy policies.

1.16.3. Role of CNFs in Enhancing Conductivity of LTO-Based Anodes

In the pursuit of next-generation lithium-ion battery anodes, the spinel structured LTO has increasingly been recognized as a material of exceptional promise. Its virtues include a stable insertion potential of ~1.55 V vs Li^+/Li, which effectively eliminates lithium plating, and a virtually zero-strain lattice change during cycling that provides outstanding durability and safety (Christian M. Julien & Alain Mauger, 2024). Yet despite these merits, the widespread application of LTO has been hindered by one glaring limitation: its intrinsically low electronic conductivity (on the order of 10^{-13} $S \cdot cm^{-1}$) and sluggish lithium-ion kinetics. It is precisely this conductivity bottleneck that has spurred a rich body of research aimed at integrating conductive carbonaceous networks into LTO composite anodes a strategy that has revealed the central role of CNFs and other additives.

In essence, the incorporation of CNFs into LTO anodes represents a structural and functional leap: rather than treating LTO particles as isolated islands of active material, the fibrous carbon network creates a continuous conductive scaffold that envelops and interconnects these particles, thereby dramatically shortening electron path lengths, reducing inter-particle resistance, and promoting efficient charge transfer. This structural role of CNFs is directly evidenced by the SEM micrographs (Figure 1.13), which reveal the progressive morphological evolution from pristine LTO to LTO–CNF composites, as well as the

formation of a more integrated and continuous conductive network within the CNF-containing electrode architectures. CNFs possess a high aspect-ratio one-dimensional geometry, good intrinsic conductivity, and mechanical robustness, making them particularly well suited to serve as “highways” for electrons in a densely packed electrode matrix. For example, an early and influential study by Zhang et al. reported “urchin-like” LTO–CNF composite particles formed via a sol–gel route where multiple CNFs penetrate a secondary LTO particle structure while carbon black (CB) particles fill the voids (B. Zhang et al., 2012). Electrodes made from this composite delivered ~123 mAh g^{-1} at 15 C, compared with ~91 mAh g^{-1} for neat LTO, underscoring how networked carbon significantly improves both conductivity and Li-ion diffusion coefficient.

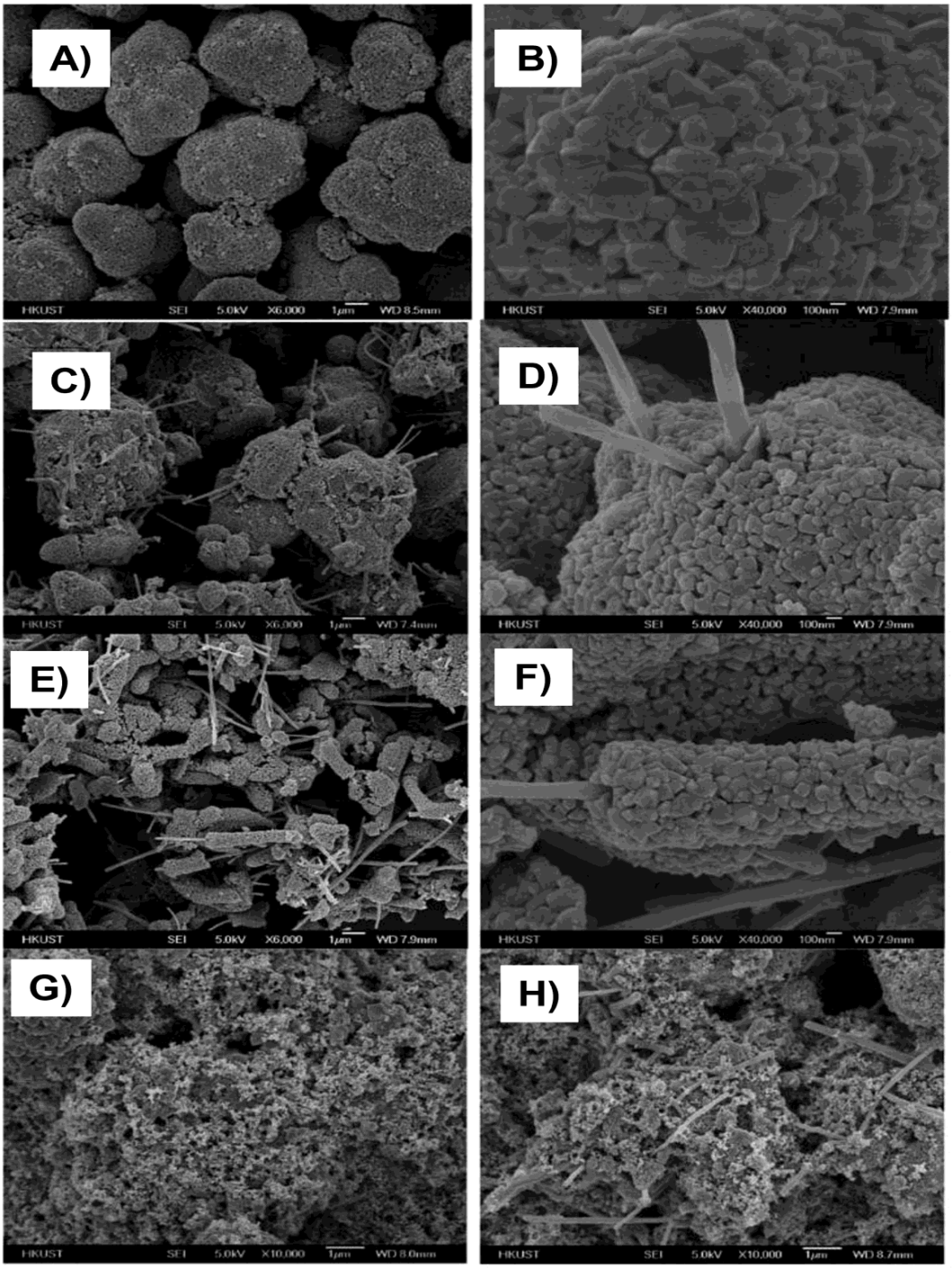

Figure 1.13. SEM micrographs showing the morphological evolution of (a–b) pristine LTO, (c–d) LTO–CNF-1, and (e–f) LTO–CNF-2 composites. Images (g) and (h) depict electrode architectures of LTO–CB–PVDF and LTO–CNF-1–CB–PVDF, respectively, illustrating the enhanced structural

integration and conductive network provided by the carbon nanofiber framework. Reproduced with permission (B. Zhang et al., 2012).

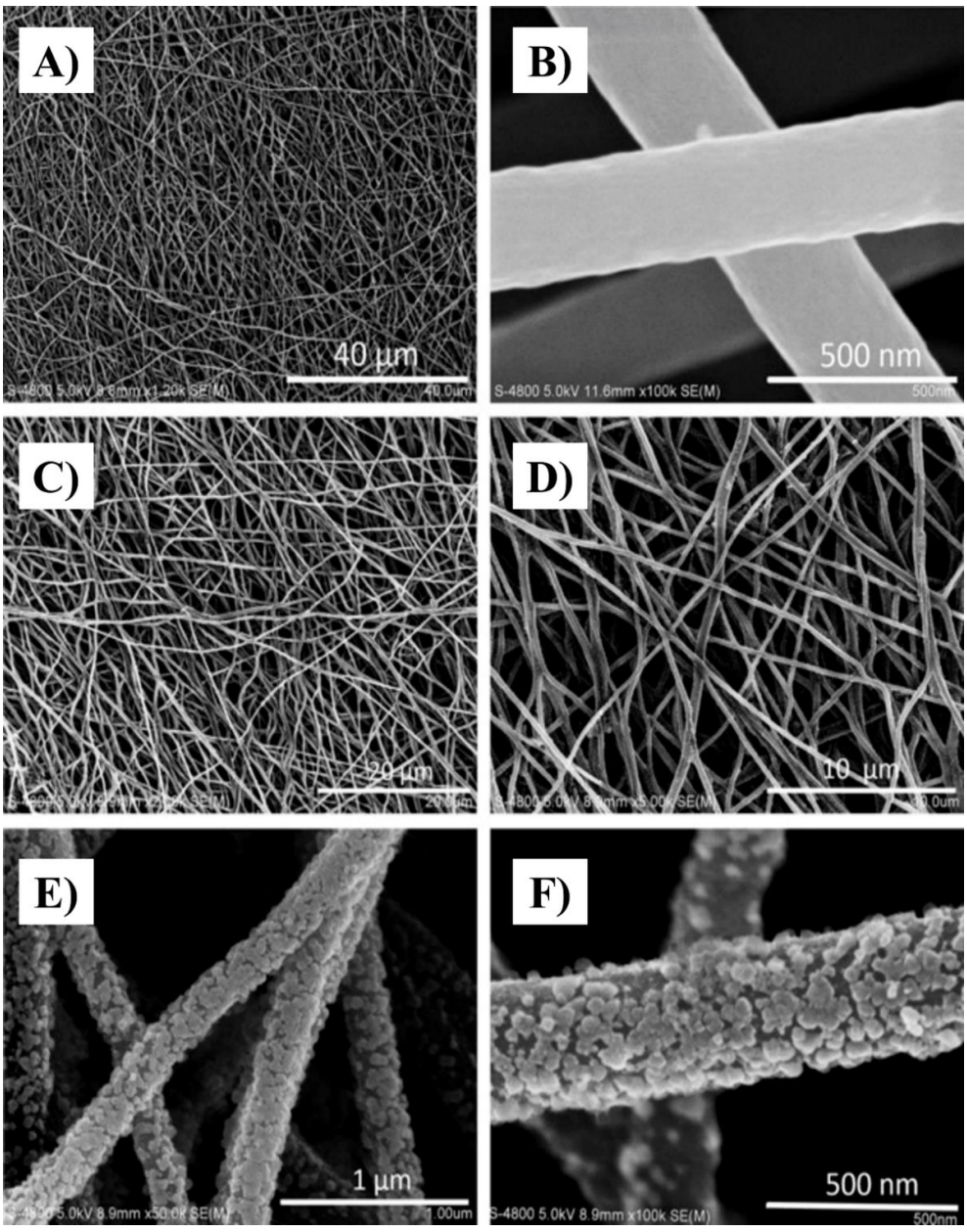

Figure 1.14. FE-SEM micrographs illustrating the morphological evolution of CNFs and LTO/CNF composites. (A, B) Uniform, bead-free CNFs with smooth and continuous fiber surfaces; (C, D) LTO/CNF hybrid structure showing homogeneous nanoparticle deposition along the fibrous network;

(E, F) magnified views revealing well-anchored LTO nanoparticles on CNF surfaces, confirming strong interfacial bonding and effective structural integration (Z. Zhang et al., 2017).

As shown in the SEM images in Figure 1.14, the structural evolution and surface morphology of electrospun CNFs and their LTO–CNF composites are clearly observed. Figure 1.14A, B The pristine CNFs display a uniform, bead-free morphology with continuous and well-interconnected fibrous networks, indicating smooth surfaces and excellent fiber alignment prior to compositing. Figure 1.14C, D At intermediate magnifications, the LTO–CNF hybrid network reveals a dense, mat-like architecture, where LTO nanoparticles are homogeneously distributed along the CNF framework, forming a three-dimensional conductive network that facilitates electron transport and mechanical reinforcement. Figure 1.14E, F The high-magnification images highlight LTO nanoparticles firmly anchored on CNF surfaces, forming a granular coating that confirms successful crystallization on the carbon backbone. This strong interfacial adhesion between LTO and CNFs enables efficient Li^+ and e^- transport pathways, resulting in enhanced electrochemical performance and long-term structural stability of the composite electrode (Z. Zhang et al., 2017).

As shown in Figure 1.15, the incorporation of CNFs into the LTO matrix leads to a pronounced enhancement in electrochemical performance across multiple metrics. The galvanostatic charge–discharge profiles (Figure 1.15A) reveal that the LTO–CNF composite maintains higher discharge capacities and reduced polarization over a wide range of C-rates compared with pristine LTO nanocrystals, indicating improved reaction kinetics and electronic conductivity. Consistently, the rate-dependent cycling results (Figure 1.15B) demonstrate superior capacity retention of the LTO–CNF electrode under progressively increasing current densities, highlighting the stabilizing role of the interconnected CNF network during high-rate operation.

Furthermore, when benchmarked against other carbon-modified LTO systems (Figure 1.15C), the LTO–CNF composite in this work exhibits competitive and, in several cases, superior high-rate discharge performance, underscoring the effectiveness of the fibrous carbon architecture in facilitating rapid electron transport and Li^+ diffusion. The long-term cycling

data at 20 C (Figure 1.15D) further confirm the structural robustness of the LTO–CNF electrode, which delivers stable capacity retention over extended cycling with Coulombic efficiency approaching 100%. Collectively, these results demonstrate that the CNF framework acts as a continuous conductive scaffold that bridges the intrinsically insulating spinel particles, suppresses particle aggregation, and preserves electrode integrity, thereby enabling enhanced rate capability and long-term cycling stability (Z. Zhang et al., 2017).

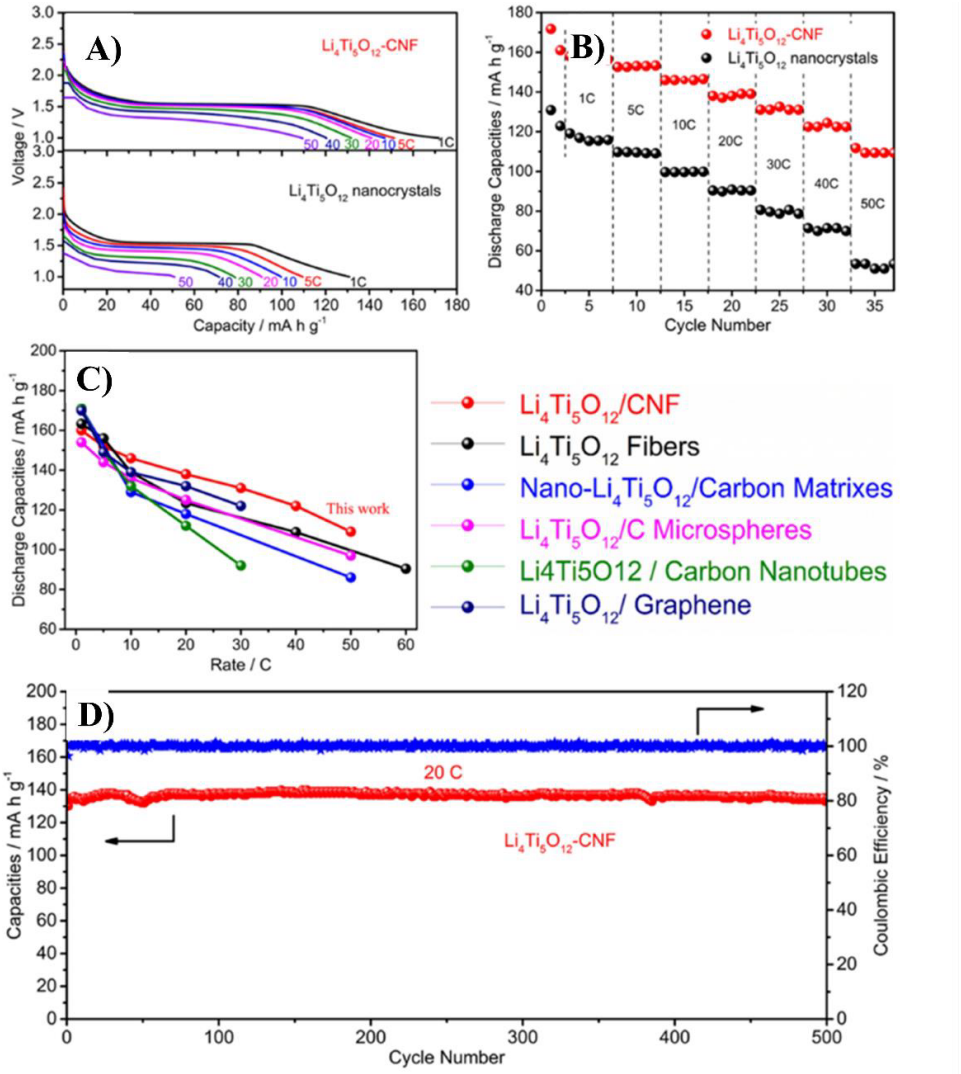

Figure 1.15. Electrochemical performance of LTO–CNF composite electrodes. (A) Galvanostatic charge–discharge curves of LTO–CNF and pristine LTO nanocrystals at various C-rates, showing superior rate capability of the composite. (B) Cycling stability comparison at multiple current rates, highlighting the enhanced reversible capacity and stability of LTO–CNF. (C) Rate performance

benchmarked against other carbon-modified LTO systems, confirming improved high-rate discharge behavior in this work. (D) Long-term cycling test at 20 C, demonstrating stable capacity retention and near-100 % CE over extended operation (Z. Zhang et al., 2017).

This morphological configuration is more than aesthetic; the fibrous carbon network enhances intimate contact between the active material and conductive matrix, reduces local current concentration, improves lithium-ion accessibility, and shortens both electronic and ionic transport paths. Furthermore, CNFs contribute mechanical robustness their fibrous skeleton cushions volumetric fluctuations and prevents conductive network degradation during prolonged cycling, a critical requirement for high-rate applications (Z. Zhang et al., 2017). However, while CNFs form a strong backbone, a high-performing electrode requires a fully percolating conductive framework that bridges every active particle and fills interstitial voids. At excessive fiber loadings, CNFs may agglomerate and restrict ion transport by reducing porosity; at insufficient loadings, they may fail to connect distant particle domains. To overcome these structural trade-offs, researchers have incorporated CNTs and CB to engineer hierarchical carbon architectures with multi-scale conductivity.

CNTs, possessing high intrinsic conductivity and extreme aspect ratios, construct long-range conductive networks even at minimal loadings. Studies on LTO/carbon composites demonstrate conductivity trends following LTO < LTO/N-CNF < LTO/CNF < LTO/CNT < LTO/N-CNT, confirming the superior bridging capability of CNTs (J.-S. Lee et al., 2022). The extended nanotube framework spans agglomerated oxide clusters, reduces charge-transfer resistance, and accelerates electron mobility through continuous percolation paths (L. Sun et al., 2016). Nevertheless, CNT networks alone may leave microvoids unfilled, resulting in local electronic “dead zones.” Here, CB plays a complementary role. Its nanosized particles penetrate voids and interfaces between larger CNTs/CNFs and active particles, enhancing interfacial contact and homogenizing current distribution. In an “urchin-like” LTO–CNF/CB hybrid system, the inclusion of merely 5 wt % CNFs and 5 wt % CB yielded a uniform 3D conductive framework and drastically improved high-rate capability (Saha, Das, & Rahman, 2026).

Thus, the most effective LTO composite architecture is a hierarchical conductive mesh, where CNFs supply structural reinforcement, CNTs provide long-range electron highways, and CB fills interstitial gaps to ensure uniform current flow and robust Li^+/e^- transport (X. Zhang, Lu, Zhou, & Li, 2020). This is where CB fine particulate carbon plays a complementary role. Although CB has lower conductivity per gram compared with CNTs or CNFs, its small particle size allows it to infiltrate the micro-voids and interfaces between larger carbon fibers/tubes and active particles, effectively improving contact area, filling gaps in the network, and smoothing out local current densities. In the earlier referenced "urchin-like" LTO–CNF work, CB at just 5 wt% alongside 5 wt% CNFs enabled a three-dimensional conductive network across the whole composite, significantly boosting high-rate capability (B. Zhang et al., 2012).

Thus, the most effective architecture emerges as a hierarchical conductive mesh: CNFs provide the backbone and mechanical reinforcement; CNTs act as long-distance bridges and network enhancers; CB fills fine interstitial gaps and improves interface contact (see schematic – Figure 1.16).

The multi-panel Figure 1.16 illustrates hierarchical CNT fiber composite architecture and its structural detail across scales. In panel (a) a schematic shows CNT bundles embedded in a matrix, highlighting the scale of single CNTs ($\sim 10^{-7} m$) up through macroscale composite ($\sim 10^{-2} m$). Panel (b) reveals intra- and inter-bundle void structures and how densification can alter morphology. Panel (c) presents high-resolution electron microscopy and fiber bundle cross-sections, showing CNT alignment, internal structure and voids, and a representative representative volume element (RVE) diagram for effective transport modeling. Together, this illustration (Figure 1.16) emphasizes how the one-dimensional conductive CNT pathways, bundled into macro-scale fibers and integrated in a composite with active material, can provide a continuous electron and ion conduction network with minimized transport distances and enhanced connectivity.

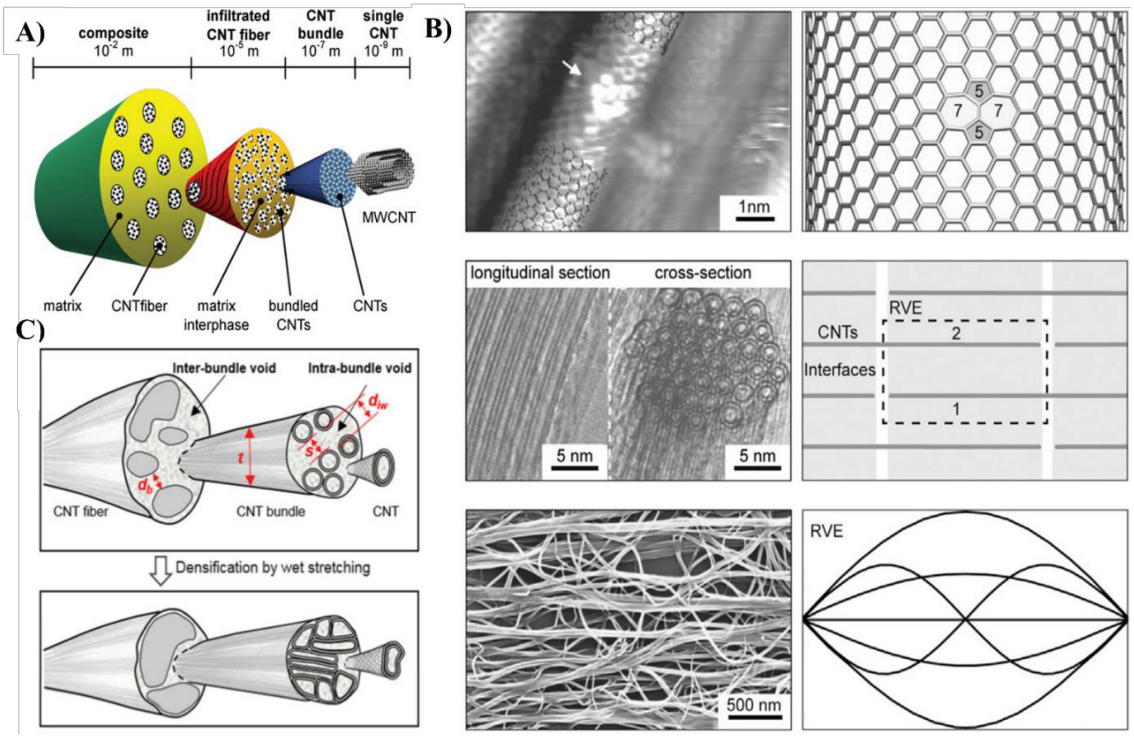

Figure 1.16. Multi-scale depiction of a carbon-nanotube fiber composite scaffold for enhanced electrode conductivity: (A) schematic of scale ranging from single CNTs to macroscale composite; (B) intra-bundle and inter-bundle void structure and densification schematic; (C) electron microscopy and RVE diagram illustrating CNT bundle cross-section, alignment and void morphology. The architecture supports continuous electron/ion transport and improved electrode kinetics, reproduced after permission (X. Zhang et al., 2020).

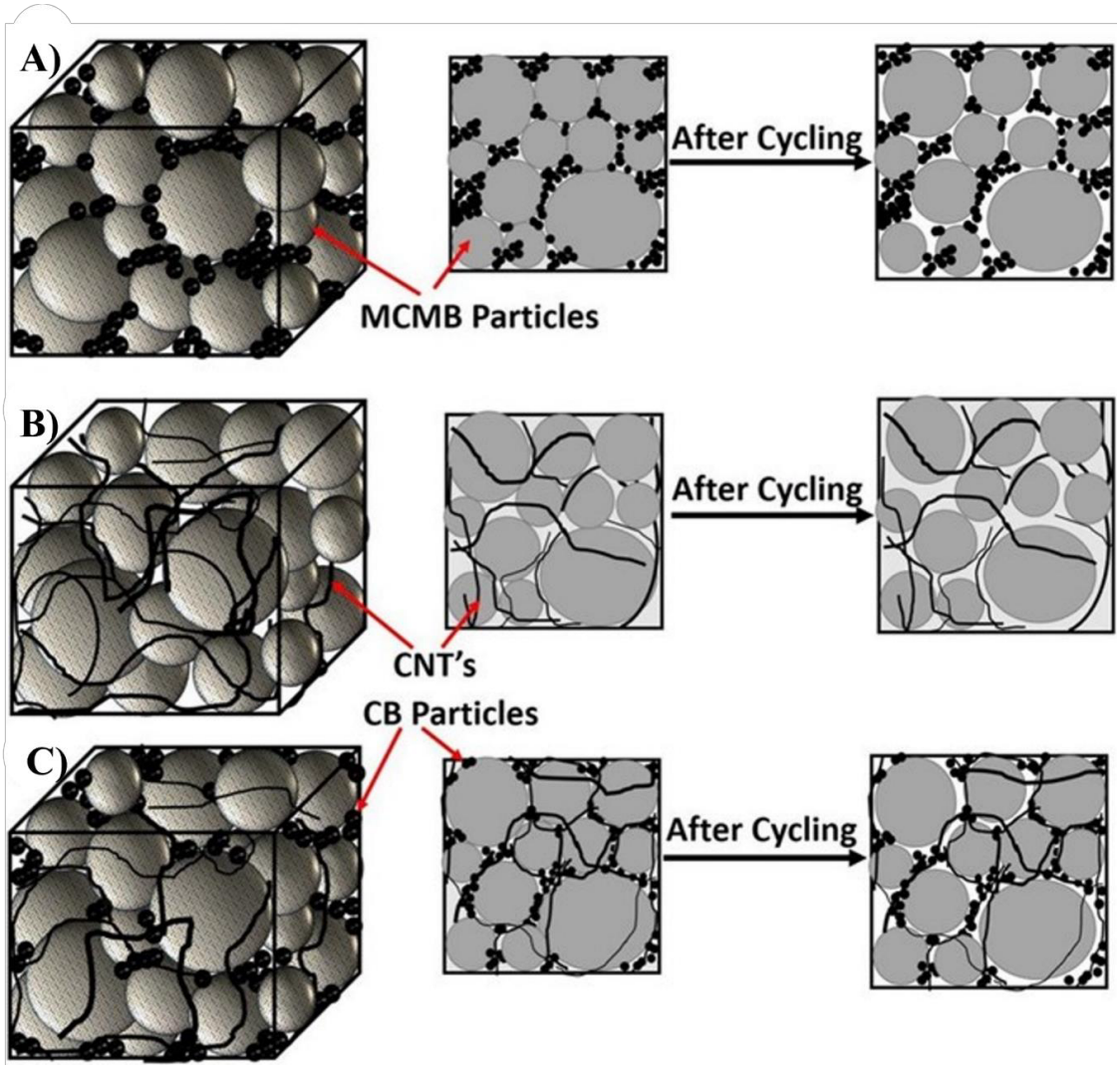

Figure 1.17. Schematic illustration of the microstructural evolution of MCMB-based composite anodes before and after electrochemical cycling: (A) pristine MCMB with CB only; (B) MCMB composite with CNTs and CB dual network; and (C) optimized hybrid architecture combining CNTs and CB for enhanced inter-particle connectivity (Ahamad, Ahmad, Mehta, & Gupta, 2017)

The schematic in Figure 1.17 visualizes how conductive network morphology affects electrode stability and capacity retention during long-term cycling. Here In the Figure 1.17A, pure CB additives form localized, discontinuous contacts that degrade under cycling, leading to poor electronic percolation. In Figure 1.17B, CNTs introduce extended conductive bridges between MCMB particles, improving network resilience and maintaining conductivity after repeated charge–discharge cycles. In Figure 1.17C, the CNT + CB hybrid configuration

creates a hierarchically interconnected structure where CNTs serve as macroscopic conductive pathways and CB fills micro-voids, preventing disconnection between active particles.

Consequently, the performance enhancements in LTO anodes incorporating these carbon additives are substantial. EIS shows marked reductions in the semicircle diameter (charge-transfer resistance) and steeper Warburg slopes (improved lithium diffusion). For instance, LTO/CNT composites report R_ct values an order of magnitude lower than neat LTO, translating into higher fraction of theoretical capacity retained at high rate something rarely achievable with pristine LTO (C. M. Julien & A. Mauger, 2024).

Fundamentally, the mechanisms by which CNFs and their hybrid carbon counterparts enhance conductivity are:

1. **Electron percolation improvement** – The fibrous carbon network forms continuous low-resistance pathways connecting the active material to the current collector, reducing electron-hopping distances and eliminating isolated oxide grains.
2. **Contact interface enhancement** – Carbon additives improve electrical contact at the interface between the active particle surface and the conductive matrix, reducing interfacial resistance and supporting efficient charge transfer.
3. **Volume change buffering and mechanical stability** – The fibrous and networked carbon frame accommodates any minor structural changes of LTO during cycling, preserving network integrity and avoiding contact loss.
4. **Ion transport synergy** – Although the primary aim is improved electronic conduction, the improved conductivity allows high current operation, which in turn reduces lithium-ion diffusion limitations. Moreover, well-distributed carbon networks help maintain porosity and electrolyte access, indirectly supporting ionic transport.
5. **Hierarchical gap-filling** – The combined CNF/CNT/CB architecture helps fill multiple scales of gaps from macro-scale clusters (bridged by CNTs) to micro-scale voids (filled by CB) ensuring uniform conductivity throughout the electrode.

The practical implications are profound: by integrating CNFs and other carbon additives into LTO-based anodes, one can reposition LTO from a safe yet low-power material into a viable

candidate for high-rate, high-power applications such as electric vehicles or grid storage. Indeed, hybrids that combine conductive carbon scaffolds with optimized particle size, porosity and active-material loading have achieved charge/discharge at very high C-rates (10–20 C+) with sustained cycling over hundreds of cycles (B. Zhang et al., 2012).

In terms of composite design guidelines emerging from literature:

- The loading of carbon additives must be optimized: too low a loading will fail to form percolation; too high a loading dilutes the active material and reduces energy density.
- The dispersion and network connectivity of the carbon fillers are critical: uniform distribution helps avoid agglomeration, ensures each particle is wired, and minimizes dead zones.
- The interface between LTO and the carbon additive must be engineered for low resistance: coating methods, conductive carbon growth or functionalization can assist.
- The structure of LTO (size, morphology, porosity) must complement the carbon network: smaller particles reduce ion-path length, hierarchical porosity supports electrolyte access, and networked carbon works best when oxide grains are intimately integrated.
- The hierarchical architecture is more effective than any single additive: combining CNFs (backbone), CNTs (bridges) and CB (gap-fillers) yields better outcomes than each alone.

In conclusion, the significance of carbon nanofibers in enhancing the conductivity of LTO-based anodes lies in their ability to transform a material hindered by poor conductivity into an electrode with remarkable kinetics and rate capability. When combined with CNTs and carbon black in a designed hierarchical conductive network, the synergy of electronic pathways, contact interface optimization and mechanical stability enables LTO to deliver performance approaching that of more conductive materials, while retaining its inherent safety and long cycle life. As the field moves toward electrification and grid-scale storage, these composite strategies will be central to unlocking the full potential of LTO anodes.

1.17. State of the art 3D printed Batteries

3D printing is revolutionizing battery electrodes by enabling more complex designs, improving performance, and increasing scalability compared to traditional methods. By precisely controlling the electrode's 3D structure, including shape, thickness, and internal channels, 3D printing can enhance ion and electron transport, leading to higher energy/power density, improved cycle life, and greater mechanical stability. This technology also allows for rapid prototyping, customization for specific applications, and the potential for more efficient manufacturing processes (Fonseca et al., 2023; Y. Liu et al., 2025; A. A. Pavlovskii, K. Pushnitsa, A. Kosenko, P. Novikov, & A. A. Popovich, 2024). 3D printing is rapidly becoming a transformative tool, enabling electrode architecture far beyond the conventional planar slurry-cast films. The impetus for this shift stems from the increasing demands for higher power density, faster charge/discharge rates, and bespoke form factors (e.g., flexible, micro-batteries, integrated systems) that cannot be fully met by legacy manufacturing routes (Mottaghi & Pearce, 2024) Traditional methods are characterized by coating processes, calendaring, and layer stacking, which limit control over internal geometry, porosity gradients, and three-dimensional transport pathways. In contrast, 3D printing allows layer-by-layer deposition of electrode and potentially cell components (active materials, conductive networks, current collectors, electrolyte reservoirs) with complex internal geometries, tunable porosity, and spatially optimized architectures, thereby reducing ion and electron diffusion distances and improving overall electrode utilization (Gao et al., 2022).

Within the context of this thesis, which focuses on high-performance anodes based on LTO enhanced by conductive carbon networks and new fabrication strategies, the inclusion of 3D-printing techniques is of critical importance. Although LTO boasts excellent structural stability, safety (zero-strain insertion), and long cycle life, its poor intrinsic conductivity and modest kinetics remain major barriers. Application of 3D-printed electrode architectures affords a route to re-engineer the electrode as a functional network: one where active-material particles, conductive additives (e.g., carbon nanofibres, nanotubes, carbon black), and current-collector pathways are co-designed and spatially integrated. The result is an electrode in which the conductive network is built into the architecture, porosity is tuned for electrolyte

penetration and ion access, and mass-loading gradients can be optimized for high rate performance. Indeed, reviews of 3D-printed Li-ion electrodes identify advantages such as "shorter diffusion pathways, larger surface area, and more effective electrolyte infiltration" when compared to conventional electrodes.

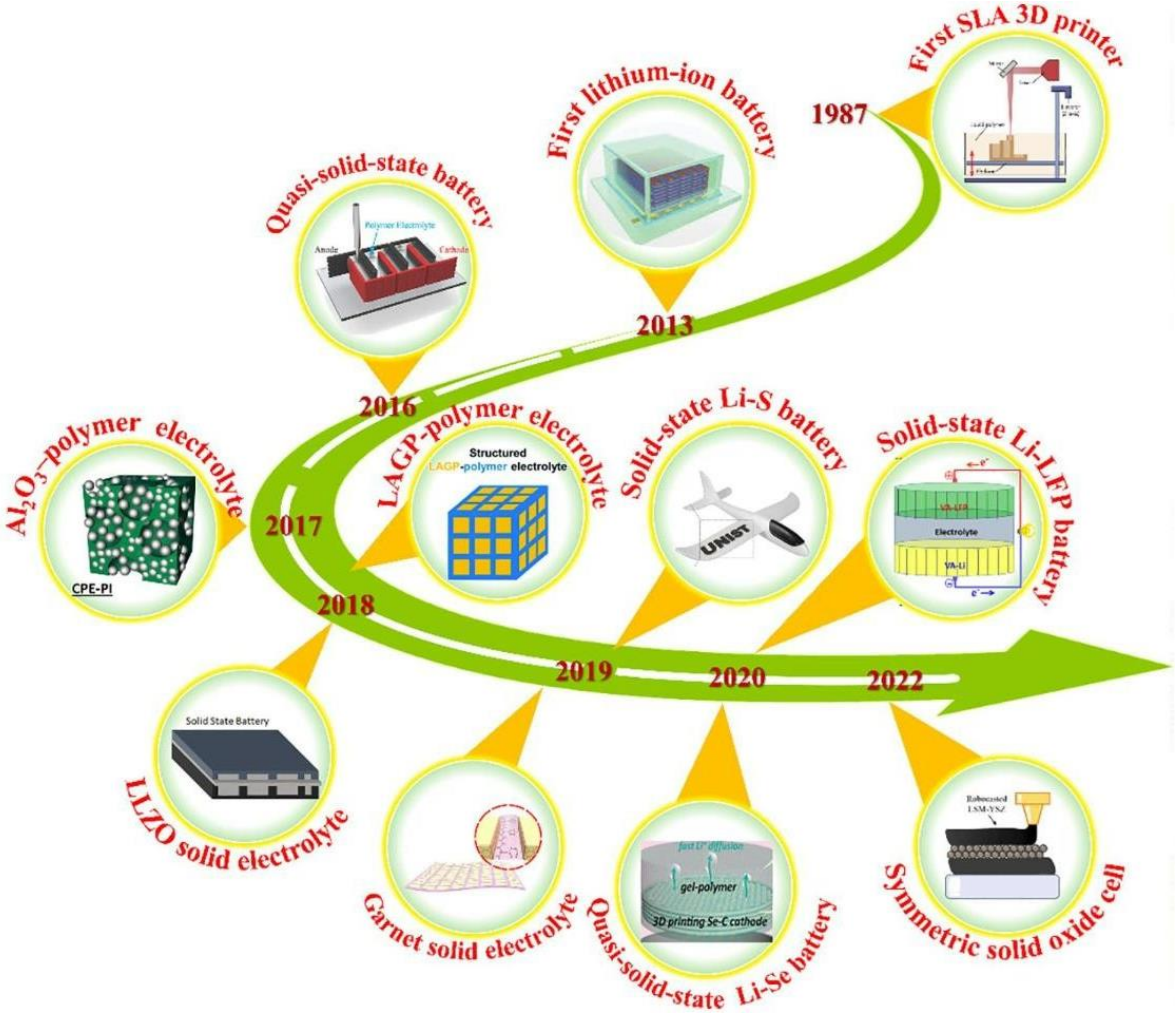

Figure 1.18. Timeline illustrating the evolution of 3D printing technologies and their progressive integration into battery research and development (Gao et al., 2022).

As shown in Figure 1.18, the timeline maps the technological trajectory linking 3D printing to the advancement of battery materials and architectures. Since the introduction of stereolithography (SLA) by Charles Hull in 1987, additive manufacturing has transitioned from a prototyping tool into a fabrication method for functional energy devices. Successive

breakthroughs in printing techniques such as fused deposition modeling (FDM), selective laser sintering (SLS), direct ink writing (DIW), and inkjet printing (IJP) have enabled precise control of electrode geometry, porosity, and interfacial contact. These innovations have accelerated the development of quasi-solid and solid-state batteries, allowing the integration of structured electrolytes like LLZO and LAGP and the realization of complex, high-performance architectures such as 3D-printed Li–S and Li–Se cells. The convergence of 3D printing and electrochemistry now offers unprecedented scalability and design flexibility for next-generation energy storage systems (Gao et al., 2022).

However, like all emerging additive manufacturing paradigms, each 3D-printing technique for Li-ion electrode fabrication exhibits distinct advantages and constraints governed by its material compatibility, achievable resolution, deposition throughput, active-material loading capacity, binder chemistry, and required post-processing steps (e.g., drying, sintering, or curing). The following table systematically compares the principal printing methodologies employed in Li-ion electrode production, outlining their operational parameters, performance trade-offs, and representative studies from recent literature. This helps contextualize the trade-offs: for instance, ME approaches (such as DIW) allow higher active-material loading and thicker electrodes (important for high areal capacity), whereas MJ and VAT-P offer finer resolution architectures (beneficial for micro-battery or high-power designs) but often at the cost of lower loading or more complex resin/ink systems. By selecting and tailoring the printing method, an electrode designer can optimize for either high power (short diffusion/transport paths) or high energy (thick loading) regimes. From the manufacturing and scalability perspective, important advantages of 3D printing include reduced waste (since material is only deposited where needed), shorter process chains (printing layer by layer replaces multiple steps of coating/calendering/drying), and flexibility for custom or application-specific shapes (which may reduce cell stacking or packaging overhead). In fact, Mottaghi et al. argue that 3D printing offers design freedom, material flexibility, reduced pack weight and the potential for on-demand customised battery fabrication (Mottaghi & Pearce, 2024).

Nevertheless, the challenges must be acknowledged. Achieving high areal loading (i.e., large mass of active material per unit area) while preserving the designed architecture and maintaining good electron/ion transport remains difficult. Many printed electrodes still suffer from lower cycling stability or inferior performance relative to best slurry-cast electrodes. Inks and filaments must simultaneously provide printability, mechanical integrity, electronic/ionic connectivity and compatibility with electrolyte and cell assembly. Post-print curing or sintering may be required, adding complexity. The interface between printed layers may introduce additional resistances or delamination. Through-put and cost per cell remain higher than conventional methods for large-scale production (Song et al., 2025).

In the context of this thesis, and specifically for LTO-based composite anodes, the implication is clear: the conductive network enhancements (via CNFs, CNTs, CB) must now be considered alongside architectural innovations enabled by 3D printing. That is, rather than simply improving the material's conductive and ionic transport properties, one must also optimise how that material is spatially arranged, how the conductive scaffold is integrated at the printing stage, how porosity, filament geometry, layer thickness and current-collector interface are co-designed, that are explained in this thesis in the later chapters. This synergy offers a pathway to unlock high-power LTO anodes (which combine structural safety and stability of LTO with rate performance typically reserved for more conductive materials). The forthcoming chapters of this thesis will therefore address: **(a)** composite formulation (active material + conductive additives), **(b)** filament/pellets development for printability, **(c)** 3D-print architecture design (geometry, porosity, conductive pathways), and **(d)** performance evaluation (rate capability, cycling, stability, scalability).

1.18. Motivation and Objectives

The rapid growth of energy storage applications in portable electronics, electric vehicles, and grid-scale systems has intensified the demand for LiB that simultaneously offer high power capability, long cycle life, and enhanced safety. Within this context, lithium titanate has emerged as a promising anode material due to its zero-strain characteristic, excellent thermal stability, and intrinsic resistance to lithium dendrite formation. However, the widespread deployment of LTO-based electrodes remains constrained by its inherently low electronic

conductivity, limited lithium-ion diffusion kinetics, and modest theoretical capacity, which collectively restrict achievable energy density, particularly at high mass loadings.

Recent advances in material engineering and additive manufacturing suggest that these limitations can be mitigated through architected electrode designs, conductive network integration, and post-processing strategies that enhance transport properties without sacrificing structural integrity. In particular, the combination of three-dimensional (3D) printing approaches with conductive carbon frameworks and solvent-assisted post-treatments offers new opportunities to decouple electrode thickness from ionic and electronic transport limitations. Despite these advances, a systematic understanding of how electrode architecture, conductive reinforcement, and post-processing influence the electrochemical performance of thick LTO-based electrodes remain incomplete.

The primary motivation of this thesis is therefore to develop and investigate additively manufactured LTO-based electrodes with engineered porosity and integrated conductive networks that enable high areal capacity, improved rate capability, and long-term cycling stability. The work aims to bridge the gap between conventional slurry-cast electrodes and next-generation 3D-structured electrodes by leveraging filament-based fabrication, carbon nanofiber reinforcement, and solvent-based post-treatment strategies.

Based on this motivation, the specific objectives of the thesis are as follows:

1. To design and fabricate 3D-printed LTO-based electrodes with controlled geometry, thickness, and internal architecture using additive manufacturing techniques tailored for electrochemical applications.
2. To engineer continuous conductive networks within printed electrodes in order to enhance electronic percolation and mitigate charge-transfer limitations inherent to LTO.
3. To systematically investigate the influence of 3D electrode architecture on lithium-ion transport, electrochemical kinetics, and polarization behavior in thick electrodes.

4. To establish quantitative structure–performance relationships by correlating architectural parameters with electrochemical metrics such as areal capacity, rate capability, impedance response, and cycling stability.
5. To benchmark the performance of 3D-printed LTO electrodes against conventional slurry-cast counterparts and state-of-the-art 3D-structured battery electrodes reported in the literature.

Through these objectives, this thesis aims to contribute fundamental insights into the design principles of architecture, additively manufactured battery electrodes and to demonstrate viable pathways toward high-performance, scalable 3D printed LiB for next-generation energy storage applications.

Chapter 2

State of the Art 3D Printed Batteries

Chapter 2. State of the Art 3D printed batteries

2.1 Introduction

Additive manufacturing (AM), commonly referred to as three-dimensional (3D) printing, has recently evolved into a pivotal technique for fabricating lithium-ion battery electrodes and complete cell architectures. It enables unprecedented control over electrode geometry, microstructure, and spatial material distribution, facilitating tailored electrochemical performance and improved structure–property relationships.

2.2. 3D Printing techniques

Among the principal AM methods applied in battery research are direct ink writing (DIW), inkjet and aerosol jet printing (IJP/AJP), fused filament fabrication (FFF or FDM), and stereolithography (SLA). Each technique offers unique advantages in terms of printable material systems, spatial resolution, deposition precision, and scalability, while also posing distinct challenges related to ink rheology, interlayer adhesion, and post-processing demands (Maurel et al., 2023; Y. Zhao, Liu, Liu, & Jiang, 2009).

2.2.1. Direct Ink Writing

DIW is a material-extrusion technique in which a visco-elastic ink or paste composed of active materials, conductive additives, binder and solvent is forced through a nozzle and deposited layer by layer according to a computer-aided design (CAD) file. Its shear-thinning rheology facilitates extrusion and shape retention post-deposition. DIW is particularly attractive for battery electrodes because it allows the printing of thick, high-loading structures, incorporates multi-material deposition and offers good control over internal porosity and architecture. For example, Yan et al. reported DIW printed micro-battery designs with high areal energy and power densities(J. Yan et al., 2022). However, DIW faces challenges in ink formulation (ensuring printability while maintaining high active-material loading), controlling drying/shrinkage, ensuring inter-layer adhesion, and achieving sufficient mechanical integrity, especially when scaling to high areal / volume electrodes (Alexander A. Pavlovskii, Konstantin Pushnitsa, Alexandra Kosenko, Pavel Novikov, & Anatoliy A. Popovich, 2024).

2.2.2. Inkjet Printing

Inkjet Printing (IJP) (and its variant, aerosol jet printing, AJP) falls under the category of material-jetting techniques. In this method, droplets of low-viscosity ink containing active or conductive materials are jetted onto a substrate, allowing high resolution and patterning precision. Pavlovskii et al. classify IJP as a key technique for printed Li-ion battery electrodes, along with DIW, FFF and SLA. The advantages of IJP include fine feature size (often from a few micrometres), minimal material waste and compatibility with thin-film or micro battery architectures. On the downside, IJP is typically limited to low viscosity inks which restricts the loading of active materials, hence limiting areal capacity; furthermore, printing thick electrodes or ensuring structural integrity can be problematic; and the throughput may be lower compared with extrusion methods (Bashir et al., 2018; Rubio & Bolduc, 2025)

2.2.3. Fused Filament Fabrication

Fused Filament Fabrication (FFF, or FDM – Fused Deposition Modeling) is a well-known 3D-printing method in which a thermoplastic filament (or composite filament loaded with active/conductive particles) is melted and extruded through a nozzle and deposited layer by layer. In the battery-electrode context, FFF is appealing because the filament can be pre-loaded with electrode active material and additive, simplifying the print process. The strengths of FFF include simplicity, relatively high throughput, and compatibility with multi-material printing (active material, current-collector, housing). However, limitations arise in achieving high active-material loading in the filament while retaining printability (melt viscosity, nozzle clogging), limited resolution (often ~50-200 μm or higher), potential for anisotropic mechanical and electrical properties due to layer interfaces, and the need for post-processing (e.g., drying, binder removal, sintering) to achieve electrochemically viable electrodes (Czerwiński, Słojewska, Jurczak, Dębowski, & Zygadło-Monikowska, 2024)

2.2.4. Stereolithography

Stereolithography (SLA), a vat-photopolymerisation technique, cures a photocurable resin by layerwise exposure to UV light, building 3D structures with very high resolution (often down

to 10–50 µm or less). In battery fabrication, SLA enables the creation of intricate electrode or cell architectures (e.g., interdigitated micro-electrodes, micro-batteries) that cannot be realized via other methods. The review by Ma et al. places SLA among the four representative printing techniques for micro-batteries, noting that its advantage lies in high resolution and complex geometry (J. Ma et al., 2024). However, SLA is constrained by its reliance on photocurable resins (which often have limited compatibility with high-loading active materials or require complex post-treatments), issues of cure shrinkage, layer adhesion, and often limited throughput, especially for thicker electrodes or high-volume manufacturing.

Table 2.1. Common 3D-Printing Techniques for Battery Applications [Working Mechanisms, Key Materials, Strengths & Limitations].

Technique	Process Description & Key Parameters	Strengths	Limitations	Ref.
DIW (Direct Ink Writing)	Extrusion of viscoelastic paste containing active material, binder, and conductive additive (~100–500 µm resolution).	High solids loading, adaptable architectures, multi-material printing.	Ink rheology controls critical; drying and interlayer adhesion challenges.	(Alexander A. Pavlovskii et al., 2024)
IJP / AJP (Material Jetting)	Ink droplets (10–50 µm) precisely deposited onto substrate;	High resolution, minimal material waste, precise patterning.	Low throughput, limited active-material content, demanding ink formulation.	(Bashir et al., 2018; Sztymela et al., 2022)

	suitable for low-viscosity inks.			
FFF / FDM (Fused Filament Fabrication)	Layer-by-layer extrusion of thermoplastic filament loaded with active materials.	Simple, scalable, cost-effective; good mechanical stability.	Limited electrical conductivity; thermal constraints (<200 °C); low precision.	(Czerwiński et al., 2024; Shaju, Ummer, Thomas, & Kandasubramanian, 2025)
SLA (Stereolithography)	UV/laser curing of photocurable resin with dispersed electroactive particles (~10–100 μm resolution).	Excellent resolution, complex internal geometries, micro-battery capability.	Restricted to photocurable resins, shrinkage, limited loading, slow build rate.	(J. Ma et al., 2024; Maurel et al., 2023)
This work (FFF-based 3D printing of LTO–CNF electrodes)	**Filament-based extrusion of LTO–CNF composite filament; layer-by-layer deposition enabling thick, architected electrodes**	**High mass loading and areal capacity; scalable and low-cost; mechanically robust self-supporting electrodes; compatible with embedded**	**Limited resolution compared to DIW/IJP; conductivity constrained by filament formulation; trade-off between CNF loading, printability, and electrical performance.**	**This thesis**

	with controlled porosity; compatible with one-shot device fabrication.	**batteries and monolithic devices.**		

In the context of my thesis on LTO-based anodes and conductive composite networks, this overview of printing technologies is critical because the choice of printing method will directly influence (i) how well the conductive network (e.g., carbon nanofibers, nanotubes) can be integrated within the printed structure, (ii) the achievable active-material loading, (iii) the architecture of the electrode (porosity, transport paths), and (iv) the eventual scalability and manufacturability of the electrode. In the next sub-section we will examine the actual electrode architectures made possible by 3D-printing and their impact on transport phenomena and electrochemical performance.

2.3. 3D Printed Electrode Architectures and Transport–Performance Correlation

The shift from conventional planar film architectures toward 3D structural electrodes represents a paradigm change in how electrochemical transport phenomena are managed. Traditional cast electrodes often suffer from long ionic diffusion paths, poor electrolyte infiltration, and uneven electron conduction across thick electrode films. By contrast, 3D-printed electrode architectures such as lattice frameworks, interdigitated layouts, and graded-porosity scaffolds allow for intentional engineering of electron and ion pathways, thus enabling high mass loadings without sacrificing rate capability or cycling stability (Aslam, Ahsan Waseem, Zhang, & Wang, 2024)

According to Saleh et al. (2018), the implementation of a 3D-printed hierarchically porous microlattice architecture leads to a dramatic enhancement in lithium-ion battery performance compared with geometrically equivalent solid block electrodes. As illustrated schematically in Figure 2.1A, the microlattice electrode is constructed from interconnected porous truss

members, forming a three-dimensional open framework that maximizes electrolyte accessibility while preserving mechanical integrity. The corresponding SEM images (Figure 2.1B) confirm the multiscale porosity of the architecture, revealing macroscopic lattice periodicity, internal truss porosity, and micron-scale pore features that collectively increase active surface area and facilitate rapid electrolyte infiltration.

The electrochemical consequences of this hierarchical design are evident in the voltage–capacity profiles (Figure 2.1C), where microlattice electrodes with thicknesses of 250 µm and 450 µm exhibit substantially higher specific capacities and reduced polarization relative to solid block electrodes. Notably, the microlattice geometry enables up to ~4-fold enhancement in specific capacity, indicating more effective utilization of the electrochemically active material. This trend is further quantified in Figure 2.1D, which shows that the microlattice electrodes deliver both higher specific and areal capacities at comparable thicknesses, achieving approximately ~400% improvement in gravimetric capacity and ~100% increase in areal capacity over the block configuration. These results underscore how architected porosity and shortened ion/electron transport pathways in 3D microlattice electrodes can overcome diffusion limitations inherent to dense electrodes, thereby enabling high-performance thick electrodes without sacrificing capacity.

The authors attribute these gains to the controlled lattice geometry and internal porosity, which enhance electrolyte penetration, provide a high surface area for electrochemical reaction, reduce ion-diffusion distances and improve volume utilization of the active material. Furthermore, they report that the printed microlattice architecture maintained its morphology even after 40 charge/discharge cycles, demonstrating mechanical and electrochemical robustness (Saleh, Li, Park, & Panat, 2018).

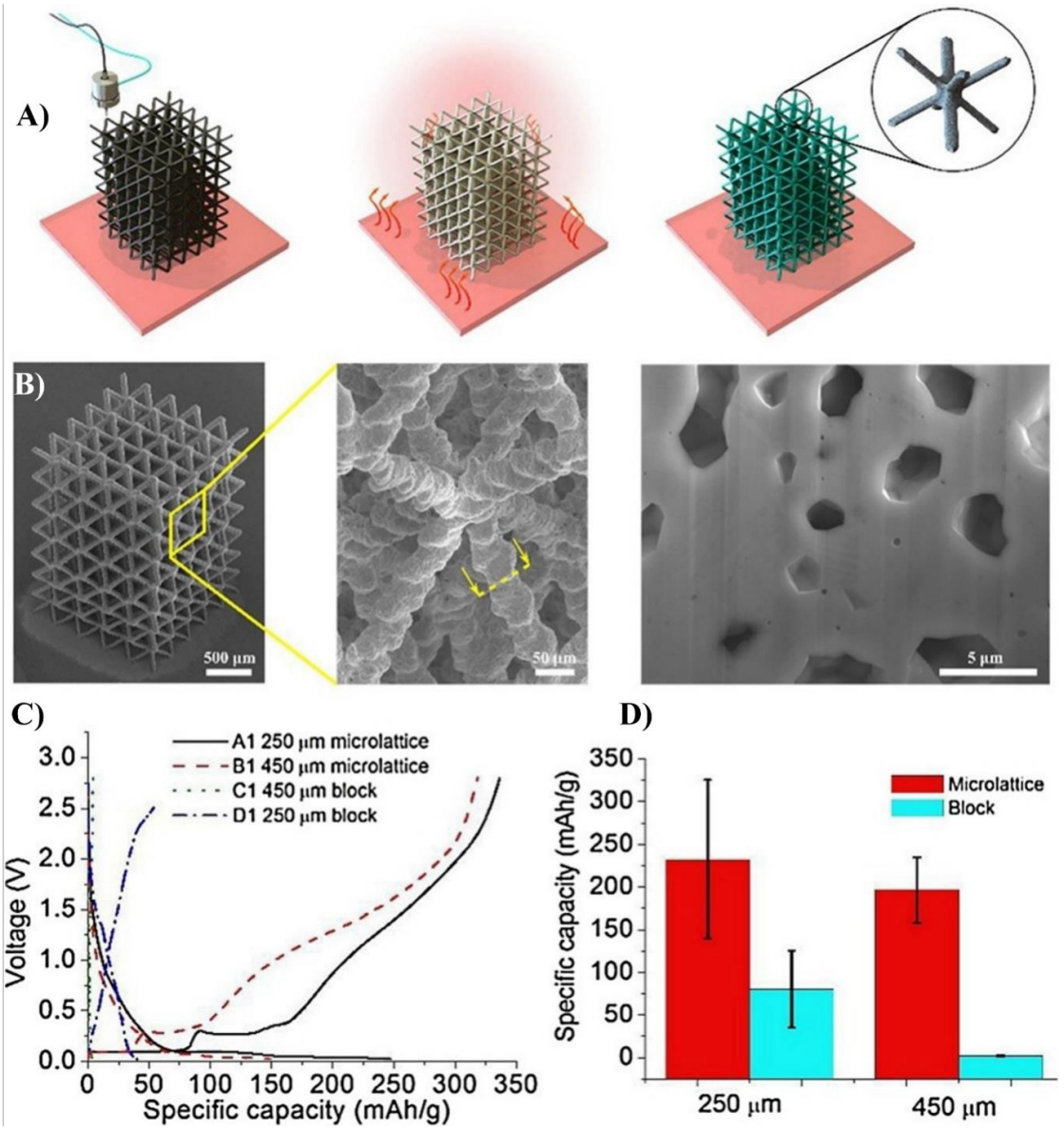

Figure 2.1. A) Schematic of the 3D-printed hierarchically porous microlattice electrode architecture (height ~250 µm) fabricated by Aerosol Jet 3D printing using porous Ag truss members. (B) SEM images of the printed microlattice structure: left – overall lattice (scale bar 500 µm), middle – magnified truss member internal porosity (scale bar 50 µm), right – high-magnification view of pore morphology (scale bar 5 µm). (C) Electrochemical performance comparison: specific capacity versus voltage for microlattice (250 µm and 450 µm) and solid block electrodes, showing ~4× higher specific capacity for microlattice. (D) Bar chart comparing specific capacities of microlattice (red) versus block (cyan) electrodes at two thicknesses (250 µm, 450 µm), reproduced after permission (Saleh et al., 2018).

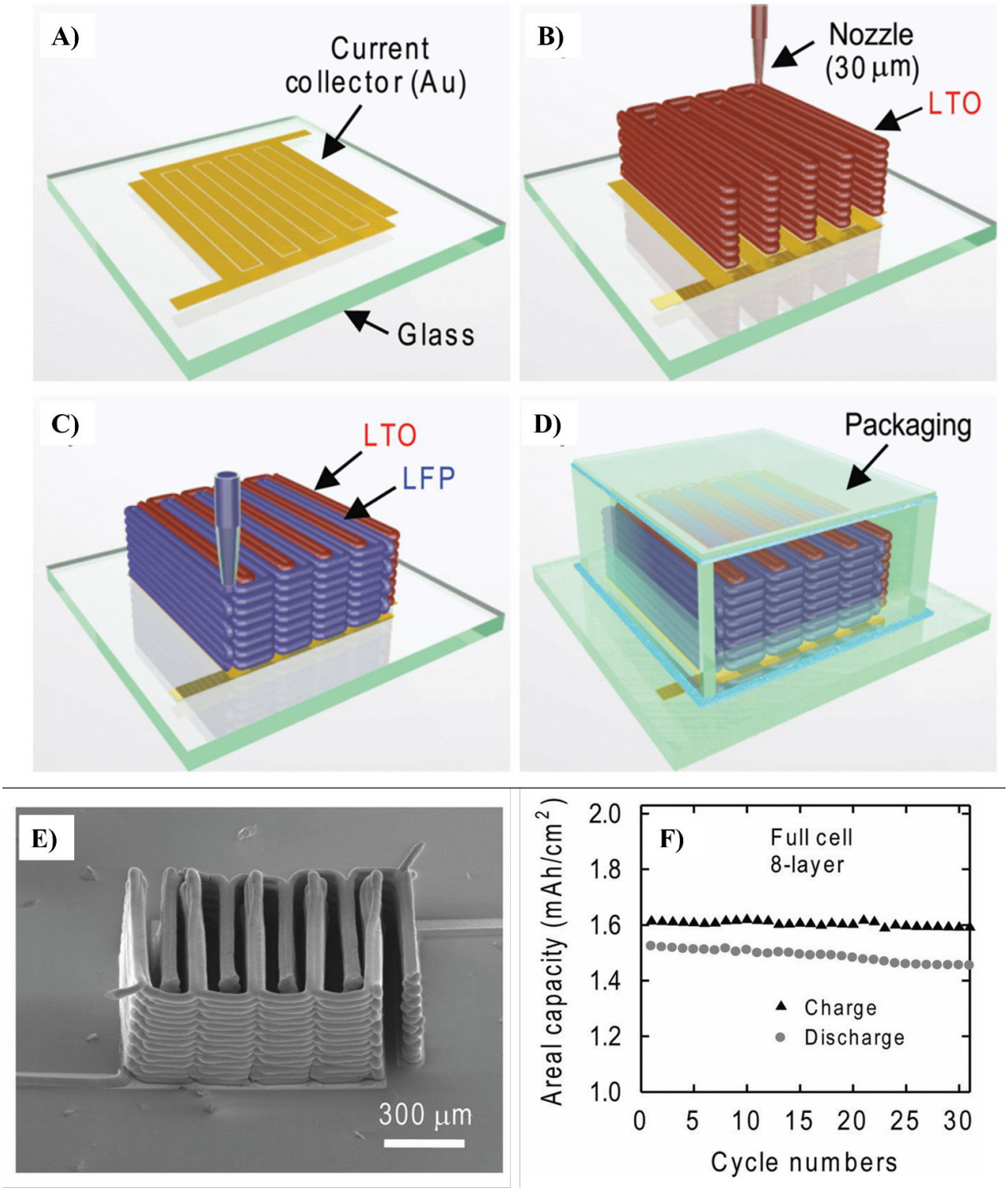

Figure 2.2. 3D-printed interdigitated Li-ion microbattery architecture and performance. (A) Patterned gold current collector on glass substrate. (B) Direct-ink-writing of LTO anode using a 30 µm nozzle.

(C) Sequential deposition of $LiFePO_4$ (LFP) cathode in an interdigitated configuration. (D) Assembled full-cell device after encapsulation. (E) SEM micrograph showing the printed 3D interdigitated electrode array with uniform layer stacking (scale bar = 300 μm). (F) Electrochemical performance of the full 8-layer cell, exhibiting stable areal charge/discharge capacities (~1.6 mAh cm^{-2}) over 30 cycles (K. Sun et al., 2013).

Figure 2.2. illustrates the fabrication strategy and electrochemical performance of a 3D-printed interdigitated lithium-ion microbattery based on LTO anode and LFP cathode architectures. As shown in Figure 2.2A, a patterned gold current collector is first defined on a glass substrate, providing a low-resistance electrical pathway and precise electrode registration. The LTO anode is subsequently deposited by direct-ink-writing using a fine 30 μm nozzle (Figure 2.2B), enabling accurate control over filament width, stacking order, and electrode spacing. This is followed by the sequential printing of the LFP cathode in an interdigitated configuration (Figure 2.2C), which maximizes electrode–electrolyte interfacial area while minimizing ion diffusion distances. The fully assembled and encapsulated microbattery device is shown in Figure 2.2D.

The structural fidelity of the printed architecture is confirmed by the SEM micrograph (Figure 2.2E), which reveals a uniformly stacked multilayer electrode array with well-defined interpenetrating channels and consistent layer alignment, essential for efficient ionic transport and mechanical stability. The electrochemical response of the resulting 8-layer full cell (Figure 2.2F) demonstrates stable areal charge and discharge capacities of approximately 1.6 mAh cm^{-2} over 30 cycles with negligible capacity fading. These results highlight the capability of additive manufacturing to precisely engineer three-dimensional interdigitated microbattery architectures that combine high areal capacity with excellent cycling stability, making them promising candidates for on-chip and microscale energy storage applications.

One of the foremost architectures is the lattice structure. In this approach, the electrode is built as a periodic truss-or strut-type network, where active material and conductive filler are deposited in a scaffold that contains macro- and meso-pores at designed dimensions. For instance, Panat et al. demonstrated a microlattice electrode with controlled porosity that dramatically improved active-material utilisation and lithium-ion transport by allowing electrolyte and Li^+ ions to access nearly the full electrode volume (Saleh et al., 2018). The

physical consequence of the lattice architecture is a shorter average diffusion length for Li^+ (both within the pore network and to the current collector) and a more uniform electric potential field, since electrons have fewer obstructions. This translates into higher rate capability and improved capacity retention under thick-electrode conditions. However, the challenge resides in ensuring sufficient packing density of active material within the lattice (to maintain energy density) while preserving mechanical stability and integrity of the scaffold during cycling.

Architectures with graded porosity provide a more subtle but effective approach. In this case, the electrode is designed to have varying porosity (and sometimes composition) across its thickness for example, a dense conductive core near the current collector to facilitate electron transport, an intermediate region enriched in active material for energy storage, and an outer layer of high porosity to ease electrolyte access and ion ingress. The purpose of grading is to decouple electronic and ionic transport constraints: electrons move efficiently through the dense core, while Li^+ ions traverse the porous outer region with minimal tortuosity and concentration polarization (Dai & Srinivasan, 2016). According to Pavlovskii et al., tailored porosity improves electrode utilisation by avoiding “dead zones” where neither electrons nor ions penetrate effectively (Alexander A. Pavlovskii et al., 2024).

Across all of these architectures, the effect on transport phenomena can be summarised as follows: (a) reduced ionic diffusion length (due to accessible pore structures and aligned channels); (b) improved electronic connectivity (through designed conductive frames and short electron paths); (c) enhanced electrolyte infiltration and wetting (via macro-porosity and graded structures); (d) minimized polarization gradients (both ionic concentration and electronic potential) across the electrode depth. For example, it has been reported that electrodes printed in a lattice format maintain nearly full utilisation of thick stacks because lithium ions reach deep regions more uniformly than in cast electrodes of equivalent thickness (Saleh et al., 2018).

In quantitative terms, one could model the effective ionic diffusion time $t_D$using $t_D \approx \frac{L^2}{D_{\text{eff}}}$, where $L$is the characteristic diffusion length and $D_{\text{eff}}$the effective diffusivity (enhanced by porosity and aligned channels). By reducing L(through architecture) and improving

D_{eff}(through tailored pore connectivity), the printed electrode reduces t_D significantly compared with random-cast designs. Similarly, electronic resistance $R_e$can be approximated via $R_e = \rho_e \frac{\ell}{A_{\text{cond}}}$, where $\rho_e$is the resistivity of the conductive network, $\ell$the average electron path length, and $A_{\text{cond}}$the cross-sectional area of the conductive network. By engineering straight, continuous conductive struts (as in lattice or interdigitated formats), $\ell$is reduced and A_{cond}effectively increased, yielding lower R_e (Fonseca et al., 2023).

In conclusion, the use of lattice, interdigitated and graded-porosity architectures in 3D-printed electrodes offers a transformative pathway for high-performance battery systems. In the context of LTO-based anodes (which inherently suffer from low electronic conductivity and moderate Li^+ kinetics), these architectures serve not merely as structural curiosities but as functional enablers that amplify the benefits of conductive additive networks and high-performance active materials. In the next subsection, we will examine how such printable architectures are specifically applied to LTO-based electrodes, the current state of research, and the opportunities ahead.

2.4. Gap Analysis and Research Opportunities

2.4.1. Summary of major knowledge gaps in LTO anode, conductive additive and printed electrode domains

In the preceding chapters we established the promise of the spinel LTO as a high-safety, zero-strain anode for lithium-ion batteries, yet we also detailed its intrinsic electronic and ionic conductivity limitations. Likewise, we explored how one-dimensional and hybrid carbon networks CNFs, CNTs, CB can dramatically improve electronic transport and inter-particle connectivity; and how advanced three-dimensional electrode architectures fabricated via 3D-printing offer new pathways to decouple thickness, increase active loadings and re-engineer transport geometry. Yet, despite these advances, there remain critical knowledge-and-application gaps at the intersections of material, additive, and manufacturing domains. These gaps must be clearly identified to define the research opportunities your thesis will exploit.

Firstly, in the LTO-anode domain, the literature consistently reports that LTO's electronic conductivity is extremely low on the order of less than 10^{-13} S cm^{-1} in pristine form (C. H. Chen et al., 2001; Yi et al., 2012). Similarly, lithium-ion diffusion coefficients within LTO are modest (~10^{-13} to 10^{-9} cm^2 s^{-1} depending on morphology). While nano-structuring, doping, coating with carbon, and composite strategies have improved these metrics, they are mostly demonstrated at low areal loadings or thin electrodes. The knowledge gap lies in how these improvements translate to high-areal-loading, thick-electrode, high-rate battery cells, where long electron/ion pathways, tortuosity effects, and mechanical constraints become dominant. Put differently: many studies show improved intrinsic LTO conductivity or kinetics, but only a few demonstrate how these enhancements survive when the electrode is scaled for practical use. This gap persists despite the known necessity of high areal loading for real applications.

Secondly, in the conductive-additive/composite engineering, although CNFs, CNTs and CB are shown to significantly reduce inter-particle resistance and form conductive networks, the systematic optimisation of these networks in the context of thick electrodes and 3D printed architectures remains under-explored (Entwistle, Ge, Pardikar, Smith, & Cumming, 2022). Many studies stop at the proof-of-concept of adding conductive nanofibres, but fewer explore the stability, integration, and manufacturability of such networks in realistic thick electrodes. In particular, the coupling between the carbon-network architecture and the 3D-printed scaffold geometry is often neglected: most carbon network studies assume traditional cast electrodes, not printed lattice or interdigitated electrodes. This mismatch forms a second major research gap (L. Sun et al., 2025).

Thirdly, in the 3D printing domain, work in this field highlights that while the geometry freedom is powerful, the technology is still nascent for high-performance lithium-ion battery electrodes, especially for anode materials like LTO. For instance, Pablo Pavlovskii et al. emphasise that the three key 3D-printing methods (material extrusion / DIW & FFF, inkjet/jetting, vat photopolymerisation) each present trade-offs in resolution, loading, and printability (Alexander A. Pavlovskii et al., 2024). Meanwhile, Maurel et al. emphasise manufacturing-oriented challenges: filament or ink formulation, binder/conductive additive content, drying/shrinkage, post-processing, and scale-up (Maurel et al., 2023). For LTO-based electrodes specifically, the number of studies that combine high active-material loading +

embedded carbon network + 3D printable architecture is limited. Thus the gap lies in the holistic integration of material (LTO), conductive network chemistry and structure (CNFs/CNTs/CB), and printable architecture with sufficient loading, connectivity and manufacturability for real-world high-power applications.

To summarize the gaps and compare across domains, Table 2.2 presents a snapshot of the major knowledge gaps.

Table 2.2. Summary of Key Knowledge Gaps Across Domains

Domain	Key Knowledge Gaps	Implications for Deliverables
LTO Anode Materials	• Extremely low intrinsic electronic & ionic conductivity (< 10^{-13} S cm^{-1}) • Few demonstrations at high areal loading / thick electrodes • Limited data on long-term cycling/fast-charge under thick electrode conditions	Without addressing this, high-power LTO remains academic
Conductive Additive / Composite	• Optimization of CNF/CNT/CB networks in thick electrodes and printed architectures • Mechanical/electrical integrity of networks over cycle life • Scale-up manufacturing of composite electrodes	If network fails or is unscalable, rate performance suffers
3D Printed Electrode Fabrication	• Ink/filament formulation with high active loading + conductive network • Integration of composite network into printed geometry • Manufacturability, throughput, post-processing	Without successful integration, printed electrodes stay lab-scale

	• Lack of full-cell data for LTO in printed format	

Given these clearly articulated gaps, the present work aims to bridge them through a three-pronged strategy that aligns material innovation, additive design, and manufacturing architecture in a unified workflow.

First, the study will develop CNF-enhanced LTO composites deliberately designed for high electronic conductivity, robust inter-particle networks, and compatibility with high areal loading. This addresses the first gap (LTO domain) and second gap (conductive additive domain) simultaneously: by embedding a well-engineered conductive network directly on/within LTO particles, the composite aims to raise conductivity to levels where high-rate performance is possible. For example, by tuning the CNF content, dispersion, interface bonding, and network topology, the composite seeks to achieve a sufficiently low charge-transfer resistance and minimal electron-hopping paths, thereby making thick electrodes viable.

Second, the research will utilise 3D-printed electrode architectures to host the CNF-LTO composites. By designing printable electrode scaffolds with tailored porosity, conductive backbone channels, and integrated carbon-network pathways, the manufacturing gap is addressed: the work will focus not just on casting electrodes but on printing electrodes that already incorporate the conductive network and active material, ensuring that the network is intrinsically embedded rather than simply added later. This addresses the third gap (3D printing domain) and its coupling with the conductive network domain.

Third, the integration of material, additive and architecture will be tested under application-relevant conditions: thick electrodes, high areal loadings, high-rate cycling, and long-term stability. By doing so, the thesis will generate data that demonstrate not only improved intrinsic properties (e.g., conductivity) but their translation into realistic performance metrics (e.g., high capacity at >5 C, low impedance growth over 100+ cycles). This bridges the gap from lab-scale proof-of-concept to meaningful system-level relevance.

In addition, the research will explore manufacturability and scalability considerations: investigating filament/pellets rheology, deposition fidelity, carbon network content vs printability trade-offs, post-processing steps and mechanical stability of printed composite electrodes. In doing so, it will provide design guidelines and process parameters that extend beyond a particular material system thereby contributing generalizable knowledge to the field.

In conclusion, although the three domains of LTO anode materials, conductive additive engineering, and 3D-printed electrode fabrication each host rich research literatures, the intersection of all three remains under-explored. The present work is specifically positioned to bridge these intersecting gaps: by creating a conductive-network-enhanced LTO composite, embedding it into a printed electrode architecture with high loading and good manufacturability, and validating its performance under realistic conditions. Through this integrated approach, the thesis aims to advance the state of the art in high-power, high-loading LTO-based anodes and move closer to practical implementation in fast-charging, high-energy lithium-ion battery systems.

In our previous research work, published as “Low-cost method to reduce interlayer voids in material extrusion: in situ layer-by-layer solvent treatment” (Iqbal, Stano, Triminì, & Percoco, 2024), I developed and experimentally validated a cost-effective in situ solvent-assisted process aimed at overcoming one of the most persistent challenges in material extrusion 3D printing the formation of interlayer voids that compromise the structural integrity and reliability of printed components. This study focused on improving interfacial adhesion and mechanical performance in FDM through a process-level innovation that did not require any hardware modification to the printing system.

In this work, I implemented a layer-by-layer solvent vapor treatment, in which the freshly deposited polymer layer was briefly exposed to a controlled atmosphere of ethyl acetate vapor before the deposition of the next layer. This treatment partially softened the surface of the printed filament, allowing molecular interdiffusion and re-entanglement of polymer chains between consecutive layers. The result was a printed structure with significantly reduced interfacial porosity and enhanced cohesive strength. Through quantitative optical microscopy and image analysis, I demonstrated that this method led to a 96 % reduction in void density and a 79 % reduction in void area, while improving the wetting factor by 34 %. Tensile testing

further confirmed a notable improvement in interlayer bonding strength (up to 40–60 %), proving the method's effectiveness in producing dense, well-fused printed components.

Beyond mechanical performance, this work offered valuable insights into solvent–polymer interaction kinetics, diffusion behavior, and layer consolidation mechanisms, which directly inform the present thesis. The layer-by-layer solvent reactivation mechanism demonstrated that the microstructural uniformity of printed polymers could be tailored by controlling the time–temperature–solvent interplay, enabling the design of dense, homogeneous matrices with consistent interfacial properties. Such process control is not only beneficial for structural applications but also critical for multifunctional devices, where mechanical cohesion and interfacial conductivity are interdependent.

This earlier research forms the technical and conceptual foundation for my current doctoral work as illustrated in Figure 2.3. The present thesis builds directly upon that process optimization framework by extending the solvent-assisted adhesion concept to multi-material and electrochemically functional systems. Specifically, while in this work I have established how interfacial bonding between inert polymer layers could be strengthened through controlled solvent diffusion, the current research explores how the same interfacial control principles can be adapted to hybrid composite electrodes containing LTO and CNFs. In these systems, maintaining intimate contact between the polymer binder, conductive additives, and electroactive particles is crucial for both electron transport and ion mobility. The solvent interaction mechanisms identified in my earlier study provide the theoretical basis for achieving such continuous networks and uniform bonding within 3D-printed energy storage architectures.

This research progression reflects a natural and deliberate evolution moving from process-level structural optimization to functional-level material integration. In the earlier work, solvent exposure was used to eliminate voids and reinforce mechanical adhesion; in the current study, it serves to ensure electrochemical continuity between functional layers and interfaces in printed electrodes. The same understanding of solvent volatility, diffusion depth, and reflow kinetics is now applied to control the deposition and consolidation of LTO–CNF composites within 3D-printed architectures. In essence, the technique that once solved a mechanical problem in polymer printing now serves as a materials-engineering strategy for embedding energy storage functionalities into printed structures.

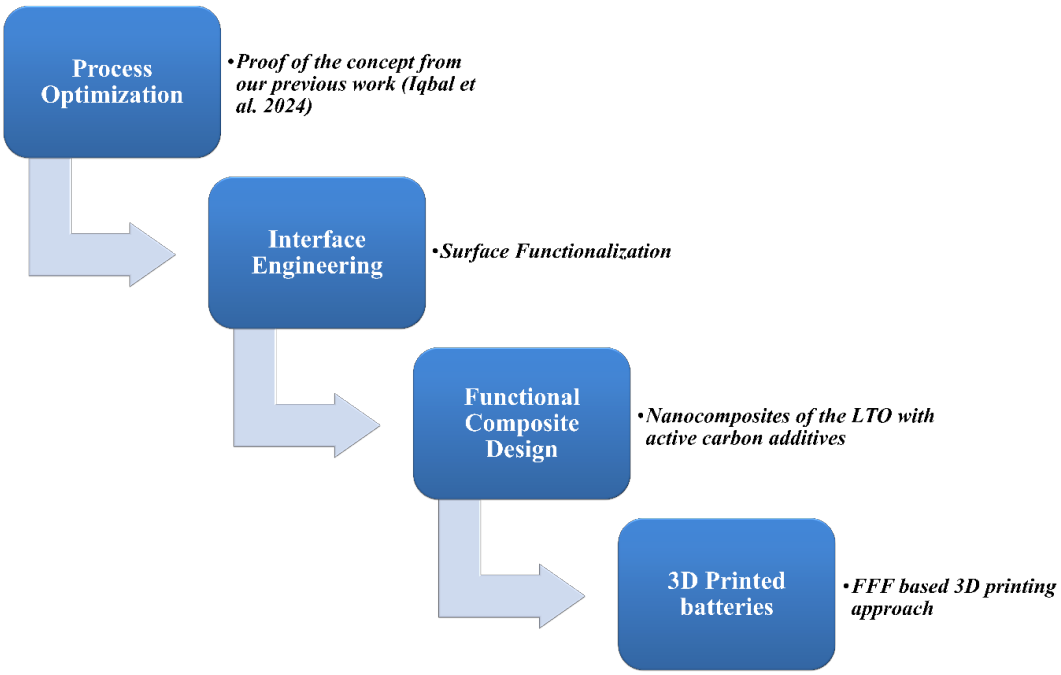

Figure 2.3. Schematic representation of research evolution pathway from process optimization to 3D printed LTO/carbon-based batteries.

Through this transition, the focus of my research has expanded from enhancing the *mechanical reliability* of printed structures to enabling their *functional integration* a shift that aligns with the overarching vision of this thesis. The lessons learned from the interlayer solvent treatment process particularly those concerning interfacial cohesion, void suppression, and solvent material compatibility now underpin the development of printable electrode formulations and composite design strategies. This correlation ensures continuity between my prior publication and the present study, linking them within a unified research trajectory that evolves from fundamental process optimization to advanced additive manufacturing for energy storage applications.

Chapter 3

Materials Selection and Experimental Methodology

Chapter 3. Materials selection and experimental methodology

3.1. Introduction

This chapter presents the materials, synthesis routes, and experimental procedures adopted throughout the research. The work was conducted in two main stages, reflecting the chronological and technical evolution of the study. The first stage focused on process optimization through solvent-assisted interlayer treatment, aimed at improving the interfacial bonding and structural integrity of material-extrusion-based printed components, as reported in previous publication (Iqbal et al., 2024). This stage provided essential insight into interlayer adhesion mechanisms and polymer–solvent interactions, forming the foundation for subsequent investigations.

The second stage of this research extended these findings towards the development of functional 3D printed battery components, particularly LTO-based composite anodes enhanced with CNFs and other conductive additives. Here, the focus shifted from purely mechanical optimization to electrochemical functionality, integrating material synthesis, filament extrusion, and additive manufacturing of energy-storing structures.

3.2 Materials and Methodology

3.2.1 Aim of the Research

The primary objective of this study was to reduce the formation of interlayer voids in parts by introducing an in situ solvent-based post-treatment using ethyl acetate (EA) vapors. The proposed method focuses on enhancing interlayer bonding between consecutively deposited layers, thereby improving the overall structural integrity and density of the fabricated components. In this research, EA was selected as the solvent for the in-situ layer-by-layer treatment owing to its favorable solvent–polymer interaction with acrylonitrile butadiene styrene (ABS), combined with its low toxicity, moderate volatility, and effective surface reflow capability. The solvent choice was made after evaluating prior literature on surface-smoothing treatments of thermoplastics, which predominantly focused on acetone-based post-processing for ABS (Lalehpour, Janeteas, & Barari, 2018; Pestano, Oliveira, & Silva, 2022; Torres, Abo, & Sugar, 2023). While acetone is widely used for vapor smoothing, its high

volatility and comparatively higher toxicity limit its suitability for iterative, layer-by-layer in-process applications.

In contrast, EA offers a balanced solvent activity sufficiently strong to induce polymer surface relaxation and partial chain diffusion, yet mild enough to avoid over-swelling or structural collapse during exposure. EA's boiling point of 77.1 °C ensures controlled vaporization at ambient temperature within a confined chamber, enabling predictable diffusion depth and repeatable results. Moreover, its lower toxicity (LD_{50} Oral, Rat: 5620 $mg \cdot kg^{-1}$) compared to acetone (5800 $mg \cdot kg^{-1}$) makes it a safer alternative for extended or repetitive in-process use (Zhu & Vesely, 2007).

3.2.2. Experimental Procedure

The *in situ* solvent treatment was integrated directly into the MEX 3D printing process. The procedure consisted of a series of sequential steps, repeated after the deposition of each layer:

1. After the extrusion of every individual layer, the printing process was temporarily paused to enable the vapor treatment phase.
2. A closed glass chamber containing EA-impregnated tissues was carefully positioned over the build plate to expose the freshly deposited polymer layer to EA vapors.
3. Prior to chamber placement, the build plate temperature was allowed to cool to room temperature (RM) to minimize premature evaporation of the solvent. This step is crucial given the boiling point of ethyl acetate (77.1 °C), as excessive heat could lead to uncontrolled vapor diffusion and inconsistent solvent exposure.
4. The treatment was carried out for a specific exposure time, determined experimentally for each sample configuration (as summarized in Table 3.1)
5. Upon completion of the prescribed exposure period, the chamber was removed from the build plate, and the printing process resumed with the deposition of the subsequent layer.

This layer-by-layer solvent vapor treatment was iteratively performed throughout the entire printing sequence, ensuring that every newly deposited layer underwent controlled exposure

to EA vapors before subsequent material deposition. The iterative treatment cycle aimed to promote partial surface softening and interlayer diffusion, ultimately reducing void formation and improving adhesion between layers.

3.3. Overview of Process Parameters

All experiments were conducted under controlled ambient conditions to maintain consistency in solvent vapor concentration and polymer behavior. The duration of exposure for each treatment step, as well as the number of treated layers, are detailed in Table 3.1. These parameters were optimized based on preliminary trials to achieve effective void reduction without causing excessive deformation or surface defects in the printed parts.

Table 3.1 Process parameters investigated for the EA vapor treatment

Sample group	Ethyl acetate / water ratio (% v/v)	Application time (min)	Total samples (3 replicates each)
A	50 / 50	4, 7, 10	9
B	75 / 25	4, 7, 10	9
C	100 / 0 (pure EA)	4, 7, 10	9

The proposed EA in situ treatment process is illustrated schematically in **Figure 3.1,** which shows the stepwise layer-by-layer application of EA vapor during the material extrusion process.

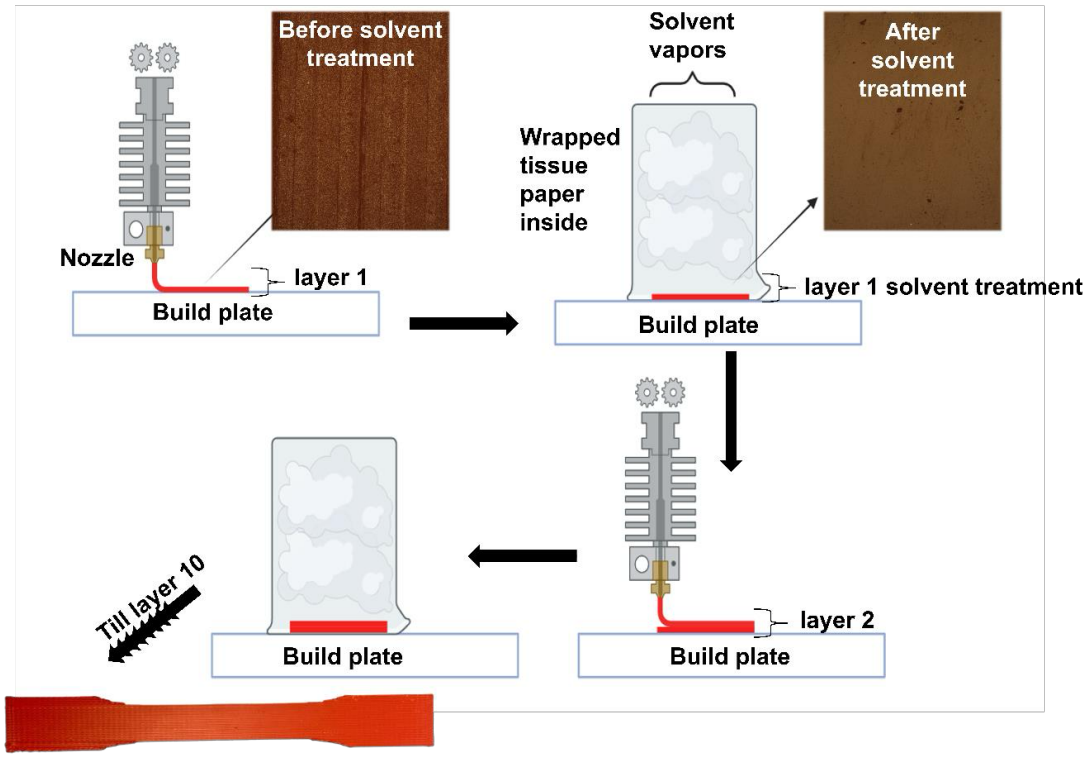

Figure 3.1. Schematic representation of the proposed layer-by-layer solvent vapor treatment.

The working mechanism underlying this technique relies on the ability of EA vapors to partially dissolve and smoothen the surface of the freshly deposited polymer layer (n). Upon exposure, the solvent softens the topmost surface, significantly reducing its surface roughness. Consequently, when the subsequent layer ($n + 1$) is extruded, the increased contact area between the two layers promotes enhanced molecular diffusion and bonding. This phenomenon leads to a substantial reduction of interlayer voids, thereby improving layer-to-layer adhesion and overall mechanical integrity of the printed components.

3.4. Solvent Application and Process Optimization

To determine the optimal solvent treatment parameters, ABS filament (eSun 3D, China) was selected as the base printing material. ABS was chosen due to its favorable mechanical properties (tensile strength ≈ 43 MPa) and its widespread use in the fabrication of low-cost

structural components. Furthermore, ABS is known to respond well to solvent-based surface treatments, a technique widely adopted for surface smoothing, particularly using acetone.

In this research, EA was selected as the treatment solvent instead of acetone owing to its lower toxicity (LD_{50} = 5620 mg/kg for EA vs 5800 mg/kg for acetone, oral, rat) and its effective solvent action on ABS surfaces. A systematic parametric study was conducted to identify the most suitable EA concentration and exposure duration for achieving optimum surface modification without inducing deformation or excessive material loss.

Three solvent concentrations (EA in aqueous solution) and three treatment times were tested, as summarized in Table 3.2. For all tests, the same volume of solution (10 mL) was used to impregnate the tissues inside the closed glass chamber, with only the EA percentage in water being varied. Each combination of concentration and exposure time was replicated three times, yielding 27 total specimens to ensure experimental repeatability and statistical reliability.

Surface roughness parameters (Ra, Rz, Rq) were measured using a Mitutoyo SJ-400 profilometer, while the surface morphology was examined with an optical microscope to assess the effect of EA vapor exposure on surface characteristics.

All samples were fabricated using a Prusa MK3 I3 3D printer (Prusa Research, Czech Republic). The slicing software PrusaSlicer was employed to generate the G-code files, which were subsequently customized to automatically pause after each layer deposition and cool down the build plate to RM prior to solvent exposure.

Table 3.2. The principal printing process parameters adopted for ABS extrusion

Parameter	**Value / Setting**	**Notes**
Infill type	Lines	Standard rectilinear pattern
Infill density (%)	100	Fully solid samples
Layer height (mm)	0.20	Uniform across all prints
Infill angle (°)	90	Alternating per layer not applied
Printing speed (mm s^{-1})	35 – 40	Depending on geometry complexity

Nozzle temperature (°C)	235	Optimized for ABS extrusion
Build-plate temperature (°C)	100	Ensures proper layer adhesion and minimizes warping

3.5. Microstructural Evaluation

To evaluate the effectiveness of the proposed *in situ* EA treatment in reducing interlayer voids, a series of controlled experiments were conducted. A total of six samples, three produced using conventional printing and three incorporating the EA vapor treatment were fabricated. Each sample consisted of ten layers with overall dimensions of 30 mm × 60 mm × 2 mm in the X, Y, and Z directions, respectively.

Following fabrication, both treated and untreated specimens were sectioned using a water-jet cutting machine to obtain two cross-sections per sample. Each section was mechanically polished to obtain a smooth observation surface. This process resulted in six cross-sections for untreated and six for treated specimens.

Cross-sectional imaging was performed using a HIROX RH-2000 digital microscope (Hirox, France) at 35× and 140× magnifications. The captured images were analyzed using Hirox RX-2000 software (version 2.0.5.0) to quantitatively evaluate void characteristics, including void count, area, and perimeter for each cross-section. These parameters were subsequently compared between the untreated and solvent-treated samples to assess the improvement in layer adhesion and void reduction achieved through the proposed EA vapor process.

3.6. Materials and methods (Part II)

This section outlines the materials, synthesis pathways, and experimental techniques employed for the development and characterization of LTO-based anodes and their integration into 3D-printed battery structures. Building upon our earlier process optimization study on solvent-assisted layer bonding (Iqbal et al., 2024), this stage of the research transitions from structural enhancement toward functional energy-storage integration. The selection of LTO as the active material stems from its outstanding structural stability, safety, and cycling

performance, while borophene and carbon-based additives such as CB, CNFs and CNTs were incorporated to overcome its intrinsic conductivity limitations.

3.6.1. Materials

All chemicals and materials used in this study were of analytical grade and employed without further purification. The primary precursors and additives utilized for the preparation of lithium-ion battery anode composites and printable filaments are summarized below. LTO powder of battery-grade spinel structure (≥ 99 % purity) was procured from Sigma-Aldrich.

3.6.1.1. Conductive additives

To mitigate the intrinsically low electronic conductivity of LTO, borophene and multiple carbonaceous additives were incorporated:

Borophene: Two-dimensional borophene nanosheets were synthesized in-house from high-purity amorphous boron powder (99 %, <5 μm) obtained from Sigma-Aldrich. Borophene was chosen for its ultrahigh electrical conductivity, chemical stability, and ability to form strong interfacial bonding with transition metal oxides.

Carbon nanofibers (CNFs): graphitized (iron-free) conical carbon nanofibers, type PR-25-XT-HHT, purchased from Sigma-Aldrich. These fibers consist of stacked conical platelets with an approximate diameter of 100 nm and a length of 20–200 μm.

Carbon nanotubes (CNTs): multi-walled CNTs (MWCNTs, > 95 % carbon basis, outer diameter 10–20 nm, length 10–30 μm) supplied by Sigma-Aldrich and used as a high-aspect-ratio conductive network former.

Carbon black (CB) : Super P conductive carbon (particle size ≈ 40 nm) obtained from Sigma-Aldrich, employed to fill micro-voids and enhance the homogeneity of the carbon network.

3.6.1.2. Polymeric binders

Two polymeric systems were investigated for filament/pellet formulation: **Poly(methyl methacrylate)** (PMMA, Sigma-Aldrich) and polylactic acid (PLA, Luminy)

were explored as structural thermoplastic matrices for composite filament extrusion and mechanical reinforcement.

Polylactic Acid (PLA): *PLA Luminy LX175 pellets* purchased to employ as polymer matrix material, and it is composed of biodegradable PLA granules derived from natural resources. PLA was selected as an eco-friendly thermoplastic matrix with excellent processability for FDM. The material exhibits low shrinkage, uniform extrusion behavior, and good adhesion to metallic and ceramic fillers, making it suitable for 3D-printed battery electrodes and separators.

3.6.2. Material Selection Rationale

3.6.2.1. Selection of PLA as the Printing Matrix

Among the various thermoplastic polymers employed in FDM, PLA was selected as the structural and printable matrix for the present study. PLA offers a unique combination of biocompatibility, biodegradability, printability, and mechanical rigidity, making it suitable for functional research on 3D-printed electrochemical devices (Chacón, Caminero, García-Plaza, & Núñez, 2017; Tymrak, Kreiger, & Pearce, 2014)

Unlike petroleum-based polymers such as ABS, polypropylene (PP), or polycarbonate (PC), which require higher processing temperatures and emit volatile organic compounds (VOCs) during extrusion, PLA can be processed at a relatively low printing temperature (≈190 °C) and under environmentally benign conditions (Ziemian, Sharma, & Ziemian, 2012). This not only simplifies the printing workflow but also reduces the risk of thermal degradation of incorporated functional fillers such as LTO, CNFs, and borophene, which can be sensitive to overheating or oxidation (Shanmugam et al., 2021).

Mechanically, PLA exhibits a high tensile strength (~59 MPa) and Young's modulus (~3.5 GPa), superior to ABS and PP, ensuring sufficient stiffness for maintaining geometric integrity in printed battery structures. Furthermore, its excellent dimensional stability, low warping, and good layer adhesion allow the fabrication of dense, uniform layers critical for maintaining interfacial contact in printed electrodes (Chacón et al., 2017; Torrado & Roberson, 2016) From a materials chemistry perspective, the polar ester functional groups in

PLA promote moderate surface energy and enhance wetting behavior with polar solvents (e.g., DMF, DCM, or NMP), favoring uniform dispersion of active particles and conductive additives within the polymer matrix. This surface polarity also aids in coating or lamination of subsequent functional layers, a feature beneficial for multi-material printing and sequential electrode deposition. Lastly, PLA's biobased origin (derived from renewable sources such as corn starch or sugarcane) and its ease of recyclability align well with the sustainability goals of next-generation additive manufacturing and green energy technologies (Chacón et al., 2017; Shanmugam et al., 2021; Torrado & Roberson, 2016; Tymrak et al., 2014).

Hence, considering its printability, compatibility with conductive fillers, eco-sustainability, and mechanical stability, PLA was selected as the preferred polymer matrix for 3D printing of battery electrodes in this study.

Table 3.3. List of materials employed in the preparation, composite formulation, and 3D printing of LTO-based electrode systems (Algarni & Ghazali, 2021; Hopewell, Dvorak, & Kosior, 2009; Khan et al., 2023; Vidakis et al., 2020).

Property	**PLA**	**ABS**	**PETG**	**Polycarbonate (PC)**	**Polypropylene (PP)**
Production base	Bio-based (corn/sugarcan)	Petroleum-based	Petroleum-based	Petroleum-based	Petroleum-based
Printing temperature (°C)	180 – 200	230 – 250	230 – 250	250 – 270	220 – 240
Glass transition temperature (°C)	55 – 65	100 – 110	80 – 85	145 – 150	−10 – 0
Tensile strength (MPa)	~59	25 – 50	45 – 50	55 – 75	20 – 40

Young's modulus (GPa)	3.5	1.1 – 2.9	2.1 – 2.4	2.0 – 2.4	1.1 – 1.6
Elongation at break (%)	6 – 10	10 – 50	10 – 25	80 – 100	200 – 700
Density (g cm^{-3})	1.24	1.04	1.27	1.20	0.90
Toxicity during printing	Non-toxic	Emits styrene vapors	Moderate	Releases BPA fumes	Low, but prone to warping
Printing difficulty	Very low	Moderate (requires heated bed)	Moderate	High	High
Dimensional stability / Warping	Excellent	Moderate	Good	Moderate	Poor
Environmental impact	Biodegradable, compostable	Non-biodegradable	Recyclable	Recyclable	Recyclable
Key advantages	Easy printing, stiff, eco-friendly	Strong, tough	Balance of strength & ductility	High strength, heat resistance	Flexible, chemical resistant
Key limitations	Brittle, lower heat deflection	Emits toxic fumes, warps	Hygroscopic	Expensive, high Tg	Poor layer adhesion

The methodology was divided into distinct yet interconnected phases: (1) Synthesis and composite formulation, involving the preparation of LTO and addition of borophene/carbon composite powders and polymer binders.

(2) Filament extrusion and printability testing, aimed at developing printable and conductive filaments compatible with fused deposition modeling (FDM) systems.

(3) 3D printing of the selected formulation

(4) Battery cell Assembly and testing for cell performance (stability etc.)

3.6.3. Synthesis of Borophene via Improved Hummers' Method

Borophene nanosheets were synthesized through a modified and improved Hummers' method, starting from high-purity amorphous boron powder (99 %, < 5 μm, Sigma-Aldrich). The method was adapted to achieve controlled oxidation, exfoliation, and reduction processes to yield few-layer borophene with metallic conductivity and high structural integrity. The synthesis sequence is illustrated in Figure 3.2.

In the first step, a mixed acid system of sulfuric acid (H_2SO_4) and phosphoric acid (H_3PO_4) in a volumetric ratio of 9:1 was prepared and cooled in an ice bath to maintain the temperature below 10 °C. This acid mixture provided both oxidative and intercalative capabilities, facilitating the partial oxidation of boron surfaces without inducing bulk combustion. Subsequently, the boron powder was gradually dispersed into the acid medium under continuous magnetic stirring for 30 min to ensure homogeneity and to promote initial surface activation of the boron particles.

Once a uniform suspension was obtained, potassium permanganate ($KMnO_4$) serving as a strong oxidizing agent was added slowly to the mixture in a 6:1 molar ratio with respect to boron, while maintaining the temperature below 20 °C to prevent rapid exothermic reactions. The slow addition ensured controlled oxidation, where Mn^{7+} ions oxidized boron to form boron–oxygen intermediate complexes. This step was followed by 6 hours of vigorous stirring under constant temperature conditions, allowing for the formation of a stable brownish dispersion indicative of boron oxide and borate intermediates.
Following oxidation, the suspension was allowed to cool to room temperature and was subsequently subjected to extensive ultrasonic exfoliation for 24 hours in deionized water. The prolonged ultrasonication step was critical for delaminating the partially oxidized boron structures, breaking down larger aggregates, and promoting the formation of ultrathin borophene nanosheets. The acoustic cavitation effect generated during ultrasonication produced localized high-energy microjets, effectively exfoliating and dispersing the boron layers into few-atom-thick sheets while maintaining their crystallinity. After exfoliation, the dispersion was washed repeatedly with deionized water until a neutral pH was reached,

followed by centrifugation at 8000 rpm to separate the solid phase from the supernatant. The obtained precipitate was then vacuum-dried at 60 °C to remove residual solvents and moisture, yielding a fine, metallic-gray borophene powder.

This synthesis route successfully converted elemental boron into two-dimensional borophene nanosheets through a sequential oxidation exfoliation reduction mechanism. The inclusion of H_3PO_4 in the acid mixture moderated the oxidation kinetics compared to conventional Hummers' methods, preventing over-oxidation and preserving the conductive metallic character of the borophene. The resulting nanosheets exhibited lateral dimensions of several hundred nanometers, thicknesses of a few atomic layers, and a high density of active edge sites.

The synthesized borophene was characterized by its distinctive metallic sheen and excellent dispersibility, confirming successful formation of 2D structures. When incorporated into LTO/CNF-based composites, the borophene acted as a two-dimensional conductive interface, improving charge transport, reducing polarization, and enhancing the mechanical flexibility of the printed electrodes.

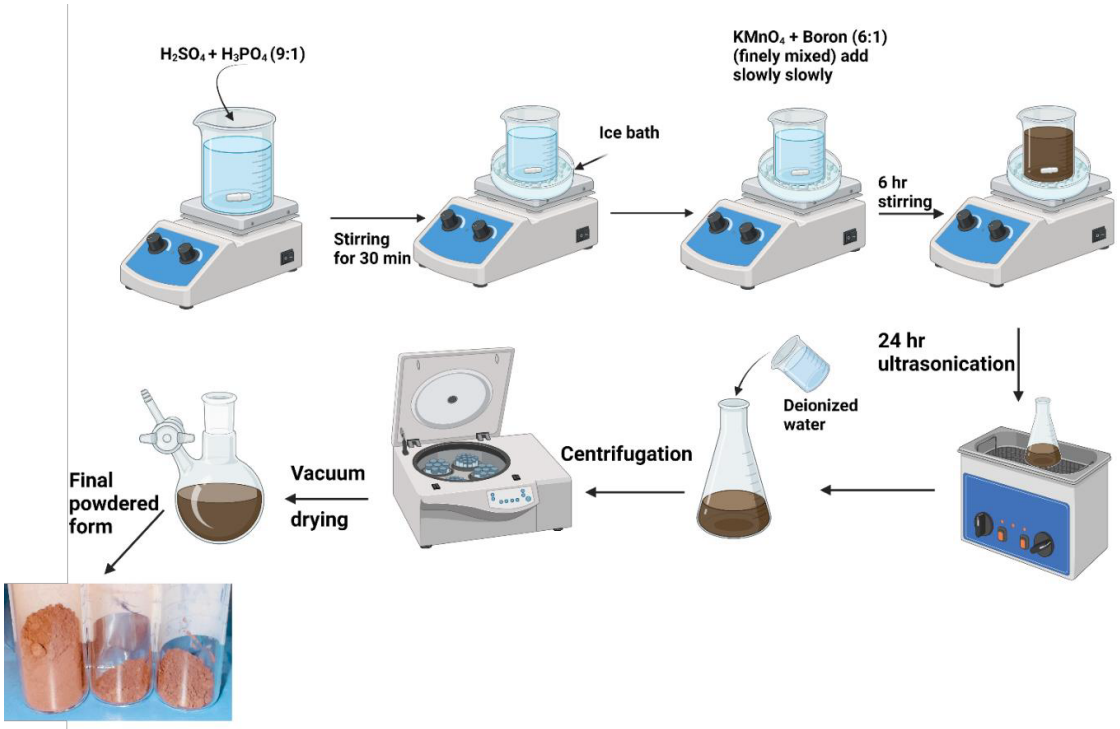

Figure 3.2. Schematic representation of the borophene synthesis procedure via the improved Hummers' method. The process involves sequential oxidation of boron in a mixed acid medium, controlled addition of $KMnO_4$, prolonged ultrasonication, centrifugation, and vacuum drying to obtain few-layer borophene nanosheets.

Fourier Transform Infrared (FTIR) spectroscopy was employed to investigate the chemical bonding and surface functionalization of the as synthesized borophene nanosheets. FTIR spectra were recorded using a JASCO FT/IR-4200 type A spectrometer operating in transmittance mode. Measurements were performed over a wavenumber range of approximately 4000−550 cm^{-1}. All spectra were baseline-corrected prior to analysis to ensure consistency and reproducibility of the acquired data.

Scanning Electron Microscopy (SEM) was employed to examine the morphology and surface features of the boron precursor and exfoliated borophene samples. SEM images were acquired using a ZEISS scanning electron microscope operated in secondary electron (SE2) imaging mode. The measurements were performed at an accelerating voltage of 15 kV with a working distance of approximately 7.5 mm. Micrographs were recorded at magnifications up to 2.0 and 2.9 kX, with corresponding scale bars as indicated in the images.

The thermal stability and transition behavior of the developed PLA + Borophene + LTO composite were analyzed using simultaneous DSC–TGA (TA Instruments SDT Q600) under nitrogen atmosphere from room temperature to 800 °C at 10 ℃ min.

3.6.4. Composite feedstock preparation for 3D-printed LTO/carbon–polymer electrodes

To establish an optimized conductive composite for 3D-printed $Li_4Ti_5O_{12}$ based electrodes, two complementary material-processing routes were implemented.

The first route (Figure 3.3A) focused on developing a printable composite filament via solvent-assisted dispersion and micro-compounding, while the second route (Figure 3.3B) centered on evaluating the intrinsic conductivity of individual additives (borophene, CNFs, CNTs, and carbon black) through uniaxially pressed pellets.

Together, these approaches ensured both the processability and electrical viability of the developed materials prior to full-scale extrusion and printing trials.

3.6.4.1. Route A – Solvent-assisted composite formulation and filament fabrication

In the first processing route, PLA pellets were dissolved in dichloromethane (DCM) under continuous magnetic stirring at 25 °C for 1 h to obtain a homogeneous polymer solution with controlled viscosity and chain mobility. DCM was selected due to its strong solvating power toward PLA and its ability to promote rapid polymer chain disentanglement, enabling the formation of a uniform polymer-rich medium. Once complete dissolution was achieved, LTO particles, few-layer borophene flakes, and a small fraction of PMMA introduced as a rheological stabilizer and film-forming aid—were gradually incorporated into the PLA/DCM solution. The suspension was further stirred for 30 min to ensure homogeneous dispersion of the ceramic and conductive phases.

This polymer-first, particle-later dispersion strategy enabled conformal coating of LTO and borophene surfaces by solvated PLA chains, effectively suppressing particle agglomeration and promoting intimate interfacial contact. The approach enhanced stress transfer across organic–inorganic interfaces and supported the formation of continuous conductive pathways upon solvent removal. Moreover, the volatile nature of DCM ensured rapid evaporation during subsequent drying, yielding a well-distributed composite microstructure without residual solvent effects. This processing route provided a robust foundation for producing mechanically coherent and electrochemically functional composite feedstocks suitable for extrusion-based additive manufacturing.

The resulting viscous slurry was cast into shallow Petri dishes and dried under ambient conditions, followed by mild oven heating (40–50 °C) to remove residual solvent. The dried composite film was then ground and fed into a micro-compounder (Xplore 15 mL twin-screw model) for filament extrusion**.**

Extrusion was performed at 150–170 °C under a 3-zone temperature gradient with a screw speed of 30–50 rpm. A uniform 1.75 ± 0.05 mm filament was obtained, with surface smoothness and mechanical integrity verified visually and through continuous laser micrometry.

The red-dashed region in Figure 3.3A highlights the extruded filament exiting the die. This

filament was later used for mechanical, rheological, and electrochemical assessments and served as the feedstock for FDM-based electrode printing.

This fabrication route was designed to maintain thermal and chemical compatibility among the components, leveraging PLA's low glass transition temperature (Tg ≈ 60 °C) and LTO's thermal robustness, while utilizing borophene's high aspect ratio and conductivity to form a percolative network through the polymer–oxide matrix. The inclusion of PMMA provided additional flexibility and printability, preventing nozzle clogging and enabling smooth deposition.

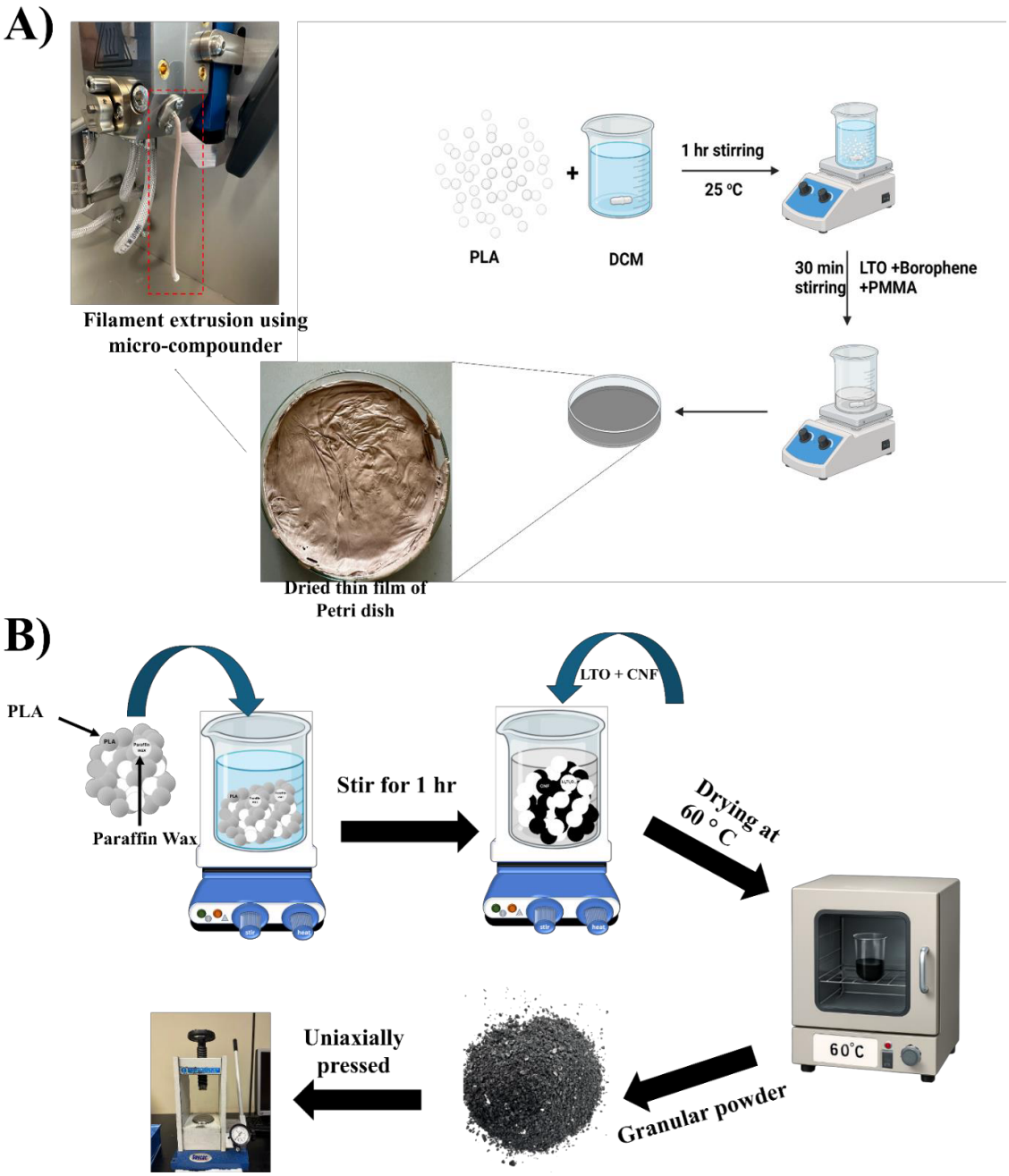

Figure 3.3. Dual-path material development strategy. (A) Solvent-assisted preparation of the LTO–borophene–PMMA–PLA composite followed by micro-compounding for filament extrusion (highlighted in red). (B) Solid-state preparation of borophene, CNT, CNF, and CB powders into uniaxially pressed pellets ("capsules") for conductivity benchmarking under 2.5–3.5 tons pressure and

60 °C drying. The combined workflow enables parallel evaluation of processability and electrical performance prior to 3D printing.

3.6.4.2. Route B – Additive pellet (capsule) preparation for conductivity evaluation

Before final selection of the conductive phase for filament extrusion, a systematic conductivity screening workflow was established based on the preparation of solid-state additive pellets ("capsules"). This approach was designed to provide a controlled and reproducible platform for evaluating the intrinsic electrical behavior of individual conductive additives under comparable compaction conditions.

Each candidate additive [borophene, CNTs, CNFs, and CB] was initially dispersed in a small volume of DCM to improve powder wetting and reduce agglomeration. The suspensions were gently stirred for 30 minutes and subsequently dried at 60 °C to remove residual solvent, yielding free-flowing powders. The dried materials were loaded into a 13 mm stainless-steel die and compacted using a uniaxial hydraulic press (Specac Atlas 15T) under an applied load of 2.5–3.5 tons for 10–15 minutes, producing mechanically stable discs with thicknesses in the range of 1–3 mm. The corresponding experimental setup is shown in Figure 3.3B.

This pelletization procedure was selected to minimize void formation, ensure consistent packing density, and establish reproducible surface–surface contact between particles, thereby enabling meaningful comparison of conductivity measurements across different additives.

The overall workflow illustrated in Figure 3.3 integrates this pellet-based screening route (Route B) with the composite filament preparation route (Route A). Route B serves as a preliminary evaluation step under well-defined and geometry-controlled conditions, while Route A translates the screened material combinations into polymer-based composite systems suitable for thermal extrusion and additive manufacturing.

In addition, the solvent-assisted processing strategy adopted in Route A was designed to remain consistent with earlier interlayer-bonding studies, where transient solvent exposure facilitates wetting between deposited strands and promotes uniform dispersion of conductive phases within the polymer matrix. This methodological continuity enables subsequent fabrication of architected printed structures, including lattices and graded-porosity designs,

using either DIW or FDM, while maintaining controlled microstructural features relevant to electrochemical applications.

3.6.5. Preparation procedure

As illustrated in Figure 3.3B, the preparation sequence involved two main stages:

1. Dry mixing and solvent-assisted homogenization, and
2. Pellet compaction under uniaxial pressure**.**

In the first stage (Figure 3.3B), the selected conductive additive (borophene or carbon nanostructures) was dispersed in a small volume of DCM to promote uniform wetting of the particles. The wet slurry was gently stirred on a magnetic plate for 20–30 minutes at room temperature to break soft agglomerates and enhance interparticle uniformity.

For carbon additives such as CNFs, CNTs, CB and borophene, similar dispersion was performed to ensure equivalent test conditions. After stirring, the mixture was partially dried in an oven at 60 °C to remove residual solvent and obtain a free-flowing granular powder. This mild drying step preserved the surface functionality of borophene (B–H and B–O groups) without causing oxidation or layer restacking.

In the second stage, the dried material was immediately transferred into a stainless-steel die set (13 mm diameter) and subjected to uniaxial pressing using a hydraulic press (Specac Atlas™ 15T). Pressing was carried out under 2.5–3.5 tons of load for 15 minutes to yield dense, mechanically stable pellets of varying thicknesses (1, 2, and 3 mm).

Figure 3.4 schematically depicts this pressing method, where the powder is confined within the die cavity and compressed between two polished punches. The diameter and pressure were kept constant, while thickness was varied to investigate the influence of compaction and path length on measured conductivity. The resulting pellets displayed uniform surfaces with no visible cracks and sufficient mechanical integrity for handling and testing.

This capsule fabrication route was implemented as a pre-screening step before advancing to composite filament extrusion and electrode printing. By compressing the pure additives into

dense pellets, it was possible to directly determine their bulk conductivity, percolation behavior, and pressure-dependent contact resistance under realistic load conditions. This is critical because the conductive behavior of nanostructured powders depends not only on their intrinsic properties but also on particle–particle contact quality, packing density, and microvoid content all of which are influenced by compaction and binder selection (S. Zhang et al., 2011). The results of these pellet tests therefore established a baseline for later comparisons with polymer composites, providing a quantitative understanding of how each additive type (borophene, CNFs, CNTs, CB) contributes to the total electronic network.

3.6.6. Pellet fabrication and measurement principle

For this evaluation, each conductive additive including borophene, CNFs, CNTs, and CB was separately pressed into self-supporting pellets under uniaxial pressure using a manual hydraulic press (Specac Atlas™ 15T).

Approximately 0.3–0.5 g of each additive powder was loaded into a 13 mm stainless-steel die and compacted under 2.5–3.5 tons of pressure for 15 minutes to ensure particle densification and minimize interparticle voids.

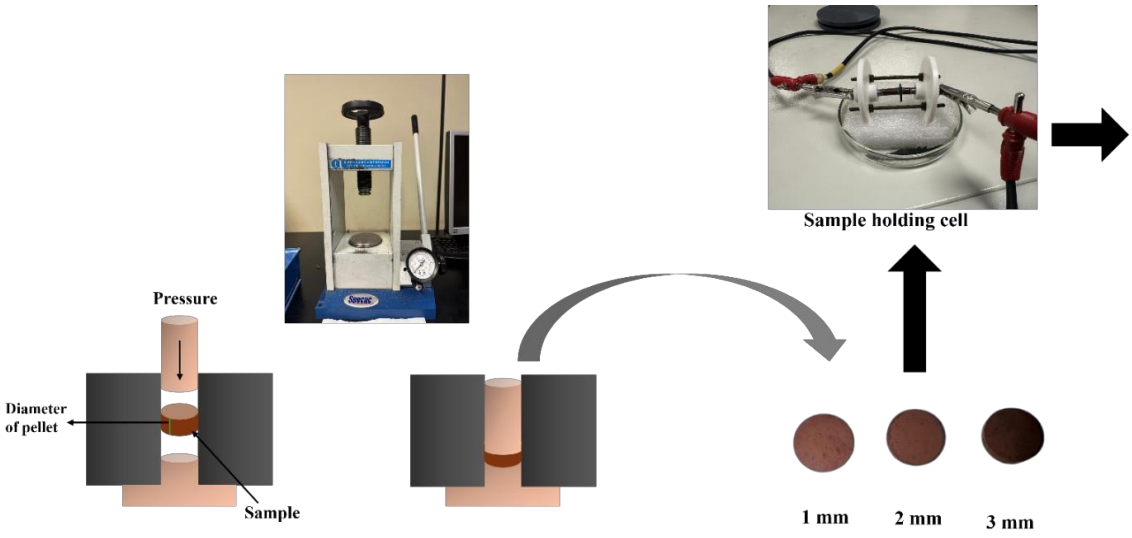

Schematic draft of the uniaxial pressing method

Pellets of different thickness

Figure 3.4. Schematic illustration and photographs of uniaxially pressed borophene/carbon additive pellets prepared under 2.5–3.5 tons for 10–15 min. Pellets of different thickness (1–3 mm) were used to evaluate conductivity as a function of compaction and additive content

The resulting pellets (1–3 mm thickness) were uniform, mechanically stable, and suitable for two-probe conductivity testing. Thickness variation was intentionally allowing assessment of how bulk compaction and density influence electrical resistivity. The schematic representation of this process (Figure 3.4) illustrates the uniaxial pressing setup and the resulting pellets of different thicknesses.

The terminology "pellet" is technically correct here in materials science, it denotes a compacted disc used for physical property testing, distinct from extruded or sintered bodies. This pelletization approach offers a reliable first indication of the intrinsic electronic conductivity and interparticle contact efficiency of the additive powders prior to polymer or composite integration.

3.6.7 Conductivity Measurement

Electrical conductivity (σ) of the pressed additive pellets was measured by determining their bulk electrical resistance (R) using a two-point probe configuration. Pellet samples were placed between two conductive electrodes to ensure full surface contact during measurement. The electrical conductivity was calculated according to:

$$\sigma = \frac{L}{R \times A} \ldots\ldots\ldots (13)$$

where L is the pellet thickness (cm) and A is the cross-sectional area (cm^2).

For each composition, measurements were repeated at least three times to ensure reproducibility, and the average value was reported. Conductivity measurements were performed for pellets containing different weight fractions of conductive additives. The resulting conductivity values were subsequently plotted as a function of additive weight fraction to assess the evolution of electrical transport behavior with increasing filler content. For graphical representation, conductivity data were displayed using a logarithmic scale to accommodate the wide dynamic range typically observed in polymer-based composite systems.

3.6.8. Scientific significance of this step

Performing conductivity measurements on these pressed additive pellets was a strategic pre-screening step. Before advancing to filament extrusion and electrode printing, it was essential to determine which additives offered superior conductivity and compaction behavior under mechanical stress as this predicts how well they will percolate when embedded in the polymer matrix.

This method provided direct insights into:

- **Intrinsic electrical response** of each additive (CNFs > CNTs > CB > borophene);
- **Effect of compaction pressure and pellet thickness** on electron pathway formation;
- **Baseline conductivities** used later to correlate with composite and printed electrode performance.

Consequently, the pellet testing phase served as a benchmark experiment confirming that while CNTs and CNFs deliver the highest bulk conductivities, borophene's layered morphology and strong interfacial coupling capability make it a promising co-additive for synergistic enhancement in hybrid LTO–carbon–boron systems.

3.6.9. Initial Composite Formulation and Extrusion Feasibility for 3D-Printed Battery Electrodes

The next stage of this research aimed to assess the extrusion and printability feasibility of polymer–ceramic nanocomposites designed for 3D-printed lithium-ion battery electrodes. The work focused on establishing a formulation that simultaneously achieves high electronic conductivity, derived from percolating conductive additives, and adequate mechanical processability, required for consistent filament extrusion and layer deposition.

The preliminary composition consisted of PLA as the biodegradable thermoplastic matrix, LTO as the active anode material, and a series of conductive additives; borophene, CNFs, CNTs, and CB investigated independently to understand their impact on rheology, extrusion

stability, and composite homogeneity. The additive selection was guided through conductivity measurement all four materials demonstrated distinct percolation behaviors and electrical responses. Borophene displayed a promising conductivity rise near 8 vol %, but its mechanical rigidity and low ductility rendered it less suitable for continuous extrusion. Conversely, CNFs and CNTs achieved excellent conductivity at lower loadings while maintaining structural cohesion and flexibility, suggesting their potential as superior candidates for printable composite systems.

3.6.9.1 Composite formulation strategy

Based on the conductivity benchmarking, the PLA content was tested with multiple concentrations to see the extrusion behavior of the synthesized formulation and maintained within 25–30 wt % of the total mass, depending on the additive concentration. The remainder comprised active LTO particles and the selected conductive additive, whose fraction systematically varied between 1 wt % and 9 wt % to explore its influence on both electrical and rheological properties. The formulation strategy sought a delicate equilibrium: minimizing the polymer fraction to maximize electroactive and conductive loading while preserving enough polymeric matrix to sustain melt elasticity and filament continuity.

All powders were pre-dried under vacuum prior to processing (PLA at 55 °C; LTO and additives at 80–100 °C for 12 h) to eliminate absorbed moisture and prevent hydrolytic degradation during melt compounding. To enhance dispersion, a “polymer-first wetting” technique was used: a small sub-portion of PLA pellets was dissolved in DCM under stirring at room temperature, followed by the gradual addition of the conductive additive to promote surface wetting and reduce agglomeration. After solvent evaporation, the dried pre-mix was blended with the remaining PLA and LTO and introduced into the extruder for melt compounding.

Initial extrusion was performed using a twin-screw micro-compounder equipped with a 1.75 mm circular die to assess the homogeneity, torque stability, and strand-forming capability of each formulation. Processing temperatures were optimized in the 175 °C, with screw speeds of 100 rpm and residence times of 5 minutes to ensure uniform shear dispersion while avoiding thermal degradation of PLA.

3.6.9.2. MFI-based flow evaluation and rheological correlation

After the initial micro-compounding trials, quantitative rheological characterization was conducted using a melt-flow-index (MFI) analyzer to assess flow behavior under controlled thermal and load conditions. This stage was performed at a subsequent research facility equipped with advanced melt rheology instrumentation, enabling more precise evaluation of extrusion feasibility across formulations.

MFI tests were carried out at 180 °C, applying loads of 2.16 kg, 3.8 kg, and 5 kg to simulate low-, medium-, and high-stress extrusion conditions, respectively. The melt-flow rate (MFR) and time-dependent flow stability were recorded to evaluate viscosity sensitivity and identify an operational processing window suitable for filament extrusion. The results revealed that CNF and CNT-filled composites maintained stable and continuous flow across the medium-pressure range (3.8 kg), indicating favorable shear-thinning behavior typical of pseudoplastic polymer–particle suspensions. At higher loads, slight die-swell and local overheating were observed, suggesting that further optimization of cooling and take-up speed would be necessary for continuous filament production.

Borophene-based composites, however, displayed a narrower processing window: they flowed inconsistently at low pressures and exhibited sudden torque fluctuations at higher loads, confirming poor melt cohesion despite excellent electrical connectivity. CB-filled samples displayed intermediate behavior but required extended residence times to achieve homogenization, potentially compromising thermal stability.

These findings highlighted that the MFI data correlated strongly with the mechanical observations from micro-compounding, validating the importance of rheological evaluation in predicting extrusion performance for functional composites. The extrusion and MFI results demonstrated that achieving functional printability requires balancing conductivity with melt cohesion. The borophene and other high-aspect-ratio fillers formed efficient conductive networks but induced brittle fracture and poor layer fusion, as confirmed by the cracked filament morphology. These findings highlighted the need for rheological tuning specifically, improving the polymer–particle interfacial compatibility and enhancing the viscoelastic elasticity of the melt.

Table 3.4. Comparison of electrical and extrusion characteristics for PLA/LTO composites containing different conductive additives.

Conductive Additive	**Electrical Conductivity (S cm^{-1})(at ~8 wt %)**	**Extrusion / MFI Stability**	**Filament Surface Morphology**	**Mechanical Flexibility**	**Dispersion Quality**	**Overall Printability Assessment**
CNF	**~0.09 – 0.10**	Stable, shear-thinning flow at 3.8 kg; minimal die swell	Smooth surface, occasional micro-pits	Flexible; continuous filament formation possible	Excellent (uniform fiber dispersion)	Best overall balance of conductivity and extrusion quality
CNTs	~0.03	Slight flow oscillations at higher pressure	Minor surface irregularities	Moderately flexible	Good, but requires sonication to prevent clustering	Good printability with optimized processing
CB	~0.016	Stable but high viscosity; slower flow rate	Smooth surface but thicker strand	Fair; limited elongation	Excellent	Processable but lower conductivity at equal loadings
Borophene	**~9 × 10^{-4} – 1 × 10^{-3}**	Unstable at high load; torque fluctuations; inconsistent flow	Severe longitudinal cracks and surface fissures; voids visible	Very brittle; fractured easily during winding	Moderate (platelet aggregation observed)	Lowest conductivity and poor mechanical printability

The next stage of the study therefore focused on modifying the composite formulation through rheology-control additives to mitigate brittleness, improve layer adhesion, and enable the production of continuous, flexible filaments suitable for 3D printing.

3.6.10. Incorporation of Binder and Transition to Pellet Printing

Following the extrusion feasibility study of PLA/LTO composites incorporating conductive additives, CNFs were selected as the fixed conductive phase at a loading of 8 wt% for subsequent formulation development. To improve melt processability and filament handling characteristics, a low-temperature binder phase, paraffin wax (PW), was introduced into the composite system.

Paraffin wax was selected due to its lubricating and plasticizing properties, low melting temperature (≈55–65 °C), and compatibility with both the PLA matrix and ceramic fillers. Its incorporation was intended to modify the melt rheology by reducing elastic stresses during extrusion and enhancing flow stability, while preserving the conductive network formed by CNFs and the electrochemical functionality of the LTO phase. The CNF content was maintained at 8 wt%, while the paraffin wax fraction was systematically varied between 6 wt% and 14 wt% to explore a suitable processing window. The remaining composition consisted of PLA and LTO, adjusted accordingly.

Composite preparation was carried out using a wet-chemical dispersion route rather than melt compounding. PLA pellets were first dissolved in DCM at room temperature under magnetic stirring to obtain a homogeneous polymer solution. In parallel, LTO and CNF powders were dispersed in DCM containing molten paraffin wax to promote uniform surface wetting. The two suspensions were then combined under vigorous stirring to form a stable composite slurry, in which paraffin wax functioned as a binder, lubricant, and secondary plasticizer. Continuous stirring was maintained to ensure homogeneous dispersion and de-agglomeration of the particulate phases. The resulting slurry was subsequently dried to remove solvent, yielding a composite powder suitable for further processing Figure 3.3B.

Rheological behavior of the prepared composites was assessed using MFI measurements conducted under standard loads of 2.16, 3.8, and 5 kg. Extruded strands obtained during MFI testing were examined qualitatively for diameter consistency, surface continuity, and flexibility to assess their suitability for downstream processing.

Based on the outcomes of the extrusion trials, the fabrication strategy was transitioned from filament-based extrusion to a pellet-based additive manufacturing approach. In this route, the compounded material is either pelletized after drying or used directly as granulated powder, served as the feedstock for pellet-fed 3D printing. This approach avoided a dedicated filament production step and reduced repeated thermal and mechanical loading of the composite material.

During pellet-based printing, material flow and deposition behavior were governed by the shear environment within the pellet extruder and nozzle. Paraffin wax contributed to flow consistency and interfacial wetting during deposition. Printed specimens were subjected to a post-processing thermal conditioning step at 80 °C for 30 minutes to promote paraffin redistribution and stabilize interfacial bonding prior to subsequent characterization.

3.6.11. Fabrication of 3D Printed Electrodes via FDM

After the successful extrusion and printing of composite electrodes, a solvent-mediated post-treatment was performed to remove the PW binder and activate the printed electrodes for electrochemical applications. While the inclusion of PW during printing significantly improved flow stability and filament formation acting as a temporary plasticizer and mechanical binder it remained electrically insulating and chemically inert toward the electrochemical environment. Therefore, a selective removal step was implemented to both enhance porosity and prepare the electrode for lithium-ion transport.

The as-printed electrodes (18 mm diameter, 0.87 mm thick) were immersed in analytical-grade n-heptane at room temperature for 2 hours in laboratory environment. Heptane was selected for its non-polar character and high affinity for paraffin-based hydrocarbons, allowing for selective dissolution of the wax phase while preserving the PLA polymer matrix and embedded LTO/CNF framework. This choice was guided by solvent compatibility charts and earlier reports on paraffin extraction from polymeric composites (Gulzar, Glynn, & O'Dwyer, 2020; Son, Kim, Choi, & Lee, 2024; K. Zhang et al., 2024).

During soaking, the solvent gradually penetrated the printed matrix, dissolving the PW fraction and producing microscopic effervescence as trapped air escaped from emerging pores. The electrodes were then retrieved using PTFE tweezers, rinsed twice with fresh

heptane, and placed on absorbent paper to remove excess solvent. Subsequently, they were dried at 60 °C for 3 hours to ensure complete solvent evaporation. This process yielded mechanically stable, wax-free electrodes with visibly darker coloration and a slightly matte surface evidence of wax depletion and emerging micro-porosity. Minimal shrinkage (<2% in diameter, <3% in thickness) was recorded, confirming that the PLA backbone retained its dimensional stability after solvent exposure.

These 3D printed electrodes were used directly for half-cell assembly against lithium metal. The test configuration employed CR2032 coin cells, Celgard 2400 separators, and 1 M $LiPF_6$ as the electrolyte. This post-treatment was found to be critical in transforming the mechanically printable composite into a functional, electrochemically active electrode suitable for energy storage evaluation, these results has been elaborated in results section.

3.6.12. Determination of Porosity by Archimedes Method

The porosity of the wax-extracted 3D-printed LTO/PLA/CNF electrode was determined using the Archimedes buoyancy principle, a widely established technique for estimating the open and closed pore volume in solid materials. This test was performed on a heptane-treated electrode, in which paraffin wax was completely removed to expose the porous framework of the composite. Because the electrode was inherently porous and could absorb water during immersion, a polymer spray coating was applied to create a thin, impermeable film around the specimen. The coating prevented fluid infiltration into internal pores and ensured accurate volume determination. The entire procedure was carried out under controlled laboratory conditions (25 ± 2 °C).

The Archimedes method was implemented as follows:

1. The dry, uncoated electrode was weighed in air to record its mass w_1.
2. The sample was coated with a thin layer of polymer spray in a fume hood and allowed to dry completely; this coating provided a sealing barrier during submersion.
3. The coated mass in air was then measured as w_2.
4. The coated specimen was gently submerged in distilled water using a fine wire hook to measure its apparent mass in water, w_3.

5. The density of the coated polymer (ρ_c) and that of water (ρ_w) were taken as 1.10 g cm^{-3} and 1.00 g cm^{-3}, respectively.

Since the coating adds extra volume and mass, a correction term was applied to remove its contribution. The effective volume of the original porous specimen was calculated by:

$$V_{\text{bulk}} = \frac{w_2 - w_3}{\rho_w} - \frac{w_2 - w_1}{\rho_c} \qquad \text{..... (14)}$$

3.6.17. Morphological Characterization (SEM)

The morphological features and microstructural evolution during the different stages of 3D-printed electrode fabrication were examined again using Scanning Electron Microscopy (SEM) (JEOL JSM-IT200) operated at an accelerating voltage of 15 kV in secondary electron imaging mode. This analysis aimed to systematically compare the morphology of (a) the pristine $Li_4Ti_5O_{12}$ (LTO) powder, (b) the extruded composite filament, and (c) the final 3D-printed LTO/CNF/PLA electrode after solvent removal. Through this sequential characterization, the progressive changes in particle distribution, interfacial bonding, and porosity induced by the extrusion and post-processing steps could be clearly observed, providing insight into the structural optimization achieved through the integrated printing and activation process.

3.6.18. Assembly of Li/LTO Half-Cells Using 3D-Printed Electrodes

After solvent-assisted removal of paraffin wax to generate the desired porous microstructure, the optimized 3D-printed CNF/LTO/PLA composite anodes were assembled into CR2032-type coin cells for electrochemical testing.

All assembly steps were performed inside an argon-filled glovebox (Jacomex Glove Box, O_2 and H_2O < 0.1 ppm) to prevent exposure of lithium to moisture and oxygen, as both react aggressively with ambient air, forming LiOH and Li_2O films that can degrade interfacial performance.

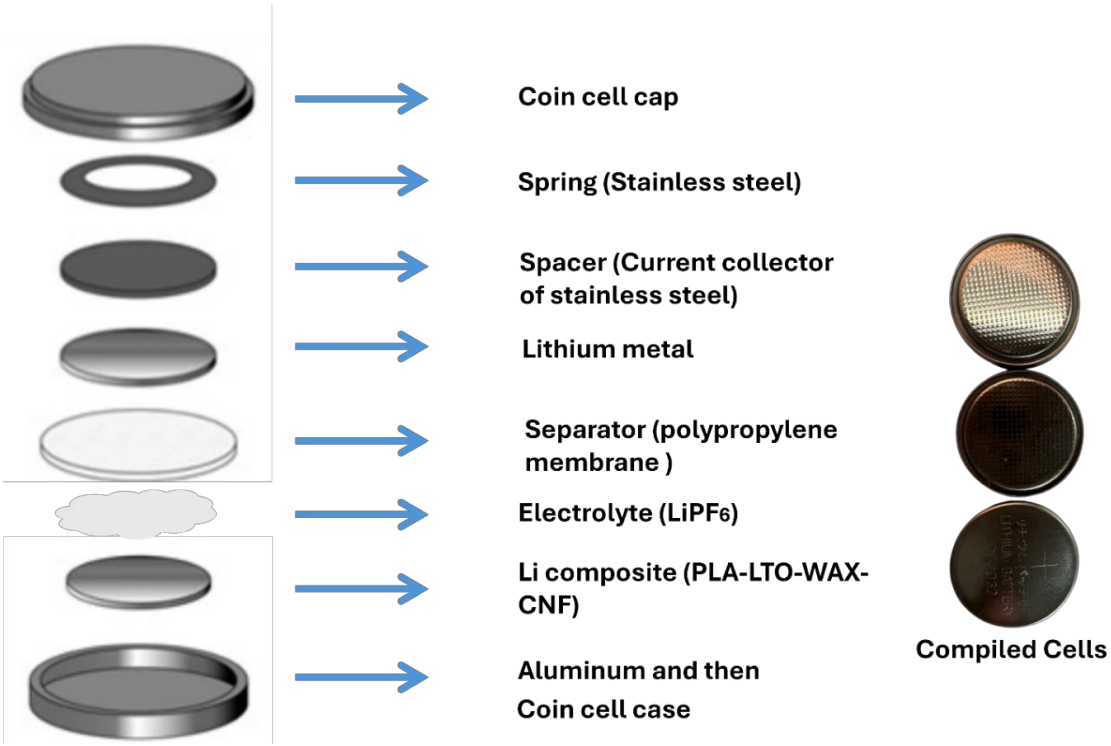

Figure 3.5. Step-by-step illustration of the coin-cell battery assembly process, highlighting the sequential stacking of the casing, electrodes, separator, gasket, and current collectors to form the final sealed cell.

Each coin cell comprised the following elements, stacked sequentially as illustrated in **Figure 3.5** above**.**

1. **Coin-cell case (bottom cup)** : aluminum housing cleaned ultrasonically in ethanol and dried under vacuum at 60 °C.
2. **3D-printed electrode (working electrode)** : printed LTO–PLA–CNF composite disk (~18 mm diameter, ~0.35 mm thick_later printed again to reduce the thickness) used directly without calendaring; positioned on the aluminum current collector.
3. **Separator** : Celgard 2400 polypropylene membrane (19 mm diameter) placed atop the printed electrode.
4. **Electrolyte** : 1 M $LiPF_6$ drop-casted (≈80–100 µL) onto the separator to ensure full wetting.

5. **Counter/reference electrode** : high-purity lithium metal foil (16 mm diameter) placed above the separator.
6. **Spacer and spring** : stainless-steel components ensuring uniform pressure and consistent electrical contact.
7. **Coin-cell cap** : sealed using a hydraulic crimping tool inside the glovebox to prevent electrolyte evaporation.

All cells were left to rest for 24 h before electrochemical measurement to ensure electrolyte soaking and SEI stabilization on the lithium surface.

This configuration represents a Li/LTO half-cell**,** where the 3D-printed composite acts as the working electrode and metallic lithium as both counter and reference electrode.

3.6.19. Electrochemical Characterization of 3D-Printed Electrodes

The electrochemical performance of the assembled Li/LTO half-cells (containing the 3D-printed CNF/LTO/PLA electrode) was evaluated using a Neware BTS-4000 battery testing system. All measurements were carried out at room temperature (25 ± 1 °C). The testing protocol consisted of sequential galvanostatic charge/discharge (GCD) cycles, performed within a potential window of 1.0–2.5 V vs. Li/Li^+, corresponding to the redox couple Ti^{4+}/Ti^{3+} in $Li_4T_5O_{12}$.

Cells were cycled at various current densities corresponding to C/25, C/12.5, C/8, C/4, and C/2 rates, where 1 C = 175 mA g^{-1} based on the theoretical capacity of LTO. Each current step was maintained for at least ten cycles to evaluate rate capability and recovery performance, followed by long-term cycling at C/25 to assess capacity retention and CE.

The specific capacity ($mAh\ g^{-1}$) was calculated based on the mass of active material in the printed electrode, which comprised ~35 wt % of the total electrode mass. CE was determined according to:

$$\mathbf{CE} = \frac{\textbf{Discharge Capacity}}{\textbf{Charge Capacity}} \times \mathbf{100} \quad \textbf{…….. (15)}$$

3.7. Conclusion

This chapter has established the experimental and material-design foundation for the fabrication of 3D-printed lithium-ion battery electrodes by systematically developing, validating, and rationalizing polymer–ceramic–carbon composite feedstocks compatible with material-extrusion additive manufacturing. In line with the restructured thesis organization, the focus of this chapter has been on methodological development and process optimization, providing the necessary framework upon which electrochemical performance and device-level behavior are later evaluated.

Two central methodological objectives guided the work presented herein. The first was the enhancement of interlayer cohesion and structural integrity in extrusion-printed polymer systems through solvent-assisted post-processing. The second was the formulation of electrically conductive, extrusion-grade composite filaments capable of accommodating high ceramic loadings while maintaining printability and mechanical robustness.

The optimization of EA vapor treatment was first addressed as a model strategy to control interfacial bonding in printed polymer architectures. By systematically tuning solvent concentration and exposure time, the treatment protocol was refined to promote polymer chain mobility and interdiffusion across printed layers, thereby mitigating interlayer void formation and surface roughness. This approach provided a mechanistic basis for solvent–polymer interaction control, establishing a transferable methodology for improving the structural quality of printed components prior to functional composite development.

Building upon this structural framework, the chapter then transitioned to the formulation of functional LTO-based composite feedstocks. A comparative screening of conductive additives including borophene, CNTs, CB, and CNFs was conducted to evaluate their influence on electrical percolation, rheological behavior, and extrusion stability. Among the investigated fillers, CNFs emerged as the most suitable conductive phase, offering a favorable balance between electronic connectivity and mechanical compliance. This selection was driven not by conductivity maximization alone, but by the need to preserve process reliability and filament integrity, which are critical constraints in filament-based additive manufacturing.

Rheological and melt-flow characterization confirmed that CNF-reinforced LTO–PLA composites exhibit stable shear-thinning behavior under representative extrusion conditions, validating their compatibility with fused filament fabrication. To further improve processability and suppress extrusion-induced cracking at high ceramic loadings, PW was introduced as a temporary processing aid. The inclusion of PW reduced melt viscosity, improved filler dispersion, and enhanced filament cohesion during printing. Thermal analysis demonstrated that PW undergoes controlled melting and evaporation below the printing temperature, ensuring that its role remains confined to processing assistance rather than long-term structural contribution.

The optimized composite formulation comprising approximately 52 wt% LTO, 28 wt% PLA, 8 wt% CNF, and 11–12 wt% PW represents a methodologically validated feedstock design, balancing ceramic loading, conductive network formation, and extrusion stability. Importantly, the chapter explicitly recognizes PW as an electrically inactive phase, necessitating its removal in subsequent processing steps, which are addressed in later chapters. This deliberate separation of processing optimization from electrochemical activation reinforces the methodological clarity of the thesis.

In summary, this chapter provides a robust and reproducible methodological platform for the additive manufacturing of ceramic-based battery electrodes. By decoupling structural optimization, conductive network design, and processability enhancement, the work establishes clear design rules for composite feedstock development in 3D-printed energy storage systems. These methods form the essential foundation for electrochemical evaluation, performance benchmarking, and device-level demonstrations presented in the subsequent chapters.

Chapter 4

Results and Discussion

Chapter 4. Results and Discussion

4.1. Roughness Analysis and Optimization of Solvent Parameters

To identify the optimal parameters for the in-situ solvent-assisted layer treatment, a series of single-layer ABS specimens were fabricated and subjected to controlled EA vapor exposure at varying concentrations (50 %, 75 %, 100 %) and treatment durations (5, 7, 10 min). The resulting surfaces were analyzed using a profilometer to determine the arithmetic mean roughness (Ra). Figure 4.1. shows the correlation between Ra and treatment time for the three EA concentrations, while Table 4.1 summarizes all measured values. The results clearly indicate a progressive decrease in surface roughness with increased treatment time. The transition from 5 to 7 min produced the most pronounced improvement (Ra reduction of ≈ 60 %), whereas extending treatment to 10 min yielded marginal additional benefit, suggesting a surface-diffusion equilibrium had been reached.

Furthermore, solvent concentration exerted a limited effect once vapor saturation was achieved. Increasing EA from 50 % to 75 % slightly reduced Ra, but further increase to 100 % produced negligible additional smoothing. This is attributed to chamber vapor saturation, in which a threshold concentration already ensures full polymer-surface softening. Optical micrographs Figure 4.2 complemented by grayscale-converted images and qualitative layer analysis, support this conclusion: samples treated with 75% EA exhibit a smoother and more homogeneous surface morphology than those treated with 100% EA. This behavior is consistent with observations by Mu et al [42] who reported that moderate solvent concentrations promote more uniform solvent penetration while avoiding excessive swelling or prolonged drying effects.

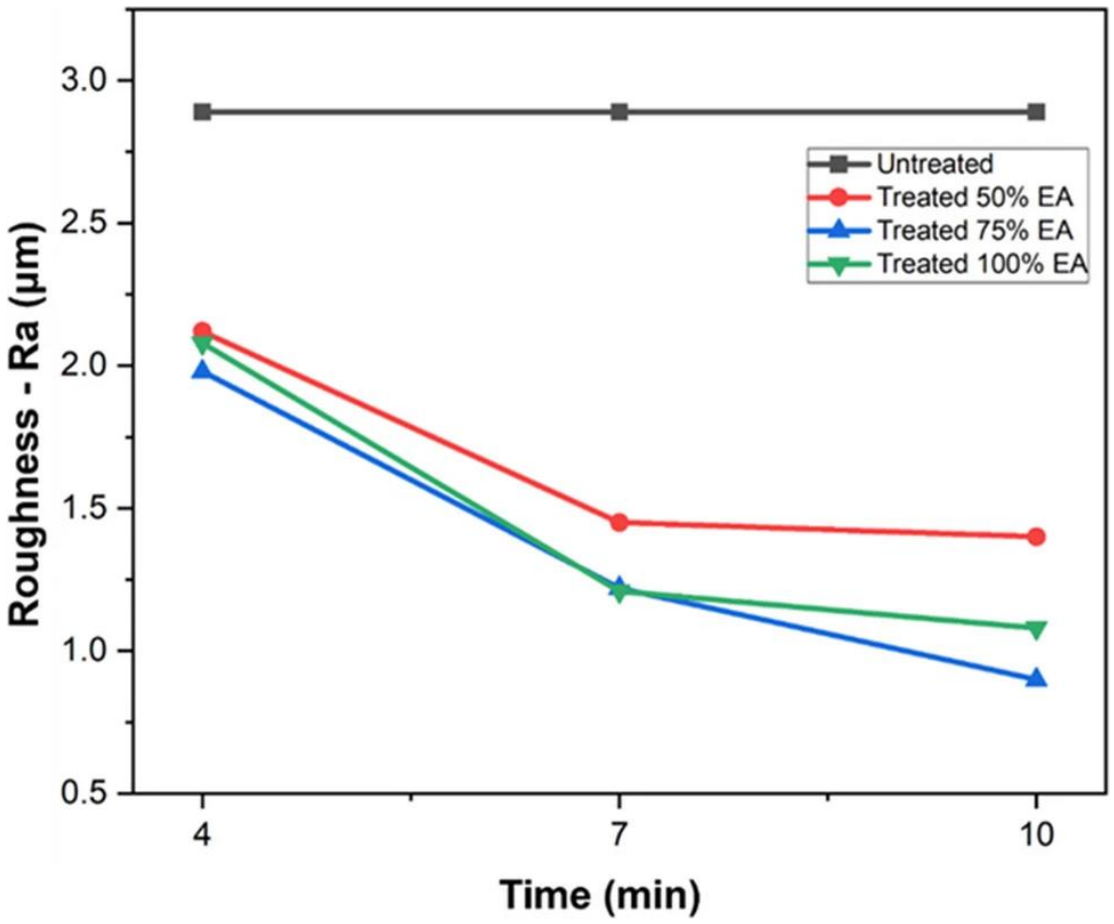

Figure 4.1. Average surface roughness (Ra) of solvent-treated ABS samples at different EA concentrations and treatment times. The 7 min – 75 % EA condition achieved near-optimal smoothing. From our published work, Iqbal et al. 2024 (Iqbal et al., 2024).

Table 4.1. Measured Ra values for all solvent-treatment conditions (nine parameter combinations, 27 specimens total) From our published work, Iqbal et al 2024 (Iqbal et al., 2024)

Application Time (min)	EA Concentration (Vol%)	Ra (µm)	Rz (µm)	Rq (µm)	Observation
4	50	2.1 ± 0.2	12.1 ± 3.0	2.7 ± 0.4	Minor smoothing observed; incomplete layer relaxation.
4	75	2.0 ± 0.34	9.9 ± 2.8	2.4 ± 0.4	Slightly improved uniformity over 50 %.
4	100	2.1 ± 0.01	11.1 ± 1.1	2.6 ± 0.07	No further improvement; likely surface oversaturation.

7	50	1.4 ± 0.2	6.5 ± 2.0	1.7 ± 0.4	Significant roughness reduction (~35 % vs 4 min).
7	75	1.2 ± 0.1	5.5 ± 0.7	1.4 ± 0.1	Optimal smoothing; uniform surface finish.
7	100	1.2 ± 0.3	5.6 ± 1.2	1.5 ± 0.3	Comparable to 75 %; diffusion saturation reached.
10	50	1.4 ± 0.5	6.6 ± 3.0	1.7 ± 0.7	Minimal improvement beyond 7 min.
10	75	**0.9 ± 0.15**	**3.8 ± 0.7**	**1.1 ± 0.2**	**Best overall roughness reduction (Ra ≈ 0.9 µm).**
10	100	1.1 ± 0.02	5.5 ± 1.0	1.4 ± 0.2	Marginal benefit; risk of local surface irregularities.

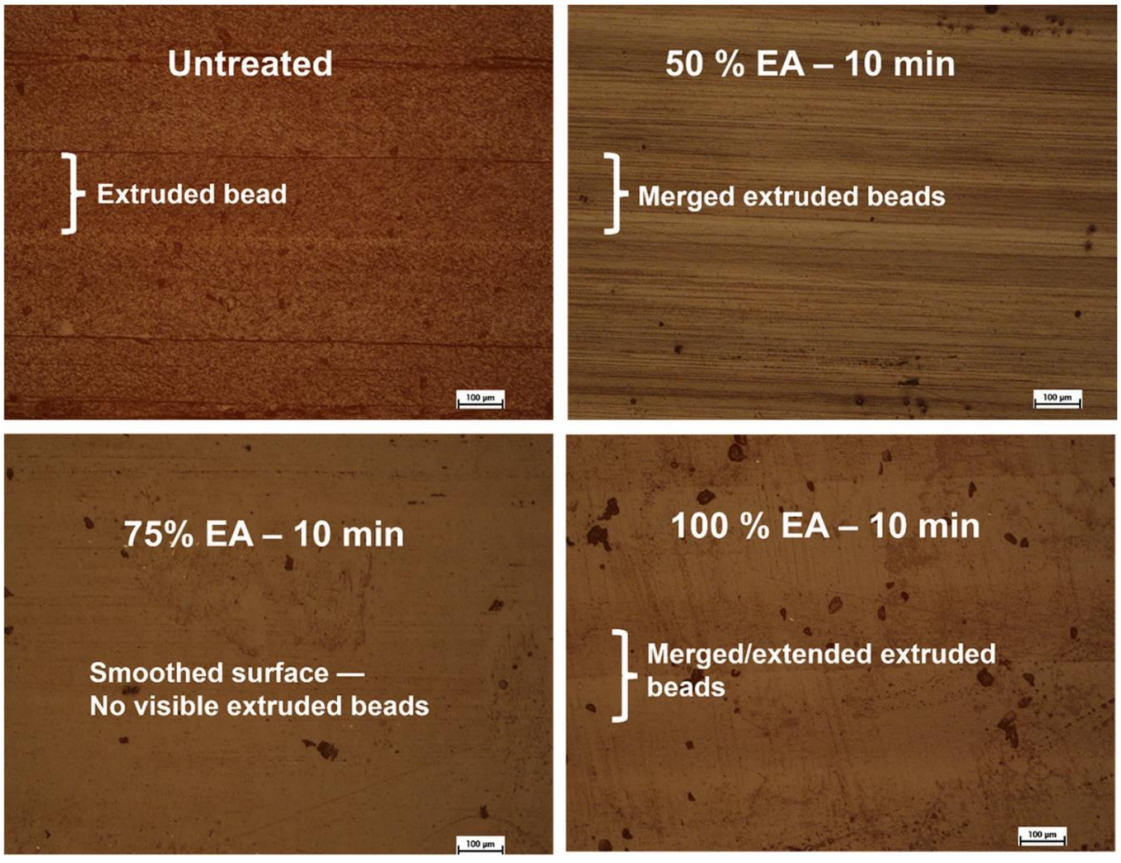

Figure 4.2. Optical microscope images of untreated and EA-treated ABS surfaces. Smoother topography is evident at 75 % EA, 7–10 min, whereas 100 % EA causes localized over-swelling. From our published work, Iqbal et al 2024 (Iqbal et al., 2024).

From these experiments, two viable process windows were established:

- **Optimal smoothing condition:** 75 % EA, 10 min (Ra ≈ 0.9 µm)
- **Economical condition:** 50 % EA, 7 min (Ra ≈ 1.4 µm)

These sets were then used for multilayer void-reduction analysis

4.2. Void-Reduction and Interlayer Densification

Building upon the preliminary surface roughness analysis, multilayer ABS specimens comprising ten printed layers were fabricated to further evaluate the influence of solvent exposure parameters on surface morphology and interlayer fusion. Four distinct post-treatment conditions were selected to capture the combined effects of solvent concentration and exposure duration: 50% EA for 7 minutes, 50% EA for 10 minutes, 75% EA for 7 minutes, and 75% EA for 10 minutes. These conditions were chosen to represent a controlled gradient of solvent activity, enabling systematic observation of polymer relaxation, surface smoothing, and potential over-swelling phenomena across varying treatment intensities.

The solvent treatment was applied after every deposited layer (nine total exposures). Figure 4.3 presents the optical micrographs of cross-sections for all configurations compared with untreated controls. The difference in void density is striking while conventional samples show numerous large voids between filaments, the treated specimens exhibit a much denser microstructure and smoother interfaces.

Quantitative image analysis was performed on 2×1.2 mm^2 regions per cross-section, evaluating void density, area, and perimeter (Table 4.2). The untreated control contained ≈30 voids per area, occupying ~ 2.4 % of total volume. The 50 % EA – 7 min treatment lowered void fraction to 1.9 % (≈ 21 % reduction). More intensive conditions further improved bonding: both 50 % EA – 10 min and 75 % EA – 7 min reduced average void area by ≈50 %, confirming that longer exposure or higher concentration promotes polymer reflow and fusion at interlayer boundaries.

The best overall densification occurred at 75 % EA – 10 min, yielding a residual void fraction of only 0.08 %, i.e., a 96.8 % reduction in void density and 79 % reduction in mean void area relative to untreated samples. Figure 4.3e clearly shows nearly complete elimination of interlayer gaps.

Figure 4.3. Optical micrographs of cross-sections: (a) untreated, (b) 50 % EA – 7 min, (c) 50 % EA – 10 min, (d) 75 % EA – 7 min, (e) 75 % EA – 10 min. Progressive reduction in interlayer voids with increasing treatment intensity is evident (Iqbal et al., 2024).

Table 4.2. Quantitative void-analysis data: density, area, and perimeter for traditional and solvent-treated samples.

Sample ID / Treatment Condition	Void Average Area (× 10^{-4} mm²)	Void Average Perimeter (× 10^{-2} mm)	Estimated Void Volume Density (%)	Observation
a) Untreated		20.0 ± 1.4	2.4	Baseline case with high void density and irregular interfaces.
b) 50 % EA – 7 min	15 ± 3	17.3 ± 2.0	1.9	Moderate reduction in void area; partial interface smoothing.
c) 50 % EA – 10 min	10 ± 2	13.8 ± 1.5	1.3	Improved densification; voids reduced by ≈ 45 % vs. untreated.
d) 75 % EA – 7 min	9 ± 2	13.1 ± 1.7	1.1	Significant reduction; strong interlayer bonding observed.
e) 75 % EA – 10 min	4 ± 1	8.7 ± 1.2	0.08	Optimal condition; nearly void-free structure (≈ 97 % reduction).

4.3. Mechanistic Interpretation: Interlayer Bond Width and Wetting Factor

To elucidate the physical mechanism behind void reduction, the bond width ($w_{(bond)}$) between successive extruded filaments was compared with the nominal bead width ($w_{(bead)}$) = 0.45 mm (set in slicing software). Solvent vapor partially dissolves the top of layer n, enabling molecular diffusion and increasing the actual contact area for layer n + 1. As shown in Figure 4.4, the treated samples exhibit visibly thicker interlayer regions.

The degree of adhesion can be expressed through the wetting factor ($f_{(w)} = W(bond)/W(bead)$. For untreated samples, $f_{(w)} \approx 0.66$ ($w_{(bond)} = 0.30$ mm), while for treated samples (75 % EA – 7 min), $f_{(w)} \approx 0.91$ ($w_{(bond)} = 0.41$ mm), signifying a 27.5 % improvement.

Under optimal conditions (75 % EA – 10 min), the factor approached unity, indicating complete interlayer wetting and fusion.

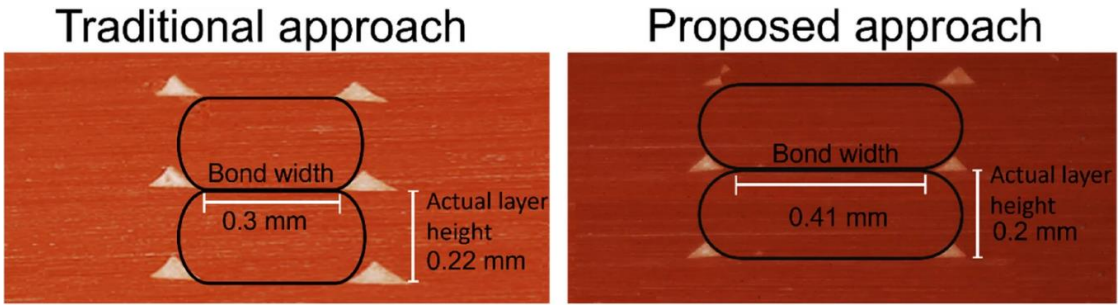

Figure 4.4. Cross-sectional comparison between untreated and solvent-treated samples showing wider bonded regions and reduced voids in the treated case. Enhanced polymer diffusion results in improved cohesion (Iqbal et al., 2024).

The wetting factor trend explains the direct relationship between treatment conditions and mechanical integrity: as $f(w) \rightarrow 1$, interlayer adhesion increases and voids disappear. This relationship aligns with Coogan et al. (Coogan & Kazmer, 2017), who correlated bonding strength with bead-bond geometrical overlap.

4.4. Consolidated Findings

The main outcomes of this phase are summarized in Table 4.3 and Figure 4.5. The proposed EA vapor in-situ treatment improved all key metrics compared to traditional material extrusion, achieving:

- Void density reduction: ≈ 97 %
- Void area reduction: ≈ 79 %
- Surface roughness reduction: ≈ 60 %
- Wetting factor increase: ≈ 34 %

Table 4.3. Summary of the main improvements obtained with solvent-assisted interlayer treatment compared with conventional printing.

Parameter	Traditional Approach	Proposed Solvent-	Improvement (%)	Remarks / Interpretation

		Assisted Approach		
Void density (% volume)	2.4	0.08	96.7	Nearly void-free microstructure achieved; enhanced interlayer bonding.
Average void area (mm²)	19×10^{-4}	4×10^{-4}	79.	Significant densification and uniform polymer reflow.
Average void perimeter (mm)	20×10^{-2}	8.7×10^{-2}	56.5	Reduction in interfacial discontinuities between extruded layers.
Wetting factor (*f*w)	0.66	≈ 1.00	34	Indicates complete interlayer wetting and adhesion.
Manufacturing time per layer (min)	2	15 (2 + 13 treatment)	—	Manual process; automation can offset time increase.

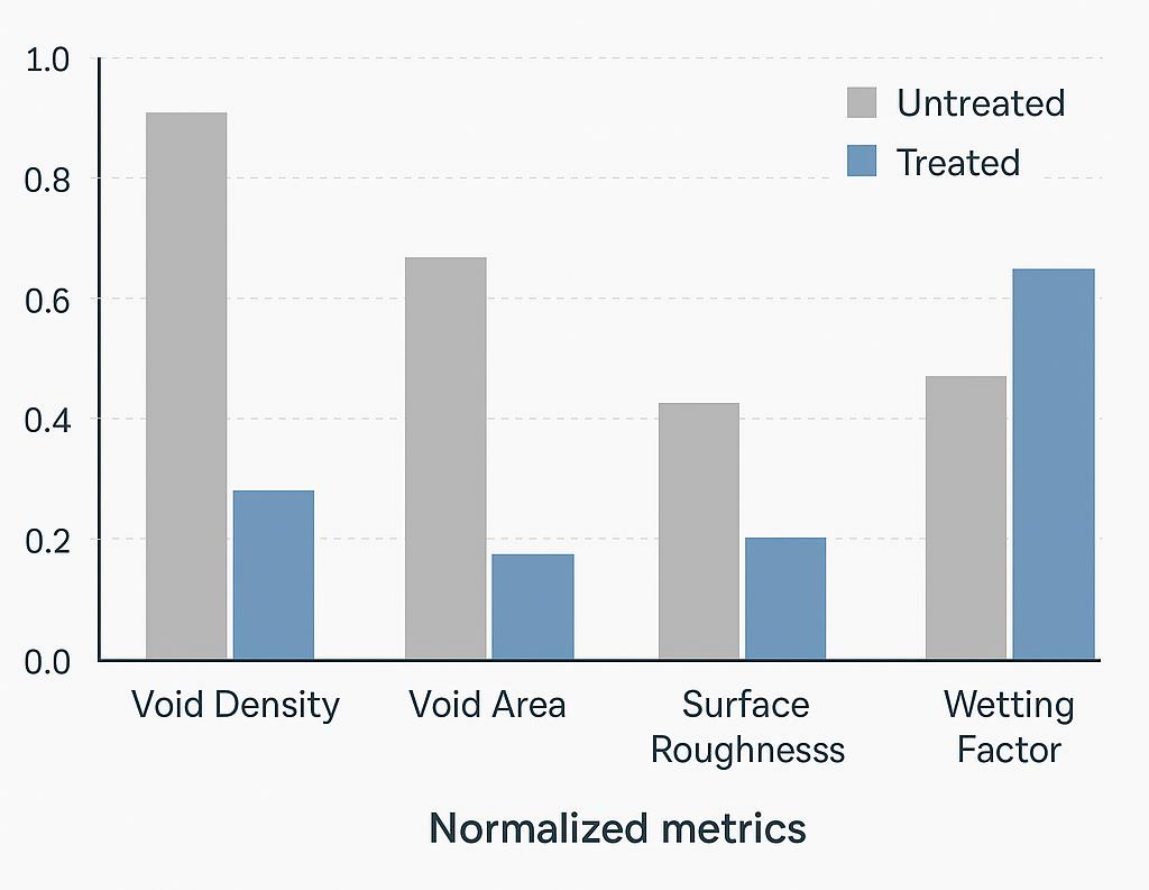

Figure 4.5. Graphical summary of process improvements achieved with the proposed EA-assisted layer-by-layer treatment. Each metric is normalized to the untreated baseline.

While the current implementation required manual intervention and added approximately 13 min per layer (cooling + treatment + restart), the methodology's simplicity and reproducibility make it ideal for automation. Future work will integrate synchronize solvent application with layer deposition, eliminating pauses and human handling.

4.5. Relevance to Subsequent Research

The solvent-assisted post-treatment study presented in this chapter constitutes a critical methodological and conceptual foundation for the subsequent research developed in this thesis. Beyond serving as an isolated process optimization, this investigation establishes a transferable framework for interfacial engineering in material-extrusion additive

manufacturing, which is directly leveraged in the fabrication of functional 3D-printed battery electrodes.

Through a systematic analysis of solvent diffusion, polymer chain mobility, and interlayer void suppression, this study provides fundamental insight into how post-printing physicochemical interactions can be used to control density, cohesion, and microstructural continuity in printed architectures. These principles are not limited to polymer–polymer interfaces; rather, they are highly relevant to composite systems in which electrically active phases are embedded within a polymeric matrix. In the context of energy-storage materials, such interfacial control is essential for achieving both mechanical integrity and efficient charge-transport pathways.

Importantly, the ability to manipulate porosity, interlayer bonding, and surface morphology through solvent-mediated mechanisms directly informs the later development of dense yet permeable LTO/carbon composite filaments, where electrolyte accessibility and electronic percolation must be carefully balanced. The understanding gained here enables a rational transition from purely structural optimization toward functional electrode design, ensuring that improvements in print quality translate into meaningful electrochemical performance enhancements rather than purely aesthetic or mechanical gains.

In the subsequent sections of the thesis, these solvent-induced interfacial engineering concepts are extended from polymer-only systems to polymer–ceramic–carbon electrode architectures, effectively bridging additive manufacturing science with electrochemical materials engineering. This continuity ensures that the later chapters build upon a rigorously established process foundation, reinforcing the coherence of the thesis and highlighting the solvent-treatment study as an enabling step in the realization of fully 3D-printed, electrochemically active energy-storage devices.

4.6. FTIR Analysis

The FTIR spectrum of the as-synthesized borophene exhibits four diagnostic bands that collectively confirm formation of a two-dimensional boron network with light hydrogenation and mild surface oxidation as shown in Figure 4.6. A sharp feature at ~889 cm is assigned to the B–H stretching mode, indicating hydrogen termination of boron edges/defect sites formed

during exfoliation. The strongest skeletal vibration appears at $\sim$1044 cm^{-1}, attributable to B–B framework stretching; its position near 1.04–1.06 × 10^3 cm^{-1} and its increased intensity relative to the sub-1000 cm^{-1} region are consistent with an extended sp-like B–B lattice rather than bulk amorphous boron. Two broader bands at $\sim$1222 cm^{-1} and $\sim$1372 cm^{-1} arise from B–O stretching of surface boron–oxide (and/or B–O–B) moieties formed upon brief air exposure; the presence of these peaks with moderate intensity is typical for few-layer borophene stabilized by a thin passivation layer. Relative to reference positions reported for elemental boron (B–B ≈1055 cm^{-1}; B–H ≈890 cm^{-1}; B–O ≈1215 and 1365–1380 cm^{-1}), the spectrum shows a slight red-shift of the B–B band (→ 1044 cm^{-1}) and a narrowing of its full width, both consistent with increased in-plane order and reduced three-dimensional connectivity expected after delamination into 2D sheets. The near-unchanged B–H position ($\sim$889 cm^{-1}) indicates that hydrogen termination persists post-synthesis and can later be tuned (e.g. mild vacuum anneal) to balance dispersion in polar matrices with conductivity. Overall, the coexistence of a strong B–B skeletal mode, a discrete B–H stretch, and moderate B–O stretches constitute a robust FTIR fingerprint of few-layer borophene with edge hydrogenation and thin oxidative passivation. For subsequent LTO-composite anode fabrication, the surface B–O/B–OH groups are advantageous for interfacial coupling to oxide particles, while the intact B–B network underpins the additive's electronic contribution.

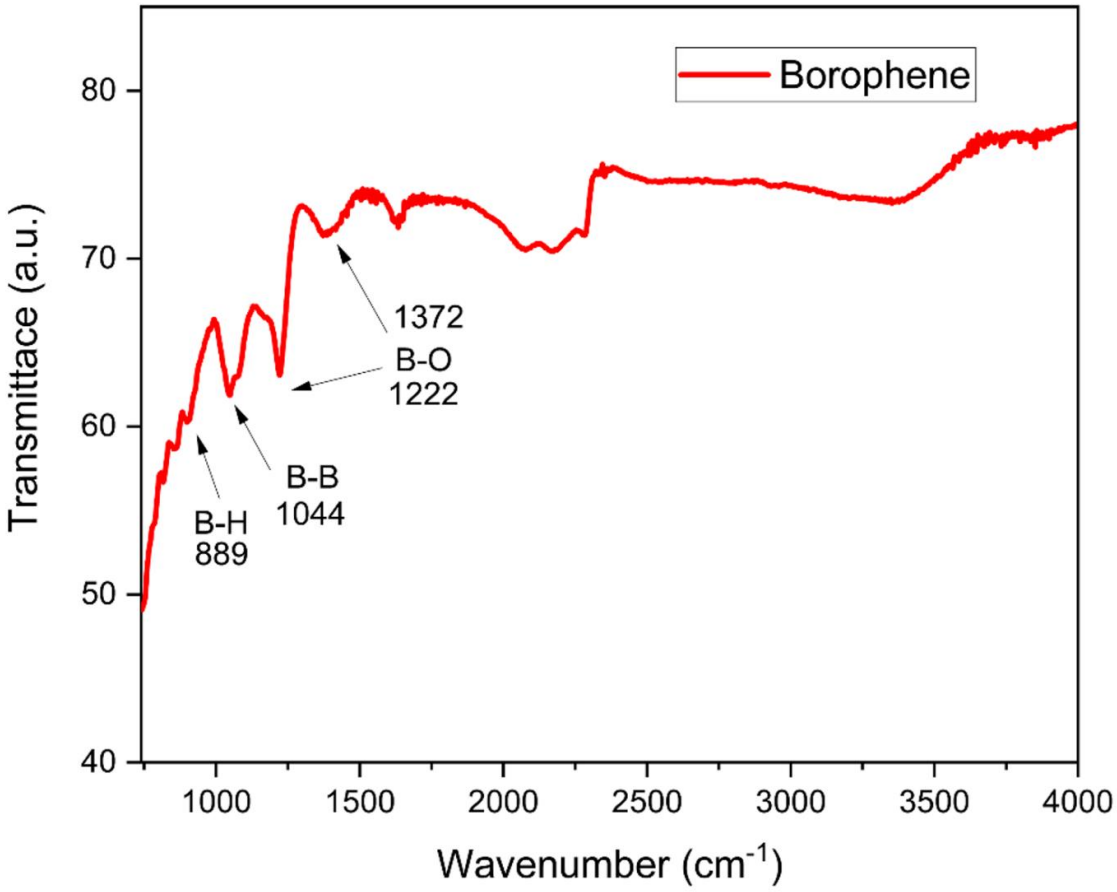

Figure 4.6. FTIR spectrum of the synthesized borophene showing characteristic B–H, B–B, and B–O vibrational modes confirming the formation of few-layer borophene.

4.7. SEM analysis

The corresponding SEM micrographs show clear morphological transformation from the boron precursor to the exfoliated borophene product.

In Figure 4.7A, the raw boron powder exhibits a dense, granular microstructure composed of irregular agglomerates with particle sizes ranging from 5 to 20 μm. The surfaces appear relatively smooth and featureless, indicating compact, bulk-like particles with limited surface area and minimal nanoscale features. This morphology is typical of commercial amorphous or β-rhombohedral boron powders. In contrast, Figure 4.7B presents the microstructure of the synthesized borophene, which reveals a pronounced morphological refinement. The material

exhibits a flake-like, loosely packed texture with interconnected nanosheets and porous agglomerates. The presence of thin, wrinkled sheets and a networked appearance confirms successful exfoliation and formation of 2D borophene layers. The average flake thickness is in the submicron range, and the lateral dimensions appear extended, giving rise to a high aspect ratio conducive to both electronic conduction and surface reactivity.

The porous, entangled morphology in the borophene sample also implies partial layer restacking a common feature in solution-derived or thermally reduced 2D materials but the retained open structure facilitates electrolyte infiltration and uniform dispersion within composite matrices. The observed contrast variation in SEM (bright vs. dark regions) indicates slight differences in thickness and local oxidation, which correlates well with the moderate B–O peaks detected in FTIR.

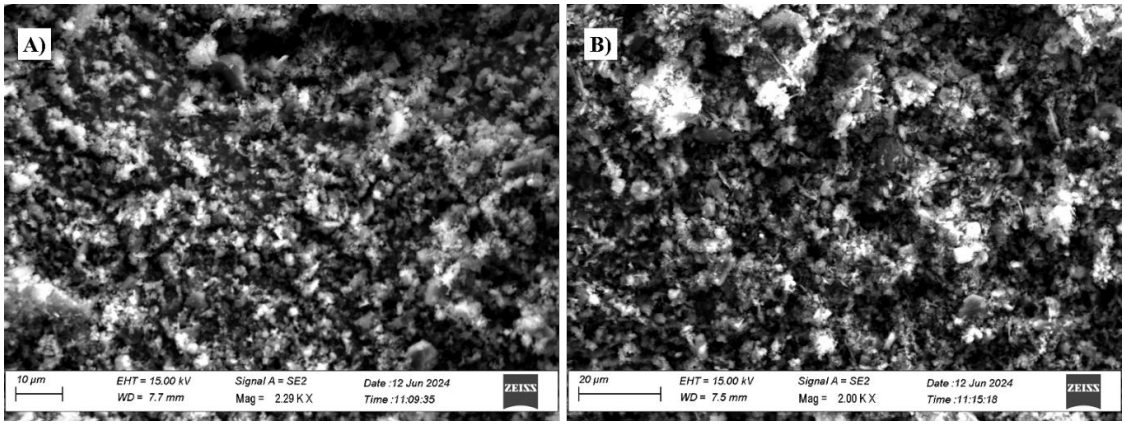

Figure 4.7. SEM micrograph of A) boron and B) synthesized borophene showing exfoliated flake-like nanosheet morphology with high surface roughness and porosity.

4.8. Thermal behavior (DSC–TGA analysis)

The TGA curve (Figure 4.8) of the composite reveals that the composite exhibits multistage degradation behavior. The first minor mass loss (< 2 wt %) below 100 °C corresponds to the removal of adsorbed moisture and residual solvent (DCM) from the polymer matrix. The sample retains over 97 wt % stability up to ~300 °C, confirming that the borophene and LTO fillers do not catalyze premature thermal decomposition of PLA. Beyond ~320 °C, the main degradation step commences, corresponding to thermal decomposition of the PLA backbone

through random chain scission and depolymerization. The maximum weight-loss rate is observed around 360–370 °C, indicating the primary decomposition region of the polymer fraction.

Incorporation of LTO and borophene shifts this onset temperature slightly upward compared with neat PLA (typically ~320–340 °C onset), suggesting a stabilizing influence of the inorganic fillers. The high thermal conductivity and heat-dissipating ability of borophene, combined with the refractory ceramic nature of LTO, effectively delay thermal breakdown by reducing local hot-spot formation within the matrix. The decomposition proceeds gradually until ~ 450 °C, after which a relatively stable residue remains. The total mass loss measured is ≈ 35.9 wt % (4.30 mg), implying that approximately 64 wt % of the composite remains as inorganic residue, which agrees closely with the intended solid-phase loading of LTO + borophene (~ 60–65 wt %) used in formulation.

The DSC trace further corroborates this thermal behavior. A broad endothermic signal below 100 °C reflects moisture and residual solvent evaporation. The first small endotherm at ~ 60 °C corresponds to the glass transition (Tg) of PLA, indicating retained amorphous chain mobility after composite formation. The subsequent major endothermic peak at ~168–172 °C is attributed to the melting (Tm) of semicrystalline PLA. The narrowness of this peak implies that the polymer chains retained partial crystallinity, while the slight shift to lower temperature relative to pristine PLA (Tm ≈ 175 °C) denotes restricted crystal growth due to the finely dispersed fillers acting as physical barriers.

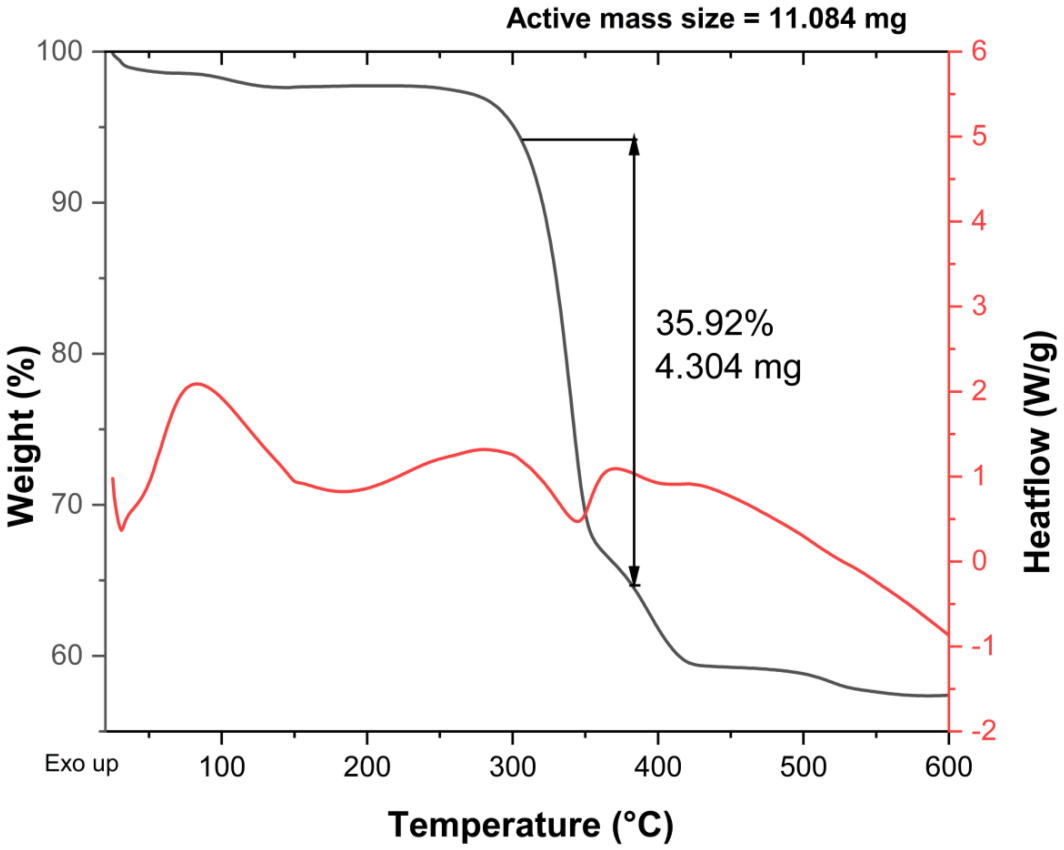

Figure 4.8. Simultaneous TGA–DSC analysis of the LTO–borophene–PLA composite under nitrogen atmosphere. (DSC thermogram of the LTO–borophene–PMMA–PLA composite showing the glass transition (~60 °C) and melting endotherm (~170 °C). The slight reduction in ΔH_f compared to pure PLA indicates filler-induced crystallinity suppression favorable for interlayer adhesion during 3D printing.

TGA curve of the composite under N_2 atmosphere. Minor volatilization below 100 °C corresponds to residual solvent/moisture; main polymer degradation occurs above 320 °C, leaving ~ 40 wt % inorganic residue consistent with the LTO + borophene content.

Beyond ~300 °C, a series of overlapping exothermic and endothermic features appear in the DSC curve, corresponding to polymer decomposition and char formation. The exothermic signal at ~360–370 °C coincides with the maximum mass-loss rate seen in the TGA curve, confirming that this transition arises from oxidative chain scission and volatile evolution of the PLA–PMMA blend. A second sharp endothermic peak around 620 °C indicates the recrystallization or phase transformation of the inorganic component, likely due to the

structural rearrangement of LTO and partial oxidation of residual boron species into B_2O_3. Such a high-temperature event demonstrates that the inorganic scaffold remains thermally stable well beyond the polymer decomposition range.

Overall, the DSC–TGA data verify that the composite is thermally processable up to ~ 200 °C, ensuring a safe operating window for FDM/FFF printing and subsequent device integration. The retained inorganic residue of ~ 64 wt % indicates the formation of a continuous LTO–borophene network capable of preserving the electrode architecture after polymer burnout if needed for post-processing or sintering. The slight delay in the onset of degradation, combined with the maintenance of the PLA melting transition, supports the conclusion that borophene acts as both a thermo-stabilizer and conductive enhancer, while LTO contributes structural rigidity and oxidation resistance.

These results confirm that the PLA + Borophene + LTO composite possesses adequate thermal stability for extrusion-based additive manufacturing, with a melt-processing window (160–180 °C) and decomposition onset above 320 °C. The data thus provide a reliable basis for selecting printing parameters and validating material integrity prior to electrochemical testing.

4.9. Conductivity Evaluation of Conductive Additives

4.9.1. Conductivity evolution and percolation behavior

Each additive was mixed with 25–30 wt% PLA using DCM as the only solvent, followed by oven drying and compaction into dense pellets under 2.5–3.5 tons of uniaxial pressure. The additive content was systematically varied from 1–9 vol%, allowing a clear observation of percolation thresholds and maximum conductivity regions.

As shown in Figure 4.9, the overall trend reveals a strong dependence of electrical conductivity (σ) on the additive type and its volumetric loading. Across all materials, conductivity increases sharply with additive content and tends to plateau beyond approximately 8 vol%, signifying the onset of a continuous electron conduction network. This percolation-driven transition indicates that above a critical filler fraction, adjacent conductive domains overlap sufficiently to permit uninterrupted charge transport through the matrix.

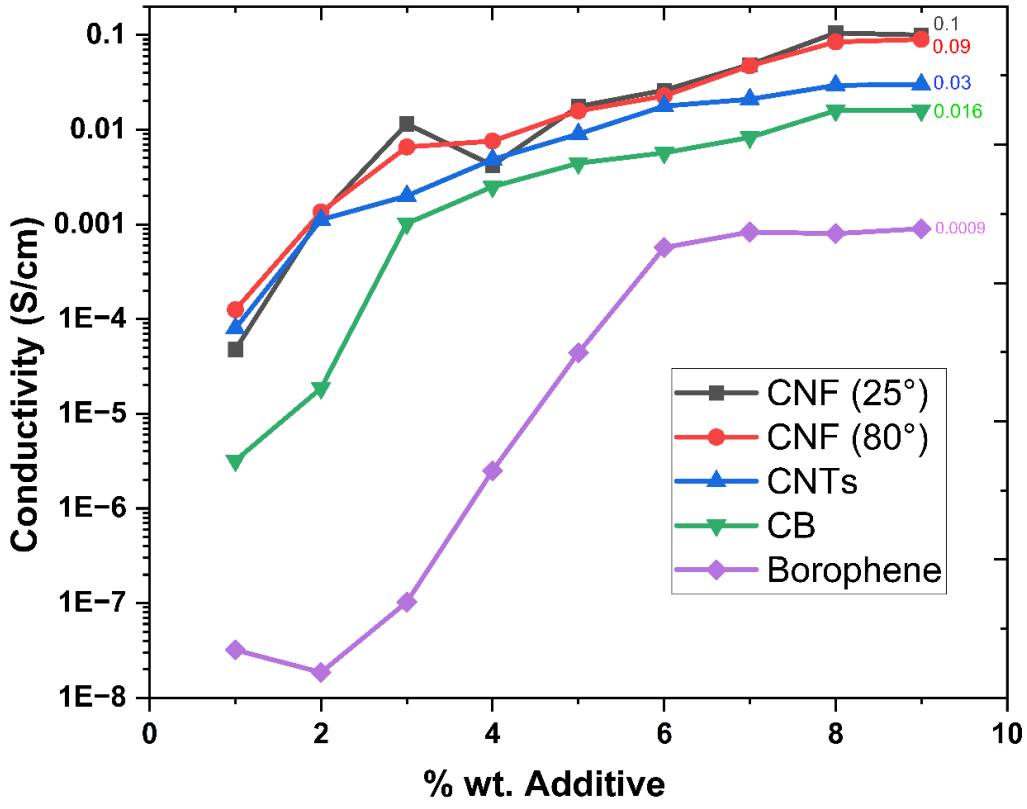

Figure 4.9. Comparative electrical conductivity of different additives (CNF, CNT, CB, borophene) showing that CNTs and CNFs exhibit higher intrinsic conductivity, while borophene demonstrates consistent conductivity improvement with loading due to flake interconnection.

Figure 4.9 presents the electrical conductivity of compacted pellets containing different conductive additives as a function of additive weight fraction. The conductivity data are plotted on a logarithmic scale (log_{10}) to capture the wide dynamic range characteristic of polymer-based composite systems, where electrical transport typically spans several orders of magnitude as the filler content approaches and surpasses the percolation threshold.

Among the additives investigated, CNF and CNT-based systems exhibit the highest electrical conductivities across the entire concentration range. At loadings of 8–10 wt%, CNFs reach conductivities on the order of $\sigma \approx 0.1$ S·cm^{-1}, with comparable values observed for CNFs measured at elevated temperature (80 °C). CNT-containing pellets achieve slightly lower, yet still substantial, conductivities of approximately $\sigma \approx 0.03$ S·cm^{-1}. These materials display a

pronounced percolation transition at relatively low filler contents (~2–3 wt%), which is attributed to their one-dimensional graphitic morphology and high aspect ratio. Extended π-electron delocalization along the fiber axis facilitates efficient charge transport, while the elongated geometry promotes rapid formation of interconnected conductive networks, enabling electron tunneling and long-range transport at minimal additive concentrations.

CB exhibits intermediate electrical performance, reaching $\sigma \approx 0.016\ S \cdot cm^{-1}$ at higher loadings. Owing to its quasi-spherical particulate morphology, CB requires higher concentrations to establish continuous conductive pathways. Electrical transport in these systems is dominated by interparticle contact resistance and tunneling across particle–particle junctions, resulting in a more gradual conductivity increase and lower overall performance compared to high-aspect-ratio carbon nanostructures.

Borophene pellets display the lowest absolute conductivity among the tested additives, reaching $\sigma \approx 9 \times 10^{-4}\ S \cdot cm^{-1}$ at high loadings. However, unlike CB, borophene shows a steady and monotonic increase in conductivity with increasing additive content, without an abrupt percolation jump. This gradual evolution is characteristic of two-dimensional conductive materials, where electrical transport is governed by flake–flake contact density, platelet alignment, and interfacial junction resistance rather than long, continuous conductive pathways. As the borophene loading increases, enhanced overlap and partial alignment of nanosheets under compaction progressively reduce interfacial resistance, facilitating lateral electron tunneling and improved charge transport.

The comparatively lower conductivity of borophene pellets relative to CNTs and CNFs can be partially attributed to mild surface oxidation, as evidenced by B–O vibrational bands in the FTIR spectra (1220–1370 cm^{-1}, Figure 4.6). These oxidized surface species introduce electron scattering sites that limit intrinsic conductivity. Nevertheless, borophene's atomically thin, two-dimensional structure and high surface energy impart strong interfacial activity, enabling intimate contact with polymer chains and oxide particles. Rather than acting as a standalone conductor, borophene is therefore best understood as a complementary and reactive conductive additive that enhances interfacial charge transfer and stabilizes conductive networks in hybrid composite systems.

4.9.2 Percolation threshold and temperature effect

The conductivity data at 25 °C and 80 °C for CNFs further confirm that the electronic conduction is predominantly electron tunneling dominated, with minimal thermal activation dependence. The minor drop at elevated temperature (from 0.1 to 0.09 $S.cm^{-1}$) can be attributed to slight structural relaxation of the polymer matrix and possible microcrack formation under thermal expansion.

In contrast, borophene's σ increases monotonically without temperature sensitivity, consistent with stable covalent bonding and the absence of volatile functional groups that might disrupt charge continuity.

The overall percolation sequence observed was:

$$\boldsymbol{\sigma_{CNF(25°C)} \approx \sigma_{CNF(80°C)} > \sigma_{CNT} > \sigma_{CB} > \sigma_{Borophene}}$$

This ranking aligns well with theoretical predictions and literature-reported conductivities for similar systems (Zare, Naqvi, Rhee, & Park, 2025).

4.9.3. Implications for composite electrode design

These findings played a decisive role in determining the conductive network for subsequent composite development and 3D printing. The CNF additive was selected as the primary conductive backbone, offering high intrinsic σ and network integrity, while borophene was incorporated as a secondary, interfacial enhancer to reinforce charge pathways across the LTO–polymer composites interfaces. This dual strategy effectively combines macroscale conductivity (CNF) and nanoscale interfacial coupling (borophene), a balance essential for achieving uniform charge distribution and structural cohesion in printed electrodes.

Therefore, this pre-screening step not only benchmarked the additive performance but also provided a quantitative framework for optimizing composite formulations. The borophene data, in particular, validated its functional potential in composite form, even if its bulk conductivity was comparatively modest.

The percolation threshold mentioned in the Table 4.4 is the critical filler concentration above which a continuous conductive network forms, was observed to vary significantly among the tested additives. CNFs and CNTs achieved percolation at ~2–3 vol%, attributed to their elongated one-dimensional geometry enabling efficient interconnection at low volume fractions. In contrast, borophene and carbon black required higher loadings (6–7 vol% and 4–5 vol%, respectively) to achieve similar conductivity levels, owing to their 2D plate-like and 0D particulate morphologies. This analysis highlights the crucial role of filler shape and dispersion state in determining electronic transport within the polymer matrix.

Table 4.4. Comparative electrical performance and percolation characteristics of conductive additives incorporation

Additive	**Structure Type**	**σ at 8 vol% (S.cm^{-1})**	**Percolation Threshold**	**Dominant Conduction Path**	**Key Remarks**
CNF (25°C)	1D graphitic fiber	0.10	2–3%	Longitudinal ballistic conduction	Highest overall σ; stable at RT
CNF (80°C)	1D graphitic fiber	0.09	2–3%	Same as above	Minimal thermal dependence
CNT	1D tubular	0.03	3–4%	Networked tunneling	Good percolation, moderate σ
CB	0D particulate	0.016	4–5%	Point-to-point hopping	Uniform, isotropic conduction
Borophene	2D lamellar	9×10^{-4}	6–7%	Planar overlap tunneling	Strong interfacial coupling potential

4.10. Extrusion-feasibility assessment of PLA/LTO composites with conductive additives

4.10.1. MFI and extrusion response

Preliminary extrusion trials were carried out to determine whether PLA/LTO composites loaded with conductive additives (borophene, CNF, CNT, CB; 1–9 wt% additive; PLA 25–30 wt% of the total) could be transformed into continuous filaments suitable for material-extrusion printing. Melt-flow index (MFI) tests at 180 °C under standard loads (2.16, 3.8 and 5 kg) were used as a rapid rheology proxy to rank formulations before filamenting.

Three consistent trends emerged:

1. **Flow window and shear sensitivity.**
   At 2.16–3.8 kg, CNF- and CNT-filled blends exhibited steady mass-throughput and reproducible MFR values, indicating a shear-thinning melt that could be driven through a 1.75 mm die without surging. CB blends flowed more slowly (higher apparent viscosity) but remained stable. In contrast, borophene blends showed load-sensitive flow oscillations; at 5 kg they displayed intermittent surges consistent with incipient melt fracture.
2. **Effect of conductive-network density.**
   Around 8 wt% additive the level previously identified as the electronic-percolation sweet spot in pellet tests CNF and CNT systems maintained manageable viscosities, whereas borophene at the same total solids led to a marked increase in torque and pressure drop. The interpretation is that rigid platelet networks in the boron phase stiffen the matrix more strongly than the slender 1D networks formed by CNF/CNT at equivalent volume fractions.
3. **Die swell and thermal stability.**
   At 5 kg load, all systems showed some die swell; only borophene blends coupled swell with localized overheating (brown/black bands) near the die exit—an indicator that the melt relaxation time exceeded the residence time at the imposed shear rate.

Taken together, the MFI screen suggested that CNF ≈ CNT > CB ≫ borophene in terms of extrusion robustness, even before considering surface quality and mechanical integrity of filaments.

4.10.2. Morphology of extruded filaments and failure modes

Representative extrudates obtained from the MFI-guided processing window are shown in Figure 4.10. That shows a macroscopic view of a free-standing filament, demonstrating that continuous strands with lengths on the order of ~13-20 cm (an example of 13 cm length of filament shown in Figure 4.10A can be produced under optimized extrusion conditions. However, higher-magnification insets reveal pronounced surface irregularities, including longitudinal crack trains and inter-bead discontinuities along the filament length.

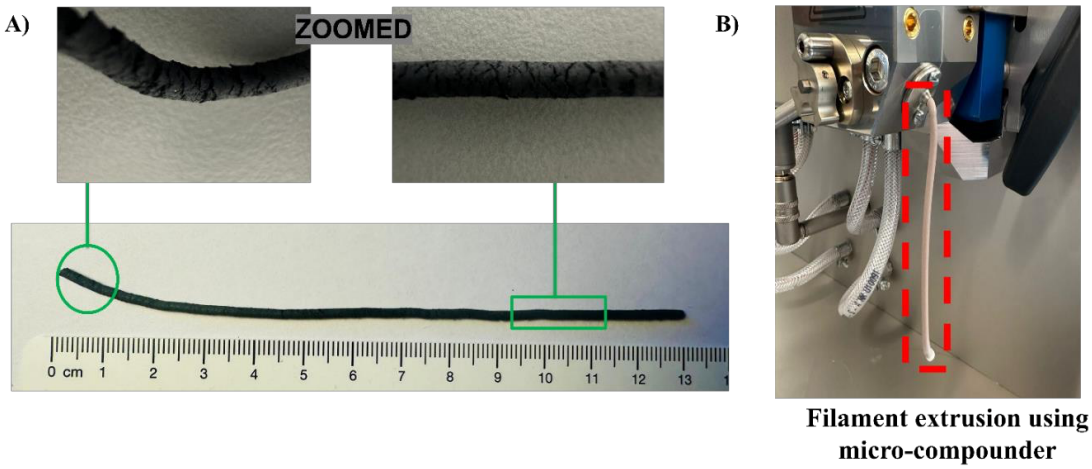

Figure 4.10. (A) Macroscopic image of a representative free-standing filament extruded from the PLA–borophene–LTO composite, showing continuous geometry over a length of approximately 13 cm, as measured against the ruler. Highlighted regions indicate locations of magnified views, revealing local surface texture and curvature along the filament length. (B) Filament extrusion from the micro-compounder nozzle, illustrating the vertical extrusion configuration and the formation of a continuous, self-supporting filament immediately upon exit from the die.

Key observations

- **Periodic surface fissures (“sharkskin” analogue).**

The crack spacing and alignment with the flow direction are characteristic of extensional-strain instabilities at the die exit. In filled thermoplastics, this occurs when elastic recovery (Weissenberg number Wi ≫ 1) overcomes the matrix's ability to relax; the skin tears as it accelerates from no-slip to free-surface flow. The effect was most pronounced in borophene-containing variants, moderate in CB, and significantly lower in CNF/CNT composites.

- **Sub-surface porosity/voids.**

  Transverse cuts (not shown) and the dark "pitted" regions in the micrographs indicate entrapped porosity. Mechanistically, this is attributed to (i) incomplete wetting of high-surface-area fillers by PLA during compounding, (ii) micro-debonding at LTO–polymer interfaces under extensional stress, and (iii) rapid pressure drop at exit causing dissolved volatiles to nucleate. Porosity was again highest for borophene systems, consistent with poorer interfacial compatibility and higher elastic modulus of the network.

- **Brittleness and handling fractures.**

  Filaments with excellent room-temperature conductivity (near the 8 wt% additive level) nevertheless snapped during winding and showed low bendability. This points to an unfavorable electromechanical trade-off: once the conductive phase percolates, it also constrains chain mobility, reducing ductility and necking capacity essential for spooling and later printing.

The distinct light brown coloration observed in the extruded filament during processing Figure 4.10B arises from the incorporation of borophene within the polymer matrix. Unlike carbon-based additives, which typically impart a uniform black appearance, borophene produces a characteristic brown-to-dark bronze tone due to its two-dimensional metallic sheet structure and light absorption behavior. The homogeneous color along the extruded strand indicates effective dispersion of borophene during compounding and extrusion, rather than localized agglomeration or surface contamination. Importantly, no evidence of thermal degradation or burning was observed at the die exit, confirming that the color change is intrinsic to the

borophene-filled composite rather than a processing artifact.

Even when MFI suggests a viable flow rate, surface integrity and post-exit relaxation become the decisive criteria for printability. Without further rheology tuning, crack initiation sites will propagate during deposition, producing inter-road voids and poor interlayer bonding in printed electrodes.

4.10.3. Linking rheology, microstructure and function

The combined MFI–morphology dataset clarifies why CNF emerged as the most promising additive for the next stage:

- **Network geometry:** 1D fibers establish long-range electron pathways at moderate loading while imposing less viscous and elastic penalty than platelet-rich networks.
- **Dispersion & alignment:** With standard sonication/shear, CNFs disperse with fewer mesoscale aggregates than CNTs, and they can partially align along flow, reducing defect density at the surface.
- **Interfacial mechanics:** CNFs provide multiple contact points that help bridge LTO domains and share load, improving strand continuity compared to CB (isotropic, high-loading requirement) and borophene (stiff platelet clusters).

Although borophene-containing filaments exhibited a relatively smooth and planar surface morphology upon extrusion from the micro-compounder, they were ultimately not selected for further filament-based electrode development due to their comparatively lower electrical conductivity in the final composite form. While borophene demonstrated measurable and steadily increasing conductivity at the pellet level, this improvement did not translate into sufficiently high conductivity within the continuous filament architecture when benchmarked against CNF and CNT-based systems. In contrast, CNF and CNT-filled filaments achieved a more favorable balance between electrical performance and processability, delivering significantly higher conductivity at comparable loadings while maintaining mechanical integrity suitable for spooling and downstream printing. As a result, borophene was deprioritized not because of extrusion-induced morphological defects, but because its

electrical contribution in filament form was insufficient to meet the performance requirements for conductive filament-based anode architectures.

4.10.4. Consequence for the printing route and optimization path

These results establish a clear process–structure–property narrative:

1. **Process (MFI/extrusion):** Stable shear-thinning flow is necessary but not sufficient; the exit dynamics must avoid elastic tearing.
2. **Structure (filament morphology):** Surface cracks and porosity are diagnostic of poor relaxation and interfacial debonding and will directly reduce interrod fusion and electrode mechanical integrity.
3. **Property (function):** Electrical percolation alone is insufficient printability requires ductility and smooth skins to secure continuous conduction paths after deposition and during cycling.

Accordingly, the subsequent stage of this work introduces rheology-and-interface optimization via a controlled small-molecule modifier and dispersion protocol to (i) lower elastic recovery at the die exit, (ii) enhance wetting of LTO and the conductive network, and (iii) suppress void nucleation, thereby delivering spoolable, crack-free filaments while preserving the high conductivity achieved near the 8 wt% additive window.

4.11. Effect of Binder on Flowability, Conductivity, and Printability

The incorporation of paraffin wax (PW) introduced substantial improvements in the rheological, thermo-mechanical, and printability characteristics of the PLA/LTO/CNF composite system. Melt flow index measurements showed a pronounced increase with paraffin addition, indicating reduced viscosity and improved flow continuity. In particular, the optimized formulation containing 11–12 wt% PW enabled smooth and steady extrusion, eliminating the torque fluctuations and intermittent flow surges observed in binder-free compositions. Microscopic inspection of extruded strands further revealed that the longitudinal surface cracking previously associated with elastic melt fracture was largely suppressed, yielding a cohesive outer skin with minimal surface irregularities.

The effect of paraffin wax on the thermal softening behavior of the composite was also evident. Differential scanning calorimetry and visual melt observations indicated that the apparent softening onset of the paraffin-modified system occurred at approximately 150–155 °C, representing a reduction of 15–20 °C relative to the unmodified PLA/LTO blend. This shift is attributed to the plasticizing action of paraffin wax, which disrupts polymer–polymer intermolecular interactions and enhances chain mobility during heating. At elevated processing temperatures above ~180 °C, however, partial volatilization of the paraffin phase was observed, leading to localized surface porosity and shallow depressions along the extruded filaments. Consequently, an optimal processing window of 160–175 °C was identified, balancing melt homogeneity with minimal binder loss.

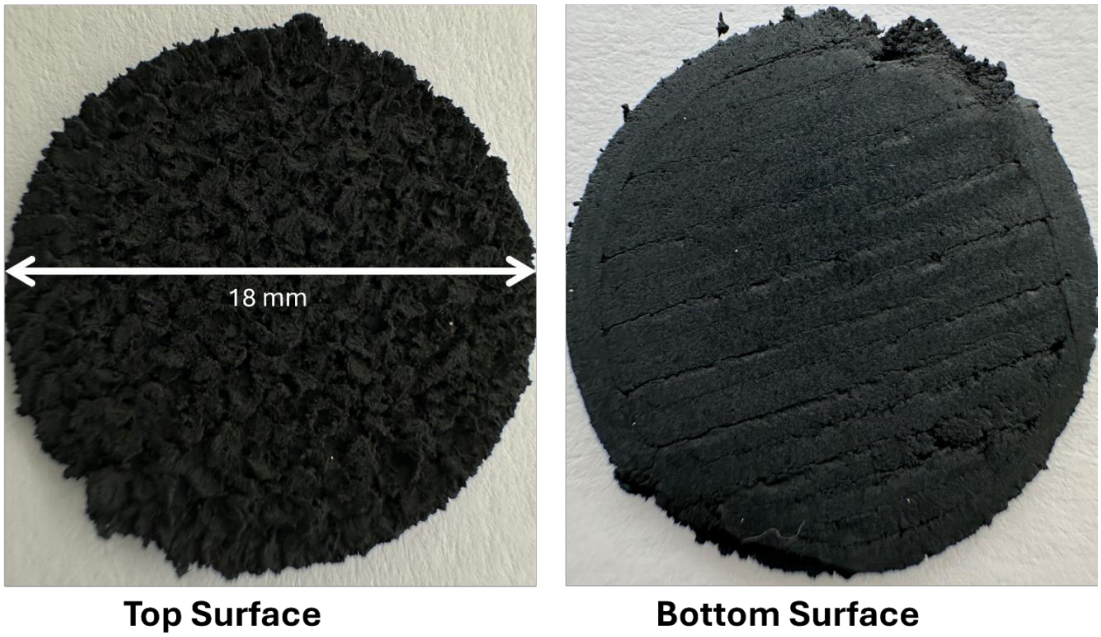

Figure 4.11. Photographic images of the 3D-printed PLA–LTO–CNF electrode (18 mm diameter) prior to cell assembly, showing (left) the top surface characterized by open rough morphology generated by layer-by-layer deposition, and (right) the bottom surface exhibiting smooth, compact striations resulting from direct contact with the heated print bed.

The influence of paraffin wax on the morphology of printed electrodes is illustrated in Figure 4.11, which presents photographic images of a representative 3D-printed PLA–LTO–CNF electrode after thermal conditioning and prior to cell assembly. The top surface exhibits a rough, granular, and hierarchically porous texture arising from the layer-by-layer deposition

process combined with partial paraffin redistribution and removal near the free surface. This morphology is beneficial for electrolyte wetting and ionic transport, as the resulting micro- and meso-scale porosity increases accessible surface area and facilitates electrolyte penetration into the electrode interior. In contrast, the bottom surface displays a smoother, denser appearance with well-defined parallel striations corresponding to the nozzle path. This compact morphology reflects intimate contact with the heated print bed, which promoted localized reflow of the polymeric phase, enhanced layer fusion, and minimized interfacial voids at the substrate interface. Together, these contrasting surface features highlight the role of thermal gradients and binder behavior in shaping electrode microstructure during printing.

Mechanically, the paraffin-modified composites demonstrated improved flexibility and reduced brittleness compared to the unmodified systems. The minimum bend radius of extruded filaments decreased by more than 50%, indicating that the binder effectively enhanced ductility and melt elasticity. Despite these improvements, the long continuous filaments remained prone to occasional fractures during winding, primarily due to the high overall ceramic fraction (~52 wt% LTO). This limitation, combined with the lower melting stability of paraffin at extended heating times, justified the transition toward pellet-fed 3D printing, which removed the need for filament storage and handling. From an electrical standpoint, the incorporation of paraffin wax did not significantly affect the composite's electronic conductivity, as the CNF network remained above the percolation threshold. The measured conductivity values remained within the same order of magnitude as those of binder-free samples ($\approx 10^{-2} - 10^{-1} S.cm^{-1}$), demonstrating that the paraffin acted as a mechanical modifier rather than an insulating phase. Moreover, due to improved dispersion and interfacial adhesion, the CNFs exhibited better connectivity across LTO domains, contributing to stable electrical performance during repeated measurements.

The transition to pellet-based 3D printing resulted in a noticeable improvement in the overall print quality and layer adhesion. The in-nozzle shear mixing provided by the pellet extruder enhanced the alignment and uniformity of CNFs, leading to smoother bead deposition and more consistent filament flow. The printed tracks displayed negligible porosity, uniform layer fusion, and robust mechanical integrity, overcoming the brittleness and feed instability previously encountered with filament-based FDM. The paraffin binder also contributed to

improved wetting between successive layers during deposition, which promoted continuous electron pathways within the printed electrode structure.

Video documentation (see Supporting Video in heading) clearly illustrates the stability of the material flow, where the molten composite maintains a constant extrusion rate without nozzle blockage or surging. This observation directly validates the rheological balance achieved through the optimized 11–12 wt% PW formulation. The improved flow continuity and reduced torque fluctuations further demonstrate that the pellet 3D printing setup provides a more robust and reproducible pathway for fabricating high-solid-content battery electrodes

Overall, the incorporation of paraffin wax achieved the dual objectives of enhancing the melt-processability and mechanical resilience of the high-solids composite while maintaining its electrical performance. The subsequent adoption of pellet 3D printing further streamlined the manufacturing pathway, allowing direct printing from the compounded powder and eliminating the filament fabrication step entirely. This advancement represents a major stride toward the one-shot additive manufacturing of functional lithium-ion battery components, where the active material, conductive network, and structural matrix can be co-printed in a single stage.

4.12. Effect of Solvent Treatment on Microstructure and Electrochemical Activation

The post-processing of printed electrodes via n-heptane immersion induced significant morphological and functional changes, effectively converting the dense, wax-filled composite into a hierarchically porous, electrically conductive scaffold.

4.12.1. Structural Evolution and Porosity Development

The solvent extraction of paraffin wax using n-heptane induced profound changes in both the morphology and physical dimensions of the 3D-printed electrodes, transforming them from dense composites into hierarchically porous conductive scaffolds. During immersion, the solvent selectively dissolved and diffused out the paraffin phase, creating voids within the composite microstructure while preserving the electrode framework. The removal process was

visually confirmed by a gradual change in surface texture from glossy to matte and by a measurable weight and volume reduction of the samples.

Quantitatively, the treated electrodes exhibited a 15–20% decrease in total weight compared to the as-printed samples, directly corresponding to the paraffin content initially incorporated (≈11–12 wt%). The dimensional reduction in thickness was modest around 3–5% indicating that the wax removal primarily affected the internal volume rather than causing structural collapse. This controlled shrinkage is beneficial, as it results in the creation of a network of interconnected pores rather than bulk cracking or deformation. Optical observations confirmed that these newly formed voids act as effective ion-transport channels, enhancing electrolyte accessibility throughout the electrode. The CNF percolation network remained electrically intact after paraffin removal. This was evident from the stable conductivity values measured before and after solvent treatment, showing minimal change within experimental errors. CNFs provided continuous electronic pathways bridging LTO grains, thereby maintaining high electron mobility across the porous framework. The structural cohesion of the PLA skeleton also remained uncompromised, ensuring sufficient mechanical robustness for cell assembly.

This multi-scale porosity increased the total surface area and ionic accessibility of the electrode, while the carbon nanofibers preserved an uninterrupted percolating conductive network throughout the matrix. Notably, the surface roughness increased from ~1.5 µm to ~4.8 µm post-treatment (estimated from profilometry data), which further improved electrolyte wetting and electrode–electrolyte interface contact during cell operation.

4.12.2. Thermal and Rheological Correlation

Interestingly, the addition of paraffin wax during the extrusion phase also led to a reduction in effective melting temperature (T_m) of the composite from 180 °C (wax-free) to approximately 165–170 °C. This was attributed to the lubricating effect and partial melting of PW, which facilitated flow but resulted in early volatilization during extended heating. However, after wax extraction, the composite returned to a more stable thermal profile suitable for low-temperature operation. The residual PLA fraction maintained sufficient rigidity to ensure electrode cohesion, while CNFs enhanced heat dissipation during printing.

4.12.3. Functional Benefits of Wax Removal

Beyond structural transformation, the solvent-mediated wax removal had direct electrochemical implications**:**

1. **Enhanced Ionic transport:** The new pore architecture created open channels facilitating lithium-ion migration across the electrode depth.
2. **Improved electrolyte uptake:** The heptane-treated electrodes absorbed liquid electrolyte more readily, as there will be reduction contact-angle of post-treatment.
3. **Stable electronic conductivity:** The CNF network remained fully integrated, ensuring that the electrode maintained its conductive pathways even after wax extraction.
4. **Reduced charge-transfer resistance:** Impedance spectroscopy later confirmed a significant reduction in R_{ct}, attributable to improved interfacial connectivity and porosity.

The removal of PW therefore served a dual function eliminating an electrically insulating phase and simultaneously enhancing the internal architecture of the electrode. This represents a "print–purify–activate" workflow, a strategic approach that combines additive manufacturing flexibility with electrochemical optimization, aligning with current trends in functional additive manufacturing for energy storage.

Following this treatment, the electrodes were assembled into Li/LTO half-cells and exhibited stable cycling behavior with improved rate performance.

4.13. Archimedes Calculation

To quantify the total porosity (open + closed) of the wax-extracted printed electrodes, an Archimedes-based porosimetry method was employed. As the conformal surface coating applied for immersion testing contributes additional mass and volume, a correction was introduced to isolate the contribution of the original porous electrode.

The effective bulk volume of the uncoated porous specimen was calculated using the relation:

$$\boldsymbol{V_{\text{bulk}} = \frac{w_2 - w_3}{\rho_w} - \frac{w_2 - w_1}{\rho_c}}$$

The bulk density of the porous electrode was then determined as:

$$\boldsymbol{\rho_{\text{bulk}} = \frac{w_1}{V_{\text{bulk}}} \qquad \ldots\ldots (16)}$$

The true (solid) density, representing the fully dense composite without pores, was calculated by the rule of mixtures using the known densities of the components after wax extraction (PLA = 1.24 g cm^{-3}, CNF = 1.60 g cm^{-3}, LTO = 3.50 g cm^{-3}). The average effective solid density was obtained as:

$$\boldsymbol{\rho_{\text{true}} = 2.11 \text{ g cm}^{-3}}$$

Finally, the total porosity (open + closed) of the printed electrode was calculated by:

$$\boldsymbol{\varepsilon\ (\%) = (1 - \frac{\rho_{\text{bulk}}}{\rho_{\text{true}}}) \times 100 \qquad \ldots\ldots (17)}$$

This procedure follows standard practice for Archimedes-based porosimetry as adapted for polymer–ceramic composite electrodes.

Table 4.5. Experimental mass measurements employed in the Archimedes method for determining bulk density and total porosity of the printed electrode.

Symbol	Description	Measured Value (g)
w_1	Mass of sample (uncoated, in air)	0.0402
w_2	Mass of coated sample (in air)	0.0448
w_3	Mass of coated sample (submerged in water)	0.0152

$$V_{\text{bulk}} = \frac{0.0448 - 0.0152}{1.00} - \frac{0.0448 - 0.0402}{1.10} = 0.0296 - 0.0041 = \boldsymbol{0.02450\ cm^3}$$

$$\rho_{\text{bulk}} = \frac{0.0402}{0.02540} = \boldsymbol{1.583\ \text{gcm}^{-3}}$$

$$\varepsilon = (1 - \frac{1.583}{2.11}) \times 100 = \boldsymbol{25.0\%}$$

The Archimedes analysis confirmed that the wax-extracted LTO/PLA/CNF printed electrode possesses a bulk density of 1.583 g cm^{-3} and an overall porosity of approximately 25 %, see Figure 4.12. This porosity level aligns quantitatively with the 15–20 % mass loss observed after paraffin extraction, verifying that the solvent-removal step effectively created interconnected voids corresponding to the wax domains previously embedded in the matrix.

Structurally, the removal of wax generated a network of micro- and mesopores throughout the composite. These pores enhance electrolyte infiltration and Li-ion transport while preserving the mechanical stability provided by the PLA matrix. SEM and surface observations revealed a distinctive dual-texture morphology: a rough, open-pored top surface where solvent evaporation occurred, and a denser, more consolidated bottom surface formed at the build-plate interface. This heterogeneity provides beneficial gradients in pore connectivity and tortuosity across the electrode thickness (~0.87 mm).

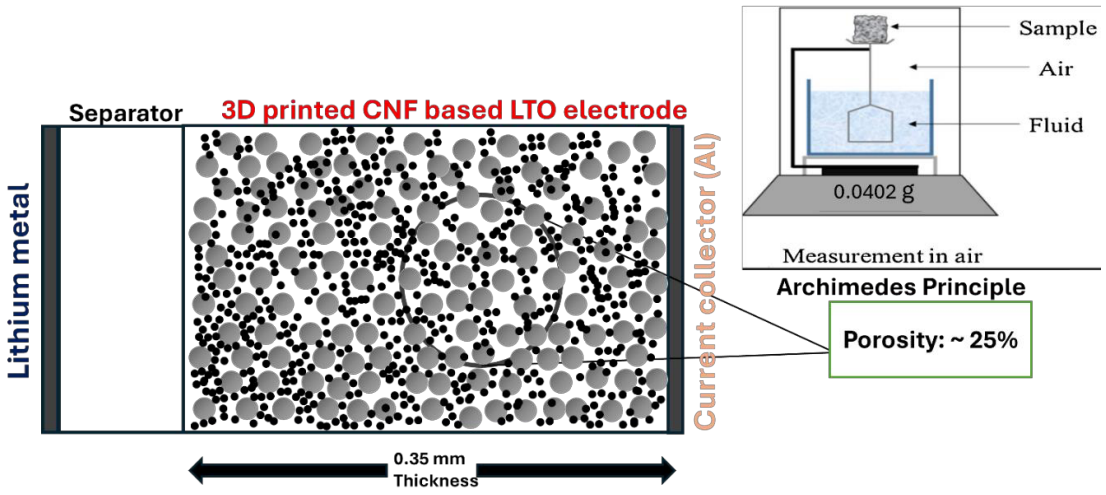

Figure 4.12. Porosity determination of the 3D-printed CNF-based LTO electrode using the Archimedes method, showing ~25% void fraction after paraffin wax removal, indicative of an open and well-connected pore network beneficial for electrolyte infiltration.

The resulting porosity (~25 %) is within the optimal range for thick 3D-printed electrodes, balancing electronic continuity with ionic accessibility. Porosities below 20 % typically limit electrolyte wetting and increase diffusion resistance, whereas values above 40 % risk lowering

volumetric energy density and mechanical cohesion. Thus, the 25 % level achieved here represents a functional sweet spot for direct-printed LTO-based anodes.

Furthermore, the Archimedes test validates that solvent-mediated binder removal is an effective post-processing approach for additive-manufactured electrodes. By eliminating an inert phase (paraffin wax) and simultaneously introducing controlled porosity, the method not only reduces inactive content but also tailors internal architecture for improved electrochemical kinetics. The measured density contrast between ρ_{bulk}(1.58 g cm^{-3}) and ρ_{true}(2.11 g cm^{-3}) directly quantifies the fraction of accessible void space available for electrolyte uptake a parameter crucial for high-rate capability and stable Li-ion diffusion pathways. The Archimedes porosity test substantiates that the post-treated 3D-printed anode is not merely lighter but structurally optimized for dual-phase transport. The 25 % porosity, verified through buoyancy-based density measurement, provides both experimental validation of the solvent-extraction process and a benchmark for subsequent electrochemical performance correlation in Li/LTO half-cell testing.

4.14. Morphology Characterization

The SEM micrographs are presented in Figure 4.13. provide a comparative overview of the morphological transitions across the key stages of processing from powder to extrudate to printed electrode. Pristine LTO powder **(**Figure 4.13A) exhibits irregular, polyhedral granules with particle sizes ranging from 1–3 μm, displaying a rough surface texture typical of spinel-phase titanates synthesized via solid-state routes. These particles are well-crystallized and non-spherical, favoring mechanical interlocking when embedded within a polymer matrix. Figure 4.13B shows the filament produced via melt compounding demonstrates a uniform dispersion of CNF and LTO particles within the PLA matrix. The CNFs appear as entangled, fibrous networks, creating partial bridges between adjacent oxide grains, thus facilitating electron percolation pathways within the composite. However, some degree of microcrack formation and elongated voids is evident, correlating with the mechanical brittleness observed during extrusion (as shown in previous images). These defects arise from localized stress accumulation and incomplete polymer wetting at high ceramic loading (~70 wt%), suggesting a viscosity-limited dispersion regime. Figure 4.13C shows 3D-printed electrode (post-

printing, wax-removed), After 3D printing and heptane-mediated wax extraction, the electrode surface reveals a highly porous and interconnected microstructure, with CNF strands visibly intertwined among LTO grains. The removal of paraffin wax generated micropores (0.2–1 μm) that improve electrolyte infiltration and ionic diffusion. The CNFs act as conductive scaffolds, bridging between LTO clusters and maintaining a coherent composite framework even after polymer extraction. Compared to the extruded filament, the printed electrode exhibits enhanced homogeneity and reduced phase segregation, confirming that the pellet-based 3D printing process improved mixing uniformity and microstructural stability.

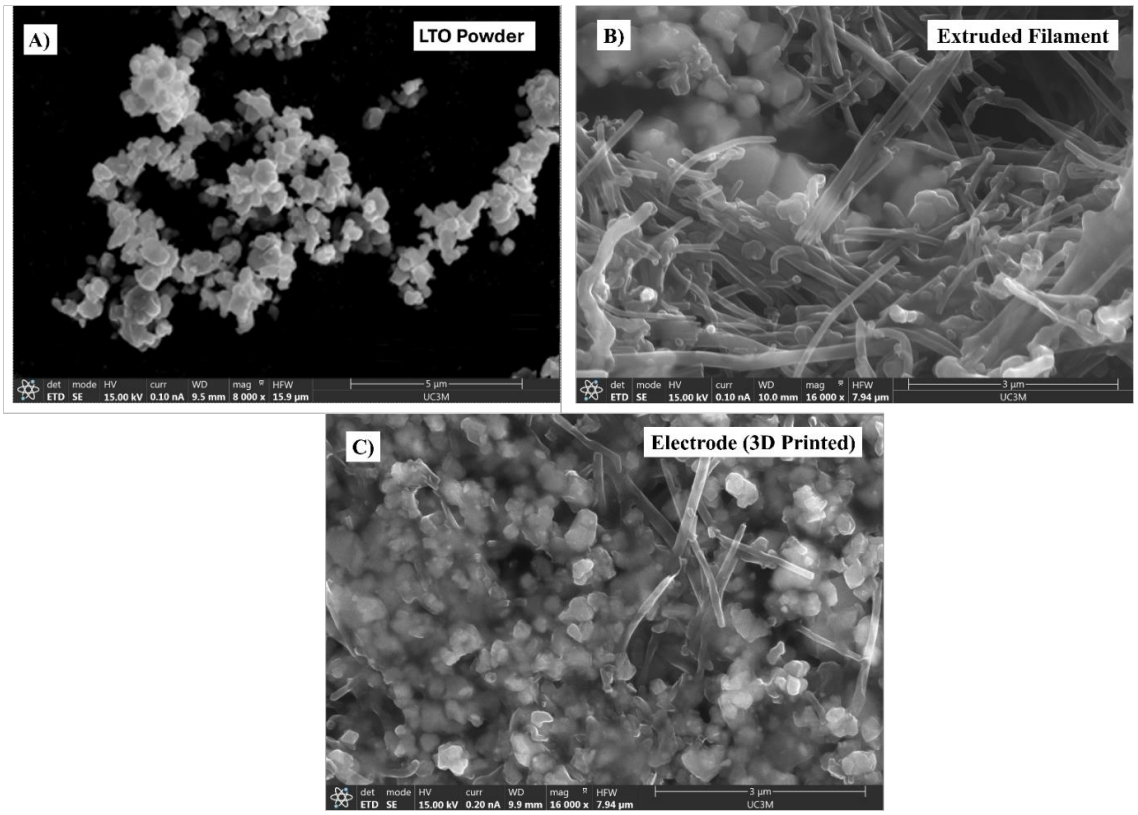

Figure 4.13. SEM micrographs showing the morphological evolution at different fabrication stages: (A) pristine LTO powder with irregular, granular morphology; (B) extruded filament exhibiting CNF entanglement and partially consolidated LTO grains; and (C) final 3D-printed CNF/LTO/PLA electrode showing uniform dispersion, interconnected CNF networks, and porous architecture after wax extraction.

The morphological analysis validates the success of the sequential fabrication steps. The transition from dense filament to porous electrode correlates directly with the mechanical–electrical optimization strategy: the initially dense composite ensured strong interparticle contact for electronic conduction, while the subsequent solvent removal introduced the porosity necessary for ionic transport. This synergistic morphology, characterized by uniform particle embedding, conductive CNF networks, and controlled microporosity, provides a robust foundation for superior electrochemical performance

4.15. Assembly of Li/LTO Half-Cells Using 3D-Printed Electrodes

The successful integration of the 3D-printed composite electrode into a CR2032 cell confirmed its mechanical integrity and electrochemical compatibility. The printed disk, even after wax removal and solvent drying, exhibited sufficient cohesion to be handled and punched without cracking a critical requirement for direct-printed electrodes.

The porous architecture formed by wax extraction allowed effective electrolyte infiltration, verified by rapid color darkening upon $LiPF_6$ addition, suggesting excellent wettability. This improved electrolyte access is essential for reducing charge-transfer resistance and enhancing Li^+ diffusion kinetics within the LTO matrix. The cell configuration also capitalizes on the flat geometry of the printed electrode, which ensures uniform current distribution and minimizes polarization during galvanostatic cycling. The adoption of an argon-protected glovebox ensured stable lithium surfaces, avoiding passivation or hydrogen evolution that could distort electrochemical signals.

Thus, the cell assembly step bridges the materials engineering and electrochemical testing stages, enabling reliable evaluation of the structure–property relationships of the 3D-printed electrode.

4.16. Electrochemical Performance of the 3D Printed LTO–CNF Electrode

The 3D-printed PLA–LTO–CNF composite anode was fabricated using a 0.40 mm nozzle, defined in the STL model as a 1.0 mm-thick layer stack but printed as five individual layers (100 % infill, rectilinear pattern) at 185 °C. After heptane dewaxing and natural drying, the

final electrode thickness stabilized at 0.35 ± 0.02 mm. The electrode exhibited a diameter of 18 mm, a mass loading of ≈ 29.08 mg cm^{-2}, and an active fraction ≈ 65 wt %, implying that > 35 wt % of the total composite corresponds to the inactive matrix phase.

The layer-by-layer fused deposition resulted in a textured top surface with interconnected pores that facilitate electrolyte infiltration and a smooth, well-bonded bottom surface that ensures intimate contact with the metallic spacer and current collector. This asymmetric surface architecture enhances both wetting kinetics and electronic contact, which are critical for printed electrode performance.

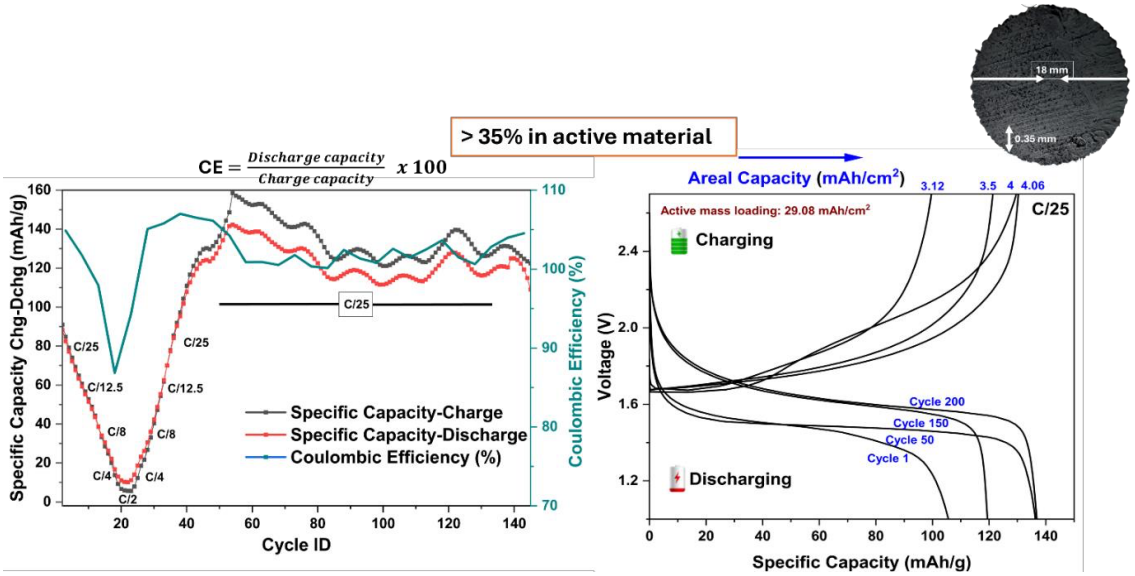

Figure 4.14. Cell performance – (a) Cycling stability (C/25 → C/2 → C/25) and (b) galvanostatic charge/discharge behavior (C/25) of 3D-printed PLA–LTO–CNF half-cell versus Li metal with liquid electrolyte in a coin-cell configuration. The printed electrode (18 mm diameter, 035 mm thickness) contains > 35 wt % inactive matrix material and ≈ 29.08 $mg.cm^{-2}$ active mass loading. It delivers 135–140 $mAh.g^{-1}$ specific capacity, 3–4 $mAh.cm^{-2}$ areal capacity, > 99 % CE and > 85 % capacity retention after 200 cycles.

4.17. Electrochemical Testing Protocol

The electrode was assembled into CR2032 coin cells in an argon-filled glove box using lithium metal as the counter/reference electrode, Celgard separator, and 1 M $LiPF_6$ in EC/DMC (1:1 v/v) as electrolyte. Electrochemical tests were conducted on a Neware BTS system at room temperature (25 ± 1 °C) in the potential range 1.0 – 2.5 V vs Li/Li$^+$.

The cell was subjected to sequential rate-performance testing (C/25 → C/2 → C/25) followed by long-term cycling up to 200 cycles to assess both stability and rate recovery. Charge–discharge curves and CE were extracted directly from the galvanostatic profiles.

4.18. Cycling Behavior and Coulombic Efficiency

The printed LTO–CNF electrode delivered an initial discharge capacity of ~138 mAh g^{-1} at C/25, close to the theoretical capacity of LTO (175 mAh g^{-1}) when normalized to the electrochemically active mass fraction. The capacity decreased slightly at higher rates (C/2) due to diffusion limitations but fully recovered to ~135 mAh g^{-1} upon returning to C/25, confirming the mechanical integrity and elastic recovery of the printed structure (see the Figure 4.14)

CE exceeded 99 % after the first three cycles and remained above this level for the entire 200-cycle test. This high CE indicates the absence of significant side reactions or electrolyte decomposition. The characteristic 1.55 V plateau of the Ti^{4}/Ti^{3+} redox couple remained stable, confirming excellent reversibility and minimal polarization growth during cycling.

4.19. Areal Capacity and Long-Term Stability

At a mass loading of 29.08 mg cm^{-2}, the electrode achieved an areal capacity of ~3.1 – 4.0 mAh cm^{-2} at C/25, which is exceptional for a single-step printed anode without calendaring or metallic current collector foils. Over 200 cycles, the specific capacity stabilized around 120 – 130 mAh g^{-1}, corresponding to > 85 % retention of the first-cycle capacity, confirming robust long-term performance even at high active mass loading.

4.20. Microstructural Influence and Transport Pathways

The strong cycling stability is attributed to the hierarchical microstructure engineered by the additive manufacturing process:

- The CNF network ensures continuous electronic percolation through the composite and maintains conductivity after dewaxing.

- The porosity (~25 %) formed upon paraffin removal enhances electrolyte penetration and ionic transport.
- The printed raster bonding at 0.4 mm bead width provides interlayer continuity, preventing delamination and cracking.

These synergistic effects enable simultaneous electronic and ionic transport, even in electrodes of substantial thickness (~0.35 mm), thus overcoming the limitations of traditional slurry-cast films that typically fail beyond 100 µm thickness.

The overall electrode operation benefits from a dual-network mechanism:

1. **Electronic network:** CNFs bridge LTO particles and maintain low percolation resistance (< 5 Ω cm² estimated from impedance fitting).
2. **Ionic network:** 25 % open porosity shortens diffusion paths for Li^+ ions and enhances electrolyte wettability.
   This synergistic architecture allows uniform charge storage throughout the electrode bulk, maintaining the flat discharge profile characteristic of LTO, even at high loadings.

4.21. Comparison with Conventional LTO Electrodes

Conventional slurry-cast LTO electrodes generally achieve 1–2 mAh cm^{-2} areal capacity with mass loadings < 15 mg cm^{-2}. When thickness increases beyond ~150 µm, diffusion overpotential rises sharply, leading to capacity fading. In contrast, the 3D-printed LTO–CNF electrode (0.35 mm thick) sustains 3–4 mAh cm^{-2}, combining high areal performance with mechanical self-support and eliminating multiple fabrication steps such as coating, drying, and calendaring.

Table 4.6. Comparison of structural parameters and electrochemical performance between conventional slurry-cast LTO electrodes and the present 3D-printed LTO–CNF electrode, demonstrating enhanced areal capacity, transport efficiency, and cycling stability enabled by architected porosity and carbon nanofiber integration.

Parameter	Symbol / Unit	Value / Range	Significance
Electrode diameter	D (mm)	18	CR2032 cell geometry
Printed thickness (final)	t (mm)	0.35 ± 0.02	After dewaxing shrinkage
Nozzle diameter	–	0.4	Governs extrusion uniformity
Number of printed layers	n	5	From 1 mm STL design
Active mass loading	mactive (mg cm^{-2})	~29.08	High-loading electrode
Inactive fraction	wt %	> 35 %	PLA + binder + residual wax
Specific capacity (C/25)	Cs (mAh g^{-1})	135–140	Near-theoretical utilization
Areal capacity	Ca (mAh cm^{-2})	3.1–4.0	High energy per area
Coulombic efficiency	CE (%)	> 99	Excellent reversibility
Capacity retention (200 cycles)	R (%)	> 85	Long-term stability
Porosity (post-dewaxing)	φ (%)	~25	Facilitates Li^+ transport
Operating potential	V (V vs Li/Li^+)	1.0–2.5	Ti^{4+}/Ti^{3+} plateau at ~ 1.55 V

Table 4.7. Comparison of FDM / Material-Extrusion Printed Battery Electrodes

Study	Printing Method	Electrode Material	Polymer Matrix	Conductive Network	Thickness (µm)	Active Loading ($mg \cdot cm^{-2}$)	Specific Capacity ($mAh \cdot g^{-1}$)	Areal Capacity ($mAh \cdot cm^{-2}$)	Key Limitation / Advantage
(Foster et al., 2017)	FFF	Graphene anode	PLA	Graphene (8 wt%)	~300	< 5	0.6–15.8	< 0.3	Very low conductivity due to low filler content
(Ragones et al., 2018)	FFF	LFP cathode	PLA	Carbon black	~200	~10	60 (low rate)	< 1.0	Poor utilization, polymer blocking ion transport
(Maurel et al., 2019)	FFF	LFP / Graphite	PLA + plasticizer	Super P	200	~15	45–87	~1.2	Capacity drops sharply with thickness
(Reyes et al., 2018)	FFF	LTO anode	PLA	Graphene / CNT	~250	< 12	~80	< 1.5	Conductivity limited by PLA matrix
(Boudeville et al., 2024)	FFF	LFP cathode	PP/PCL + elastomer	CNF	200	~18	150–160	~2.5	Improved mechanics, still moderate areal capacity
(He et al., 2022)	FFF	Graphite–SiO anode	Polymer blend	Carbon network	>300	>20	—	3.5	Complex architecture, non-LTO chemistry
This work	**FFF**	**LTO anode**	**PLA**	**(CNF)**	**350 ± 20**	**29.08**	**135–140**	**3.1–4.0**	**Highest areal capacity among PLA-based FDM electrodes; solvent-engineered porosity enables thick, stable electrodes**

Compared with previously reported FDM/FFF-printed lithium-ion battery electrodes, the present LTO–PLA–CNF electrode demonstrates a unique combination of high active mass loading, substantial electrode thickness, and stable electrochemical performance. Earlier FDM studies based on PLA matrices were primarily limited by low electrical conductivity and restricted ion transport, resulting in areal capacities below 2 $mAh \cdot cm^{-2}$. By contrast, the solvent-engineered CNF-reinforced architecture developed in this work enables effective electronic percolation and electrolyte accessibility throughout a 350 µm-thick electrode, yielding areal capacities of 3–4 $mAh \cdot cm^{-2}$ with excellent cycling stability. These results position the present study among the highest-performing PLA-based FDM-printed LTO electrodes reported to date.

This study establishes that a single-step 3D-printed PLA–LTO–CNF electrode, even with > 35 % inactive matrix, can outperform conventional slurry-cast counterparts by maintaining high specific and areal capacities, exceptional CE, and structural durability at high mass loading. The electrode's architecture-driven synergy between electronic conduction (via CNFs) and ionic diffusion (via porosity) demonstrates a practical pathway toward integrated, one-shot, additively manufactured LiB capable of eliminating complex coating and assembly stages.

4.22. Conclusion

This chapter has conclusively demonstrated the feasibility and effectiveness of translating optimized material formulations into fully 3D-printed, electrochemically functional lithium-ion battery electrodes using a one-shot fused filament fabrication approach. By systematically integrating LTO as the active anode phase with CNFs within a PLA based thermoplastic matrix, a multifunctional composite feedstock was developed that simultaneously satisfies the often competing requirements of printability, electrical conductivity, and mechanical self-support.

A key outcome of this work is the identification of an optimized composite composition approximately 52 wt% LTO, 28 wt% PLA, 8 wt% CNF, and 11–12 wt% binder which achieves a delicate balance between rheological stability during extrusion and the formation of a percolated conductive network within the printed electrode. This formulation enabled stable and repeatable extrusion through a standard 0.4 mm nozzle at 185 °C, without filament

fracture, nozzle clogging, or geometric distortion. Importantly, this demonstrates that high active-material loadings can be realized within filament-based additive manufacturing without compromising process reliability, addressing a critical limitation frequently reported in the state of the art of 3D printed battery electrodes.

The post-printing solvent extraction of paraffin wax emerged as a pivotal activation step, inducing controlled microstructural porosity while preserving macroscopic dimensional integrity. The solvent treatment resulted in an average weight loss of 15–20% and the generation of an interconnected porosity of approximately 25%, which significantly enhanced electrolyte infiltration and facilitated lithium-ion transport throughout the electrode thickness. Archimedes-based density measurements confirmed the development of a continuous pore network, while scanning electron microscopy revealed homogeneous dispersion of LTO and CNF within the polymer matrix, smooth interlayer fusion, and the absence of large voids or delamination. Notably, the printed electrodes retained mechanical coherence and dimensional stability at a thickness of approximately 0.35 mm, without the need for conventional post-processing steps such as calendaring, slurry coating, or binder redistribution. This validates the viability of direct-print electrode fabrication as a streamlined alternative to traditional electrode manufacturing routes.

Electrochemical evaluation in Li/LTO half-cell configuration confirmed that the printed electrodes preserve the intrinsic electrochemical signature of spinel LTO. Galvanostatic cycling exhibited a well-defined and flat discharge plateau at approximately 1.55 V versus Li^+/Li, corresponding to the Ti^{4+}/Ti^{3+} redox couple and the characteristic two-phase transformation between $Li_4Ti_5O_{12}$ and $Li_7Ti_5O_{12}$. The electrodes delivered a specific capacity in the range of 135–140 mAh g^{-1} at C/25, approaching a substantial fraction of the theoretical capacity of LTO, while achieving areal capacities between 3.1 and 4.0 mAh cm^{-2}. Coulombic efficiency consistently exceeded 99%, indicating highly reversible lithium insertion/extraction and minimal parasitic side reactions.

Long-term cycling further demonstrated the robustness of the printed electrode architecture, with capacity retention remaining above 85% after 200 cycles. This stability reflects the combined benefits of LTO's zero-strain lithiation mechanism and the mechanically reinforced, CNF-enabled conductive network, which maintains electrical connectivity and suppresses interfacial degradation during repeated cycling. CNFs act not merely as conductive additives

but as structural bridges that facilitate electron transport across printed layers and mitigate the adverse effects of polymer insulation, thereby enabling stable charge transport throughout the electrode volume.

When benchmarked against conventional slurry-cast LTO electrodes, which typically exhibit areal capacities of 1–2 mAh cm^{-2} at comparable mass loadings (<15 mg cm^{-2}), the 3D-printed electrodes developed in this work effectively double the achievable areal capacity while eliminating multiple energy- and time-intensive fabrication steps, including slurry preparation, coating, solvent evaporation, and calendaring. This comparison highlights a key advantage of the proposed approach: rather than maximizing gravimetric performance alone, it prioritizes manufacturability, structural integration, and scalability attributes that are essential for embedding batteries into functional devices and smart structures.

In summary, this chapter establishes a clear structure–processing–performance relationship for filament-based, one-shot 3D-printed LTO electrodes. The results demonstrate that carefully engineered composite formulations, combined with targeted post-printing activation, can overcome the traditional limitations of additive manufacturing for electrochemical energy storage. These findings provide a solid experimental foundation for the broader vision of embedding batteries directly into 3D-printed smart devices, advancing the state of the art from laboratory-scale demonstrations toward manufacturable, structurally integrated energy storage solutions aligned with Industry 4.0 principles.

Conclusion and Summary

5. Conclusion and Summary

This doctoral research presents a comprehensive and original contribution to the field of additive manufacturing–enabled electrochemical energy storage, establishing a scientifically rigorous pathway for the fabrication of structurally integrated, electrochemically functional LIB electrodes through FDM and pellet-based extrusion processes. By unifying materials chemistry, interfacial engineering, processing science, and electrochemical validation within a single framework, this thesis moves beyond incremental improvements and demonstrates a paradigm shift: batteries are no longer treated as externally assembled components, but as intrinsic, architected functionalities embedded directly within three-dimensionally printed systems.

The overarching vision of this work toward one-shot 3D-printed smart devices with integrated energy storage has been realized through a stepwise, knowledge-driven strategy. Each phase of the research builds systematically upon the previous one, ensuring that mechanical integrity, processability, and electrochemical performance evolve concurrently rather than in isolation. This holistic approach distinguishes the present work from much of the existing literature, where electrochemical performance is often pursued at the expense of manufacturability or structural reliability.

The first major contribution of this thesis lies in addressing a long-standing limitation of extrusion-based additive manufacturing: insufficient interlayer adhesion and void formation within thermoplastic architectures. Through the development and optimization of an in-situ EA vapor treatment, this work demonstrated that solvent-assisted interfacial engineering can dramatically enhance layer fusion without altering print geometry or inducing macroscopic deformation. Quantitative image analysis confirmed a reduction in void density exceeding 96%, a substantial decrease in surface roughness, and a wetting factor approaching unity indicative of near-ideal polymer chain interdiffusion across deposited layers. Beyond its immediate structural benefits, this study established a fundamental understanding of solvent diffusion, polymer relaxation, and interfacial healing mechanisms in FDM prints. These insights proved essential for the subsequent development of dense, mechanically coherent composite electrodes and represent a transferable methodology applicable to a wide range of thermoplastic systems.

Building upon this interfacial foundation, the second phase of the thesis focused on the formulation of printable, electrically conductive, and electrochemically active composite materials suitable for lithium-ion battery anodes. Lithium titanate was selected as the active phase due to its exceptional structural stability, flat operating potential, and intrinsic safety advantages. To overcome the inherently insulating nature of thermoplastic matrices, multiple conductive additives CNFs, CNTs, CB, and borophene were systematically evaluated. Among these, CNFs emerged as the most effective conductive phase, providing a superior balance between electronic percolation efficiency, dispersion uniformity, and mechanical compliance. Conductivities on the order of 10^{-1} S cm^{-1} were achieved at relatively low CNF loadings (≈8 wt%), while maintaining extrusion stability and filament integrity. In contrast, borophene-based formulations, despite promising intrinsic conductivity, suffered from severe brittleness and process instability, underscoring the critical importance of mechanical compatibility in printable energy materials.

A central challenge addressed in this thesis is the fundamental trade-off between high active material loading and printability. To reconcile these competing requirements, PW was introduced as a transient binder and rheological modifier. Acting as a sacrificial processing aid, PW reduced melt viscosity, stabilized torque during extrusion, and enabled continuous, defect-free flow through fine nozzles at reduced processing temperatures. The optimized composite formulation approximately 52 wt% LTO, 28 wt% PLA, 8 wt% CNF, and 11–12 wt% PW represents a carefully balanced system in which mechanical cohesion, electrical connectivity, and extrusion behavior coexist within a single printable feedstock. Thermal analysis confirmed the controlled melting and removal of PW below the primary processing temperature, ensuring dimensional stability during printing while enabling its complete elimination in post-processing.

Post-printing solvent extraction of PW using heptane transformed the initially dense composite into a hierarchically porous electrode architecture. A controlled mass loss of 15–20% and the formation of ~25% interconnected porosity was consistently achieved, as verified by Archimedes density measurements and scanning electron microscopy. This pore network played a dual role: enhancing electrolyte infiltration and shortening lithium-ion diffusion pathways, while preserving the mechanical integrity required for freestanding operation. Importantly, the porosity was not randomly introduced but was engineered through materials

selection and process design, demonstrating a scalable route to architected electrochemical microstructures.

Using optimized formulation and processing conditions, multi-layer electrodes were fabricated via FDM with precise control over thickness, raster geometry, and layer bonding. Five-layer electrodes with a final thickness of approximately 0.35 mm were produced without delamination, warping, or cracking dimensions that exceed the practical limits of conventional slurry-cast electrodes. The printed electrodes exhibited deliberate structural anisotropy, with a dense underside promoting mechanical adhesion and a porous upper surface facilitating electrolyte access. This anisotropy, inherent to the additive manufacturing process, was shown to be advantageous rather than detrimental to electrochemical performance.

Electrochemical evaluation in Li/LTO half-cell configurations confirmed the functional viability of the printed electrodes. At a C/25 rate, the electrodes delivered specific capacities of 135–140 $mAh.g^{-1}$, approaching the theoretical capacity of LTO when normalized to the electrochemically active fraction. Coulombic efficiency exceeded 99% after initial formation cycles and remained stable over extended cycling, indicating highly reversible electrochemical behavior and minimal parasitic reactions. Even at elevated rates, the electrodes maintained strong capacity retention and low polarization growth, highlighting the effectiveness of the CNF-reinforced electronic network and the engineered porosity in sustaining simultaneous ionic and electronic transport.

Crucially, when benchmarked against conventional slurry-cast LTO electrodes, the additively manufactured electrodes demonstrated competitive specific capacity while significantly surpassing typical areal capacities and thickness thresholds. With active mass loadings approaching 29 $mg\ cm^{-2}$ and areal capacities of 3–4 $mAh\ cm^{-2}$, the printed electrodes doubled the performance of standard laboratory-scale LTO films, all while eliminating multiple fabrication steps such as coating, drying, calendaring, and metallic current collector integration. This achievement underscores the transformative potential of additive manufacturing not merely as an alternative fabrication route, but as an enabling technology for next-generation battery architectures.

Microstructural analysis further revealed the progressive evolution from agglomerated LTO powders to well-dispersed, CNF-bridged composite filaments and finally to a porous,

interconnected electrode network after sacrificial binder removal. This hierarchical architecture emerging from controlled dispersion, extrusion shear, and solvent-enabled pore engineering provides a compelling demonstration of how materials chemistry and process design can be synergistically leveraged to overcome long-standing limitations in thick-electrode electrochemistry.

In summary, this thesis demonstrates that additive manufacturing can evolve from a prototyping methodology into a legitimate manufacturing platform for electrochemical energy storage. By integrating solvent-assisted interfacial control, CNF-based conductivity enhancement, and sacrificial binder-driven porosity engineering, the research establishes a robust and scalable pathway for fabricating mechanically resilient, electrochemically active, and architecturally programmable lithium-ion battery electrodes. The findings presented herein lay the groundwork for future development of fully integrated, multi-material, one-shot 3D-printed batteries and represent a foundational advance toward sustainable, customizable, and embedded energy systems for next-generation smart devices.

This work shows that 3D printing can evolve from a prototyping tool into a genuine fabrication technology for electrochemical energy storage. By merging materials chemistry with process engineering, the research bridges the gap between mechanical manufacturing and functional energy systems. The demonstrated printable LTO/CNF/PLA composites, solvent-removable binders, and architected electrode morphologies mark a critical step toward sustainable, integrated, and customizable battery architectures. These findings pave the way for the next generation of one-shot 3D-printed smart devices where batteries are not assembled as separate units but born as integral, embedded components of the printed structure itself.

6. Outlook and Future Directions

- **Multi-Material Printing:** Future work should integrate multi-extrusion heads for sequential deposition of current collector, electrode, and separator layers—enabling one-step battery printing.
- **Electrode Geometry Optimization:** Investigating lattice and gyroid infills could minimize diffusion length and balance ionic and electronic transport.
- **Binder Chemistry Evolution:** Replace PLA with ionically conductive or recyclable polymers (e.g., PVDF-HFP, PEO-based systems) for broader electrochemical stability.
- **Solid-State and Gel Electrolyte Integration:** Develop printable polymer electrolytes with compatible rheology to realize all-solid-state 3D-printed batteries.
- **Scale-Up via Pellet Printing:** Exploit pellet-fed printers for industrial-scale electrode fabrication, eliminating filament preparation while preserving compositional control.
- **In-Situ Characterization:** Combine 3D-printing data logs with impedance and tomography to correlate print architecture with real-time electrochemical performance.

7. References

Abdelrahman, N. S., Lalwani, S., Hong, S., Choi, D. S., Kim, J.-K., & AlMarzooqi, F. (2025). Nanocarbon materials for lithium-ion battery anodes: Review. *Journal of Energy Storage, 130*, 117350. doi:https://doi.org/10.1016/j.est.2025.117350

Admase, A. T., Asrade, E. D., & Fanta, S. W. (2025). A comprehensive review on energy storage materials & technologies: applications of nanofabrication techniques for enhanced performance and efficiency. *Materials for Renewable and Sustainable Energy, 14*(3), 56. doi:10.1007/s40243-025-00329-3

Ahamad, S., Ahmad, M., Mehta, B. R., & Gupta, A. (2017). Effect of nano-fillers on capacity retention and rate capability of mesocarbon microbeads anode. *Journal of The Electrochemical Society, 164*(13), A2967.

Akinyele, D. O., & Rayudu, R. K. (2014). Review of energy storage technologies for sustainable power networks. *Sustainable energy technologies and assessments, 8*, 74-91.

Algarni, M., & Ghazali, S. (2021). Comparative study of the sensitivity of PLA, ABS, PEEK, and PETG's mechanical properties to FDM printing process parameters. *Crystals, 11*(8), 995.

AlJaber, G., AlShammari, B., & AlOtaibi, B. (2025). From Theory to Experiment: Reviewing the Role of Graphene in Li-Ion Batteries Through Density Functional Theory. *Nanomaterials, 15*(13). doi:10.3390/nano15130992

Allehyani, A. (2025). Distributed energy storage systems for ancillary grid services. In *Distributed Energy Storage Systems for Digital Power Systems* (pp. 375-394): Elsevier.

Altairnano. (2025). Powerful solutions: Lithium titanate (LTO) battery technologies for transportation and grid applications.

Amir, M., Deshmukh, R. G., Khalid, H. M., Said, Z., Raza, A., Muyeen, S. M., . . . Sopian, K. (2023). Energy storage technologies: An integrated survey of developments, global economical/environmental effects, optimal scheduling model, and sustainable adaption policies. *Journal of Energy Storage, 72*, 108694. doi:https://doi.org/10.1016/j.est.2023.108694

Apostolopoulou, M., Vernardou, D., & Passerini, S. (2024). Optimization Strategies of Hybrid Lithium Titanate Oxide/Carbon Anodes for Lithium-Ion Batteries. *Nanomaterials, 14*(22). doi:10.3390/nano14221799

Apostolopoulou, M., Vernardou, D., & Passerini, S. (2024). Optimization Strategies of Hybrid Lithium Titanate Oxide/Carbon Anodes for Lithium-Ion Batteries. *Nanomaterials (Basel), 14*(22). doi:10.3390/nano14221799

Asamoah, G. A., Korsah, M., Jeyasundar, P. G., Ahmed, M., Lau, S. Y., & Danquah, M. K. (2024). Nanotechnology-Based Lithium-Ion Battery Energy Storage Systems. *Sustainability, 16*(21). doi:10.3390/su16219231

Aslam, J., Ahsan Waseem, M., Zhang, Y., & Wang, Y. (2024). Carbon-Based 3D Architectures as Anodes for Lithium-Ion Battery Systems. *ChemPlusChem, 89*(12), e202400198. doi:https://doi.org/10.1002/cplu.202400198

Audu, G. A., Mafo, A. R., Jegede, R. E., Tarasenko, M., & Kozak, K. (2025). Advances in energy storage technologies for renewable energy systems: bridging intermittency and sustainable integration. *Eurasian Journal of Physics and Functional Materials, 9*(2), 79-96.

Bashir, I., Zaghari, B., Harvey, T. J., Weddell, A. S., White, N. M., & Wang, L. (2018). Design and Testing of a Sensing System for Aero-Engine Smart Bearings. *Proceedings, 2*(13). doi:10.3390/proceedings2131005

Bayerl, D., & Kioupakis, E. (2019). Room-temperature stability of excitons and transverse-electric polarized deep-ultraviolet luminescence in atomically thin GaN quantum wells. *Applied Physics Letters, 115*(13). doi:10.1063/1.5111546

Bhutia, P. T., Grugeon, S., El Mejdoubi, A., Laruelle, S., & Marlair, G. (2024). Safety Aspects of Sodium-Ion Batteries: Prospective Analysis from First Generation Towards More Advanced Systems. *Batteries, 10*(10). doi:10.3390/batteries10100370

BIELEWSKI, M. (2022). BATTERIES FOR ENERGY STORAGE IN THE EUROPEAN UNION.

Boudeville, V., Grugeon, S., Maurel, A., Lesieur, R., Louati, M., Cayla, A., . . . Dupont, L. (2024). Solvent-free extrusion of a LiFePO4-based monofilament for three-dimensional printing of a lithium-ion battery positive electrode. *Journal of Power Sources, 593*, 233973.

Cai, W., Yan, C., Yao, Y.-X., Xu, L., Xu, R., Jiang, L.-L., . . . Zhang, Q. (2020). Rapid lithium diffusion in order@ disorder pathways for fast-charging graphite anodes. *Small Structures, 1*(1), 2000010.

Carnegie, R., Gotham, D., Nderitu, D., & Preckel, P. V. (2013). Utility scale energy storage systems. *State Utility Forecasting Group. Purdue University, 1*, 27.

Celadon, A., Sun, H., Sun, S., & Zhang, G. (2024). Batteries for electric vehicles: Technical advancements, environmental challenges, and market perspectives. *4*(5), e234. doi:https://doi.org/10.1002/sus2.234

Chacón, J. M., Caminero, M. A., García-Plaza, E., & Núñez, P. J. (2017). Additive manufacturing of PLA structures using fused deposition modelling: Effect of process parameters on mechanical properties and their optimal selection. *Materials & Design, 124*, 143-157. doi:https://doi.org/10.1016/j.matdes.2017.03.065

Chandrasekhar, J., Dhananjaya, M., Hussain, O. M., Mauger, A., & Julien, C. M. (2021). Enhanced Electrochemical Performance of Li4Ti5O12 by Niobium Doping for Pseudocapacitive Applications. *Micro, 1*(1), 28-42. doi:10.3390/micro1010004

Chekushkin, P. M., Merenkov, I. S., Smirnov, V. S., Kislenko, S. A., & Nikitina, V. A. (2021). The physical origin of the activation barrier in Li-ion intercalation processes: the overestimated role of desolvation. *Electrochimica Acta, 372*, 137843. doi:https://doi.org/10.1016/j.electacta.2021.137843

Chen, C. H., Vaughey, J. T., Jansen, A. N., Dees, D. W., Kahaian, A. J., Goacher, T., & Thackeray, M. M. (2001). Studies of Mg-Substituted Li4−xMgx Ti5O12 Spinel Electrodes (0≤x≤1) for Lithium Batteries. *Journal of The Electrochemical Society, 148*(1), A102. doi:10.1149/1.1344523

Chen, Z., Belharouak, I., Sun, Y. K., & Amine, K. (2013). Titanium-Based Anode Materials for Safe Lithium-Ion Batteries. *Advanced Functional Materials, 23*(8), 959-969. doi:https://doi.org/10.1002/adfm.201200698

Coogan, T. J., & Kazmer, D. O. (2017). Bond and part strength in fused deposition modeling. *Rapid Prototyping Journal, 23*(2), 414-422.

Cui, Y. (2021). Silicon anodes. *Nature Energy, 6*(10), 995-996. doi:10.1038/s41560-021-00918-2

Czerwiński, A., Słojewska, M., Jurczak, J., Dębowski, M., & Zygadło-Monikowska, E. (2024). FFF/FDM 3D-Printed Solid Polymer Electrolytes Based on Acrylonitrile Copolymers for Lithium-Ion Batteries. *Molecules, 29*(19). doi:10.3390/molecules29194526

Dai, Y., & Srinivasan, V. (2016). On Graded Electrode Porosity as a Design Tool for Improving the Energy Density of Batteries. *Journal of The Electrochemical Society, 163*(3), A406. doi:10.1149/2.0301603jes

De Carne, G., Maroufi, S. M., Beiranvand, H., De Angelis, V., D'Arco, S., Gevorgian, V., . . . Hagenmeyer, V. (2024). The role of energy storage systems for a secure energy supply: A comprehensive review of system needs and technology solutions. *Electric Power Systems Research, 236*, 110963. doi:https://doi.org/10.1016/j.epsr.2024.110963

de Pauli, M., Gomes, A. M. C., Cavalcante, R. L., Serpa, R. B., Reis, C. P. S., Reis, F. T., & Sartorelli, M. L. (2019). Capacitance spectra extracted from EIS by a model-free generalized phase element analysis. *Electrochimica Acta, 320*, 134366. doi:https://doi.org/10.1016/j.electacta.2019.06.059

Entwistle, J., Ge, R., Pardikar, K., Smith, R., & Cumming, D. (2022). Carbon binder domain networks and electrical conductivity in lithium-ion battery electrodes: A critical review. *Renewable and Sustainable Energy Reviews, 166*, 112624. doi:https://doi.org/10.1016/j.rser.2022.112624

Eroğlu, H., & Kurtuluş, O. (2025). Strategic design of wind energy and battery storage for efficient and sustainable energy systems. *Scientific Reports, 15*(1), 34976. doi:10.1038/s41598-025-18863-5

Feng, L., Zhou, S., Cui, H., Soomro, R. A., Zhang, P., & Xu, B. (2025). Multi-functional MXene binder enables ultra-stable and high-capacity Li4Ti5O12 anode for lithium ion batteries. *Energy Storage Materials, 75*, 104079.

Fonseca, N., Thummalapalli, S. V., Jambhulkar, S., Ravichandran, D., Zhu, Y., Patil, D., . . . Song, K. (2023). 3D Printing-Enabled Design and Manufacturing Strategies for Batteries: A Review. *Small, 19*(50), 2302718. doi:https://doi.org/10.1002/smll.202302718

Foster, C. W., Down, M. P., Zhang, Y., Ji, X., Rowley-Neale, S. J., Smith, G. C., . . . Banks, C. E. (2017). 3D printed graphene based energy storage devices. *Scientific Reports, 7*(1), 42233.

Fu, S., Jin, E., Hanayama, H., Zheng, W., Zhang, H., Di Virgilio, L., . . . Wang, H. I. (2022). Outstanding Charge Mobility by Band Transport in Two-Dimensional Semiconducting Covalent Organic Frameworks. *Journal of the American Chemical Society, 144*(16), 7489-7496. doi:10.1021/jacs.2c02408

Fu, S., Yu, X., Wu, Q., Yang, X., Liu, Z., Li, X., . . . Tong, S. (2021). Ultrathin [110]-Confined Li4Ti5O12 Nanoflakes for High Rate Lithium Storage. *Advanced Energy Materials, 11*(22), 2003270.

Gadermaier, B., Hogrefe, K., Heitjans, P., & Wilkening, H. M. R. (2021). Broadband impedance spectroscopy of Li4Ti5O12: from nearly constant loss effects to long-range ion dynamics. *Zeitschrift für anorganische und allgemeine Chemie, 647*(22), 2167-2171. doi:https://doi.org/10.1002/zaac.202100143

Gallego, N. C., Contescu, C. I., Meyer, H. M., Howe, J. Y., Meisner, R. A., Payzant, E. A., . . . Wood, D. L. (2014). Advanced surface and microstructural characterization of natural graphite anodes for lithium ion batteries. *Carbon, 72*, 393-401. doi:https://doi.org/10.1016/j.carbon.2014.02.031

Gao, X., Zheng, M., Yang, X., Sun, R., Zhang, J., & Sun, X. (2022). Emerging application of 3D-printing techniques in lithium batteries: From liquid to solid. *Materials Today, 59*, 161-181.

Gehring, J. C., & Cand, B. M. (2024). The Sustainable Energy Imperative: A Future Generations Perspective on Technologies Leading the Clean Energy Transition. *The Global Youth Council on Science, Law & Sustainability: Cambridge, UK*.

Ghafari, A., Bayat, V., Akbari, S., & Yeklangi, A. G. (2023). Current and future prospects of Li-ion batteries: A review. *NanoSci Technol, 8*, 24-43.

Ghanooni Ahmadabadi, V., Rahman, M. M., & Chen, Y. (2023). A Study on High-Rate Performance of Graphite Nanostructures Produced by Ball Milling as Anode for Lithium-Ion Batteries. *Micromachines (Basel), 14*(1). doi:10.3390/mi14010191

Ghasemian, S., Faridzad, A., Abbaszadeh, P., Taklif, A., Ghasemi, A., & Hafezi, R. (2024). An overview of global energy scenarios by 2040: identifying the driving forces using cross-impact analysis method. *International Journal of Environmental Science and Technology, 21*(11), 7749-7772.

Gu, Y.-J., Guo, Z., & Liu, H.-Q. (2014). Structure and electrochemical properties of Li4Ti5O12 with Li excess as an anode electrode material for Li-ion batteries. *Electrochimica Acta, 123*, 576-581.

Gulzar, U., Glynn, C., & O'Dwyer, C. (2020). Additive manufacturing for energy storage: Methods, designs and material selection for customizable 3D printed batteries and supercapacitors. *Current Opinion in Electrochemistry, 20*, 46-53. doi:https://doi.org/10.1016/j.coelec.2020.02.009

Han, C., He, Y.-B., Li, H., Li, B., Du, H., Qin, X., & Kang, F. (2015). Suppression of interfacial reactions between Li4Ti5O12 electrode and electrolyte solution via zinc oxide coating. *Electrochimica Acta, 157*, 266-273. doi:https://doi.org/10.1016/j.electacta.2014.12.080

Han, F., Luo, S., Wu, Z., Liang, Z., Yang, W., Han, D., . . . Niu, L. (2023). A label-free photoelectrochemical sensor based on BiVO4@graphene oxide hybrid for analysis of the antioxidant capacity in food. *Journal of Electroanalytical Chemistry, 946*, 117713. doi:https://doi.org/10.1016/j.jelechem.2023.117713

Han, X., Ouyang, M., Lu, L., & Li, J. (2014). Cycle life of commercial lithium-ion batteries with lithium titanium oxide anodes in electric vehicles. *Energies, 7*(8), 4895-4909.

Han, Y., Chandio, Z. A., Soni, H. L., Ciucci, F., & Cheong, J. Y. (2025). Carbon-derived pitch assisted surface modification of anode materials for lithium-ion batteries: Status and future perspectives. *Journal of Energy Storage, 125*, 116981. doi:https://doi.org/10.1016/j.est.2025.116981

Hasan, M. M., Haque, R., Jahirul, M. I., Rasul, M. G., Fattah, I. M. R., Hassan, N. M. S., & Mofijur, M. (2025). Advancing energy storage: The future trajectory of lithium-ion battery technologies. *Journal of Energy Storage, 120*, 116511. doi:https://doi.org/10.1016/j.est.2025.116511

He, W., Chen, C., Jiang, J., Chen, Z., Liao, H., Dou, H., & Zhang, X. (2022). 3D Printed Multilayer Graphite@ SiO Structural Anode for High-Loading Lithium-Ion Battery. *Batteries & Supercaps, 5*(3), e202100258.

Heath, G. A., Ravikumar, D., Hansen, B., & Kupets, E. (2022). A critical review of the circular economy for lithium-ion batteries and photovoltaic modules–status, challenges, and opportunities. *Journal of the Air & Waste Management Association, 72*(6), 478-539.

Hesse, H. C., Schimpe, M., Kucevic, D., & Jossen, A. (2017). Lithium-Ion Battery Storage for the Grid—A Review of Stationary Battery Storage System Design Tailored for Applications in Modern Power Grids. *Energies, 10*(12). doi:10.3390/en10122107

Hopewell, J., Dvorak, R., & Kosior, E. (2009). Plastics recycling: challenges and opportunities. *Philosophical Transactions of the Royal Society B: Biological Sciences, 364*(1526), 2115-2126. doi:10.1098/rstb.2008.0311

Iqbal, M. S., Stano, G., Triminì, V., & Percoco, G. (2024). Low-cost method to reduce interlayer voids in material extrusion: in situ layer-by-layer solvent treatment. *The International Journal of Advanced Manufacturing Technology, 133*(11), 5333-5342. doi:10.1007/s00170-024-14077-7

Islam, M. M., Yu, T., Giannoccaro, G., Mi, Y., La Scala, M., Nasab, M. R., & Wang, J. (2024). Improving reliability and stability of the power systems: A comprehensive review on the role of energy storage systems to enhance flexibility. *IEEE Access, 12*, 152738-152765.

Jang, J., & Kwon, T. (2025). Various Technologies to Mitigate Volume Expansion of Silicon Anode Materials in Lithium-Ion Batteries. *Batteries, 11*(9). doi:10.3390/batteries11090346

Jiang, X., Ma, G., Zhu, Q., Ge, H., Chen, Q., Yan, B., . . . Wu, C. (2023). Synthesis of dual-modified Fe-doped and carbon-coated Li4Ti5O12 anode based on industrial H2TiO3 for Li-ion batteries. *Scientific Reports, 13*(1), 15118. doi:10.1038/s41598-023-41830-x

Joy, R., Balakrishnan, N. T. M., Das, A., Shafeek, S., Thakur, V. K., Zaghib, K., . . . Raghavan, P. (2022). Graphene: chemistry and applications for lithium-ion batteries. *Electrochem, 3*(1), 143-183.

Julien, C. M., & Mauger, A. (2024). Fabrication of Li4Ti5O12 (LTO) as Anode Material for Li-Ion Batteries. *Micromachines, 15*(3). doi:10.3390/mi15030310

Julien, C. M., & Mauger, A. (2024). Fabrication of Li(4)Ti(5)O(12) (LTO) as Anode Material for Li-Ion Batteries. *Micromachines (Basel), 15*(3). doi:10.3390/mi15030310

Jung, S.-K., Dutta, J., Martha, S. K., Jun, M. B.-G., & Pol, V. G. (2025). Powering the extreme: rising world of batteries that could operate at ultra-low temperatures. *Chemical Communications, 61*(58), 10716-10730. doi:https://doi.org/10.1039/d5cc02279g

Kamyab, N., Weidner, J. W., & White, R. E. (2019). Mixed Mode Growth Model for the Solid Electrolyte Interface (SEI). *Journal of The Electrochemical Society, 166*(2), A334. doi:10.1149/2.1101902jes

Kang, C.-Y., Krajewski, M., & Lin, J.-Y. (2021). Impact of titanium precursors on formation and electrochemical properties of Li4Ti5O12 anode materials for lithium-ion batteries. *Journal of Solid State Electrochemistry, 25*(2), 575-582. doi:10.1007/s10008-020-04831-8

Kazemi, A., Mostaani, R., Ravari, M. K., Ghorbanzadeh, M., Yavarinasab, M., Enferadi, J., . . . Davoodi, A. (2025a). Enhancing high rate performance of Lithium Titanium Oxide (LTO) anodes: A comprehensive review. *Journal of Power Sources, 630*, 236051. doi:https://doi.org/10.1016/j.jpowsour.2024.236051

Kazemi, A., Mostaani, R., Ravari, M. K., Ghorbanzadeh, M., Yavarinasab, M., Enferadi, J., . . . Davoodi, A. J. J. o. P. S. (2025b). Enhancing high rate performance of Lithium Titanium Oxide (LTO) anodes: A comprehensive review.

Khan, I., Tariq, M., Abas, M., Shakeel, M., Hira, F., Al Rashid, A., & Koç, M. (2023). Parametric investigation and optimisation of mechanical properties of thick tri-material based composite of PLA-PETG-ABS 3D-printed using fused filament fabrication. *Composites Part C: Open Access, 12*, 100392.

Kia, A. M., Speulmanns, J., Emara, J., Potapov, P., Lubk, A., & Haufe, N. (2023). X-ray photoelectron spectroscopic investigation of atomic-layer-deposited spinel Li4Ti5O12: Calcination under reducing atmosphere. *Thin Solid Films, 768*, 139694. doi:https://doi.org/10.1016/j.tsf.2023.139694

Kim, Y.-M., & Shim, J.-H. (2020). Development of Fast-Rechargeable Lithium Ion Batteries By Graphite Etched with Potassium Hydroxide. *ECS Meeting Abstracts, MA2020-02*(3), 584. doi:10.1149/MA2020-023584mtgabs

Kioupakis, E., Chae, S., Bushick, K., Pant, N., Zhang, X., & Lee, W. (2021). Theoretical characterization and computational discovery of ultra-wide-band-gap semiconductors with predictive atomistic calculations. *Journal of Materials Research, 36*(23), 4616-4637. doi:10.1557/s43578-021-00437-6

Kitta, M., Matsuda, T., Maeda, Y., Akita, T., Tanaka, S., Kido, Y., & Kohyama, M. (2014). Atomistic structure of a spinel Li4Ti5O12(111) surface elucidated by scanning tunneling microscopy and medium energy ion scattering spectrometry. *Surface Science, 619*, 5-9. doi:https://doi.org/10.1016/j.susc.2013.09.026

Ko, M., Chae, S., & Cho, J. (2015). Challenges in Accommodating Volume Change of Si Anodes for Li-Ion Batteries. *2*(11), 1645-1651. doi:https://doi.org/10.1002/celc.201500254

Koech, A. K., Mwandila, G., Mulolani, F., & Mwaanga, P. (2025). Exploring the anode materials for lithium-ion batteries: A review. *Next Research, 2*(3), 100442. doi:https://doi.org/10.1016/j.nexres.2025.100442

Kozlova, A., Uvarov, N., & Ulihin, A. (2022). Transport and Electrochemical Properties of Li4Ti5O12-Li2TiO3 and Li4Ti5O12-TiO2 Composites. *Materials, 15*(17). doi:10.3390/ma15176079

Lalehpour, A., Janeteas, C., & Barari, A. (2018). Surface roughness of FDM parts after post-processing with acetone vapor bath smoothing process. *The International Journal of Advanced Manufacturing Technology, 95*(1), 1505-1520.

Lee, C.-Y., Peng, H.-C., Lee, S.-J., Hung, I. M., Hsieh, C.-T., Chiou, C.-S., . . . Huang, Y.-P. (2015). A flexible three-in-one microsensor for real-time monitoring of internal temperature, voltage and current of lithium batteries. *Sensors, 15*(5), 11485-11498.

Lee, J.-S., Yun, S.-D., Nyamaa, O., Yang, J.-H., Huh, S.-C., Jeong, H.-M., . . . Noh, J.-P. (2022). Free-Standing Li4Ti5O12/Carbon Nanotube Electrodes for Flexible Lithium-Ion Batteries. *Energies, 15*(22). doi:10.3390/en15228585

Li, H., He, Z., Tian, S., Liu, S., Shi, X., Xia, Y., & Hou, H. (2023). Optimization prelithiation current of silicon-oxygen anode for high specific energy li-ion cells. *Journal of Energy Storage, 64*, 107149. doi:https://doi.org/10.1016/j.est.2023.107149

Li, K., Niu, J., Hao, Y., Yao, J., Kumar, P., Luo, Z., . . . Ming, H. (2025). Analysis of failure mechanisms and behavior of LiCoO2-graphite batteries at 0 °C. *Next Materials, 8*, 100709. doi:https://doi.org/10.1016/j.nxmate.2025.100709

Liu, H., Zhu, Z., Huang, J., He, X., Chen, Y., Zhang, R., . . . Xing, X. (2019). Elucidating the limit of Li insertion into the spinel Li4Ti5O12. *ACS Materials Letters, 1*(1), 96-102.

Liu, J., Zhong, S., Chen, Q., Meng, L., Wang, Q., Liao, Z., & Zhou, J. (2020). Spherical Li4Ti5O12/NiO composite with enhanced capacity and rate performance as anode material for lithium-ion batteries. *Frontiers in Chemistry, 8*, 626388.

Liu, X., Yin, L., Ren, D., Wang, L., Ren, Y., Xu, W., . . . Amine, K. (2021). In situ observation of thermal-driven degradation and safety concerns of lithiated graphite anode. *Nature Communications, 12*(1), 4235. doi:10.1038/s41467-021-24404-1

Liu, Y., Ding, H., Chen, H., Gao, H., Yu, J., Mo, F., & Wang, N. (2025). Recent Progress on the Research of 3D Printing in Aqueous Zinc-Ion Batteries. *Polymers, 17*(15). doi:10.3390/polym17152136

Llaín-Jiménez, H. A., Buchberger, D. A., Winkowska-Struzik, M., Ratyński, M., Krajewski, M., Boczar, M., . . . Czerwiński, A. (2022). Correlation between Lithium Titanium Oxide Powder Morphology and High Rate Performance in Lithium-Ion Batteries. *Batteries, 8*(10). doi:10.3390/batteries8100168

Lou, F., & Chen, D. (2015). Aligned carbon nanostructures based 3D electrodes for energy storage. *Journal of Energy Chemistry, 24*(5), 559-586. doi:https://doi.org/10.1016/j.jechem.2015.08.013

Lupan, O., Magariu, N., Santos-Carballal, D., Ababii, N., Offermann, J., Pooker, P., . . . Adelung, R. (2023). Development of 2-in-1 sensors for the safety assessment of lithium-ion batteries via early detection of vapors produced by electrolyte solvents. *ACS applied materials & interfaces, 15*(22), 27340-27356.

Ma, J., Zheng, S., Fu, Y., Wang, X., Qin, J., & Wu, Z.-S. (2024). The status and challenging perspectives of 3D-printed micro-batteries. *Chemical Science, 15*(15), 5451-5481.

Ma, Y., Ding, B., Ji, G., & Lee, J. Y. (2013). Carbon-Encapsulated F-Doped Li4Ti5O12 as a High Rate Anode Material for Li+ Batteries. *ACS Nano, 7*(12), 10870-10878. doi:10.1021/nn404311x

Madani, S. S., Shabeer, Y., Allard, F., Fowler, M., Ziebert, C., Wang, Z., . . . Khalilpour, K. (2025). A Comprehensive Review on Lithium-Ion Battery Lifetime Prediction and Aging Mechanism Analysis. *Batteries, 11*(4). doi:10.3390/batteries11040127

Mahek, M. K., Ramadan, M., Choi, D. S., Ghazal, M., Alkhedher, M., & Alami, A. H. (2025). Lithium titanate batteries for sustainable energy storage: A comprehensive review of safety, performance, and environmental impact. *Journal of Energy Storage, 132*, 117573. doi:https://doi.org/10.1016/j.est.2025.117573

Mao, S., Huang, X., Chang, J., Cui, S., Zhou, G., & Chen, J. (2015). One-step, continuous synthesis of a spherical Li4Ti5O12/graphene composite as an ultra-long cycle life lithium-ion battery anode. *NPG Asia Materials, 7*(11), e224-e224. doi:10.1038/am.2015.120

Market.Us. (2025). lobal Energy Storage Systems Market By Technology (Electrochemical, Mechanical, Thermal, Others), By Application (Utility, Commercial & Industrial, Residential), By Region and Companies – Industry Segment Outlook, Market Assessment, Competition Scenario, Trends, and Forecast 2025–2034.

Markey, B., Zhang, M., Robb, I., Xu, P., Gao, H., Zhang, D., . . . Chen, Z. (2020). Effective Upcycling of Graphite Anode: Healing and Doping Enabled Direct Regeneration. *Journal of The Electrochemical Society, 167*(16), 160511. doi:10.1149/1945-7111/abcc2f

Maurel, A., Grugeon, S., Fleutot, B., Courty, M., Prashantha, K., Tortajada, H., . . . Dupont, L. (2019). Three-dimensional printing of a LiFePO4/graphite battery cell via fused deposition modeling. *Scientific Reports, 9*(1), 18031.

Maurel, A., Pavone, A., Stano, G., Martinez, A. C., MacDonald, E., & Percoco, G. (2023). Manufacturing-oriented review on 3D printed lithium-ion batteries fabricated using material

extrusion. *Virtual and Physical Prototyping, 18*(1), e2264281. doi:10.1080/17452759.2023.2264281

Mayyas, A., Chadly, A., Amer, S. T., & Azar, E. (2022). Economics of the Li-ion batteries and reversible fuel cells as energy storage systems when coupled with dynamic electricity pricing schemes. *Energy, 239*, 121941.

Menyhart, J. (2024). Overview of sustainable mobility: the role of electric vehicles in energy communities. *World Electric Vehicle Journal, 15*(6), 275.

Microvast Holdings, I. (2024). Microvast powers the next generation of electric commercial vehicles with groundbreaking battery technology at IAA Transportation 2024.

Mojumder, M. R., Ahmed Antara, F., Hasanuzzaman, M., Alamri, B., & Alsharef, M. (2022). Electric Vehicle-to-Grid (V2G) Technologies: Impact on the Power Grid and Battery. *Sustainability, 14*(21). doi:10.3390/su142113856

Mottaghi, M., & Pearce, J. M. (2024). A Review of 3D Printing Batteries. *Batteries, 10*(3). doi:10.3390/batteries10030110

Murugan, M., Elumalai, P. V., Vijayakumar, K. C. K., Babu, M., Suresh Kumar, K., Ganesh, M., . . . Prabhakar, S. (2025). A Comprehensive Review of Thermal Management Methods and Ideal System Design for Improved Electric Vehicle Battery Pack Performance and Safety. *Energy Science & Engineering, 13*(3), 1011-1036. doi:https://doi.org/10.1002/ese3.2081

Nandihalli, N. (2024). A Review of Nanocarbon-Based Anode Materials for Lithium-Ion Batteries. *Crystals, 14*(9). doi:10.3390/cryst14090800

Ngoy, K. R., Lukong, V. T., Yoro, K. O., Makambo, J. B., Chukwuati, N. C., Ibegbulam, C., . . . Jen, T.-C. (2025). Lithium-ion batteries and the future of sustainable energy: A comprehensive review. *Renewable and Sustainable Energy Reviews, 223*, 115971. doi:https://doi.org/10.1016/j.rser.2025.115971

Njema, G. G., Ouma, R. B. O., & Kibet, J. K. (2024). A review on the recent advances in battery development and energy storage technologies. *Journal of renewable energy, 2024*(1), 2329261.

Otero, M., Heim, C., Leiva, E. P. M., Wagner, N., & Friedrich, A. (2018). Design-Considerations regarding Silicon/Graphite and Tin/Graphite Composite Electrodes for Lithium-Ion Batteries. *Scientific Reports, 8*(1), 15851. doi:10.1038/s41598-018-33405-y

Paraschiv, L. S., Paraschiv, S., & Alexandru, S. J. M. o. E. Q. A. I. J. (2025). Decarbonizing Europe's energy system through the phase-out of coal-fired power plants under the green deal initiatives for sustainable development. 1-21.

Parvizi, P., Jalilian, M., Amidi, A. M., Zangeneh, M. R., & Riba, J.-R. (2025). From Present Innovations to Future Potential: The Promising Journey of Lithium-Ion Batteries. *Micromachines, 16*(2). doi:10.3390/mi16020194

Pavlovskii, A. A., Pushnitsa, K., Kosenko, A., Novikov, P., & Popovich, A. A. (2024). 3D-Printed Lithium-Ion Battery Electrodes: A Brief Review of Three Key Fabrication Techniques. *Materials (Basel), 17*(23). doi:10.3390/ma17235904

Pavlovskii, A. A., Pushnitsa, K., Kosenko, A., Novikov, P., & Popovich, A. A. (2024). 3D-Printed Lithium-Ion Battery Electrodes: A Brief Review of Three Key Fabrication Techniques. *Materials, 17*(23). doi:10.3390/ma17235904

Peng, M., Shin, K., Jiang, L., Jin, Y., Zeng, K., Zhou, X., & Tang, Y. (2022). Alloy-Type Anodes for High-Performance Rechargeable Batteries. *61*(33), e202206770. doi:https://doi.org/10.1002/anie.202206770

Pestano, V., Oliveira, M. P. d., & Silva, F. P. d. (2022). Effect of acetone vapor smoothing process on surface finish and geometric accuracy of fused deposition modeling ABS parts. *Journal of Materials Science and Chemical Engineering. China. Vol. 10, no. 10 (oct. 2022), p. 1-9.*

Pomerantseva, E., Jung, H., Gnerlich, M., Baron, S., Gerasopoulos, K., & Ghodssi, R. (2013). A MEMS platform for in situ, real-time monitoring of electrochemically induced mechanical changes in lithium-ion battery electrodes. *Journal of micromechanics and microengineering, 23*(11), 114018.

Ragones, H., Menkin, S., Kamir, Y., Gladkikh, A., Mukra, T., Kosa, G., & Golodnitsky, D. (2018). Towards smart free form-factor 3D printable batteries. *Sustainable Energy & Fuels, 2*(7), 1542-1549.

Rahman, M. M., Nisar, U., Abouimrane, A., Belharouak, I., & Amin, R. (2025). Valuation of Anode Materials for High-Performance Lithium Batteries: From Graphite to Lithium Metal and Beyond. *Electrochemical Energy Reviews, 8*(1), 14. doi:10.1007/s41918-025-00249-w

Reyes, C., Somogyi, R., Niu, S., Cruz, M. A., Yang, F., Catenacci, M. J., . . . Wiley, B. J. (2018). Three-dimensional printing of a complete lithium ion battery with fused filament fabrication. *ACS Applied Energy Materials, 1*(10), 5268-5279.

Rubio, J. C., & Bolduc, M. (2025). Inkjet Printing for Batteries and Supercapacitors: State-of-the-Art Developments and Outlook. *Energies, 18*(20). doi:10.3390/en18205348

Saha, S., Das, S., & Rahman, M. Z. (2026). Hybridization in natural fiber composites: Enhanced performance and sustainability. *Composites Part B: Engineering, 308*, 112986. doi:https://doi.org/10.1016/j.compositesb.2025.112986

Saleh, M. S., Li, J., Park, J., & Panat, R. (2018). 3D printed hierarchically-porous microlattice electrode materials for exceptionally high specific capacity and areal capacity lithium ion batteries. *Additive Manufacturing, 23*, 70-78. doi:https://doi.org/10.1016/j.addma.2018.07.006

Sang, V. T., Duong, Q. H., Zhou, L., & Arranz, C. F. A. (2024). Electric Vehicle Battery Technologies and Capacity Prediction: A Comprehensive Literature Review of Trends and Influencing Factors. *Batteries, 10*(12). doi:10.3390/batteries10120451

Schichtel, B. A., Stevenson, E. D., Braun, G., Shaw, S. L., Tarroja, B., & Chao, C. C. (2022). Circular economy for lithium-ion batteries and photovoltaic modules—status, challenges, and opportunities. *Journal of the Air & Waste Management Association, 72*(10), 1053-1062.

Schleife, A., Neumann, M. D., Esser, N., Galazka, Z., Gottwald, A., Nixdorf, J., . . . Feneberg, M. (2018). Optical properties of In2O3 from experiment and first-principles theory: influence of lattice screening. *New Journal of Physics, 20*(5), 053016. doi:10.1088/1367-2630/aabeb0

Selvamurugan, M., Karthikeyan, C., & Karuppuchamy, S. (2017). SYNTHESIS AND CHARACTERIZATION OF LITHIUM TITANATE (LTO) NANOCOMPOSITES VIA SOLUTION GROWTH ROUTE FOR Li-ION BATTERIES. *Kongunadu Research Journal, 4*(3), 10-13.

Shaju, A., Ummer, R. P., Thomas, S., & Kandasubramanian, B. (2025). Novel Approaches in 3D Printing Techniques for the Development of High-Performance Micro-Batteries. *Journal of Electronic Materials, 54*(3), 1531-1552. doi:10.1007/s11664-024-11659-9

Shanmugam, V., Das, O., Babu, K., Marimuthu, U., Veerasimman, A., Johnson, D. J., . . . Berto, F. (2021). Fatigue behaviour of FDM-3D printed polymers, polymeric composites and architected cellular materials. *International Journal of Fatigue, 143*, 106007. doi:https://doi.org/10.1016/j.ijfatigue.2020.106007

Shen, L., Uchaker, E., Zhang, X., & Cao, G. (2012). Hydrogenated Li4Ti5O12 nanowire arrays for high rate lithium ion batteries. *Advanced materials, 24*(48), 6502-6506.

Simpson, F., Redor, S., Titirici, M. M., & Lander, L. (2025). A Review on the Energy Storage Mechanisms of Transition Metal Sulfide and Selenide Cathode Materials for Non-Aqueous Aluminum Batteries. *Advanced Energy Materials*, e03159.

Son, J.-h., Kim, H., Choi, Y., & Lee, H. (2024). 3D printed energy devices: generation, conversion, and storage. *Microsystems & Nanoengineering, 10*(1), 93. doi:10.1038/s41378-024-00708-2

Song, J., Shang, W., Zhou, W., Li, J., Wu, X., Li, W., . . . Liu, S. (2025). From issues to solutions: 3D printing for overcoming challenges in liquid- and solid-state batteries. *Energy Storage Materials, 79*, 104342. doi:https://doi.org/10.1016/j.ensm.2025.104342

Stolz, L., Winter, M., & Kasnatscheew, J. (2024). Practical relevance of charge transfer resistance at the Li metal electrode| electrolyte interface in batteries? *Journal of Solid State Electrochemistry*, 1-6.

Sturman, J., Zhang, Y., Yim, C.-H., Niketic, S., Toupin, M., Baranova, E. A., & Abu-Lebdeh, Y. (2021). Composites of silicon@$Li_4Ti_5O_{12}$ and graphite for high-capacity lithium-ion battery anode materials

Composites of silicon@Li4Ti5O12 and graphite for high-capacity lithium-ion battery anode materials. *Journal of The Electrochemical Society, 168*(1), 010524-010528. doi:10.1149/1945-7111/abda05

Sun, K., Wei, T. S., Ahn, B. Y., Seo, J. Y., Dillon, S. J., & Lewis, J. A. (2013). 3D printing of interdigitated Li-Ion microbattery architectures. *Advanced materials, 25*(33), 4539-4543.

Sun, L., Kong, W., Wu, H., Wu, Y., Wang, D., Zhao, F., . . . Fan, S. (2016). Mesoporous Li4Ti5O12 nanoclusters anchored on super-aligned carbon nanotubes as high performance electrodes for lithium ion batteries. *Nanoscale, 8*(1), 617-625. doi:10.1039/C5NR06406F

Sun, L., Li, H., Dong, Y., Rong, W., Zhou, N., Dang, R., . . . Pan, C. (2025). Carbon/High-Entropy Alloy Nanocomposites: Synergistic Innovations and Breakthrough Challenges for Electrochemical Energy Storage. *Batteries, 11*(9). doi:10.3390/batteries11090317

Sztymela, K., Bienia, M., Rossignol, F., Mailley, S., Ziesche, S., Varghese, J., & Cerbelaud, M. (2022). Fabrication of modern lithium ion batteries by 3D inkjet printing: opportunities and challenges. *Heliyon, 8*(12), e12623. doi:https://doi.org/10.1016/j.heliyon.2022.e12623

Thermtest. (2024). he Role of Batteries in Renewable Energy Solutions. Thermtest.

Tomaszewska, A., Chu, Z., Feng, X., O'Kane, S., Liu, X., Chen, J., . . . Wu, B. (2019). Lithium-ion battery fast charging: A review. *eTransportation, 1*, 100011. doi:https://doi.org/10.1016/j.etran.2019.100011

Tomboc, G. M., Wang, Y., Wang, H., Li, J., & Lee, K. (2021). Sn-based metal oxides and sulfides anode materials for Na ion battery. *Energy Storage Materials, 39*, 21-44. doi:https://doi.org/10.1016/j.ensm.2021.04.009

Torrado, A. R., & Roberson, D. A. (2016). Failure Analysis and Anisotropy Evaluation of 3D-Printed Tensile Test Specimens of Different Geometries and Print Raster Patterns. *Journal of Failure Analysis and Prevention, 16*(1), 154-164. doi:10.1007/s11668-016-0067-4

Torres, J., Abo, E., & Sugar, A. J. (2023). Effects of annealing and acetone vapor smoothing on the tensile properties and surface roughness of FDM printed ABS components. *Rapid Prototyping Journal, 29*(5), 921-934.

Tsai, P.-c., Hsu, W.-D., & Lin, S.-k. (2014). Atomistic Structure and Ab Initio Electrochemical Properties of Li4Ti5O12 Defect Spinel for Li Ion Batteries. *Journal of The Electrochemical Society, 161*(3), A439. doi:10.1149/2.095403jes

Tymrak, B. M., Kreiger, M., & Pearce, J. M. (2014). Mechanical properties of components fabricated with open-source 3-D printers under realistic environmental conditions. *Materials & Design, 58*, 242-246. doi:https://doi.org/10.1016/j.matdes.2014.02.038

Vandaele, N., & Porter, W. (2015). Renewable energy in developing and developed nations: Outlooks to 2040. *Journal of Undergraduate Research, 15*(3), 1-7.

Varley, J. B., & Schleife, A. (2015). Bethe–Salpeter calculation of optical-absorption spectra of In2O3 and Ga2O3. *Semiconductor Science and Technology, 30*(2), 024010. doi:10.1088/0268-1242/30/2/024010

Vidakis, N., Petousis, M., Velidakis, E., Liebscher, M., Mechtcherine, V., & Tzounis, L. (2020). On the strain rate sensitivity of fused filament fabrication (Fff) processed pla, abs, petg, pa6, and pp thermoplastic polymers. *Polymers, 12*(12), 2924.

Wagner-Henke, J., Kuai, D., Gerasimov, M., Röder, F., Balbuena, P. B., & Krewer, U. (2023). Knowledge-driven design of solid-electrolyte interphases on lithium metal via multiscale modelling. *Nature Communications, 14*(1), 6823. doi:10.1038/s41467-023-42212-7

Waldmann, T., Hogg, B.-I., Kasper, M., Grolleau, S., Couceiro, C. G., Trad, K., . . . Wohlfahrt-Mehrens, M. (2016). Interplay of operational parameters on lithium deposition in lithium-ion cells: systematic measurements with reconstructed 3-electrode pouch full cells. *Journal of The Electrochemical Society, 163*(7), A1232.

Wang, Y., Song, J., Huang, G., Lang, X., & Zhang, S. (2023). Hybrid nanostructure of sanwhich-like porous Co3O4 nanorods/exfoliate graphite composite for lithium-ion batteries. *Journal of Energy Storage, 72*, 108575. doi:https://doi.org/10.1016/j.est.2023.108575

Wang, Y., Zhang, S., Hua, H., Fu, D., Wang, X., Zhang, Z., . . . Chen, S. (2025). Recent Advances in the Failure Analysis of Solid-State Li Ion Batteries. *Renewables, 3*(4), 175-202.

Wang, Y., & Zhu, W. (2020). Micro/nano-structured Li4Ti5O12 as high rate anode material for lithium ion batteries. *Solid State Ionics, 349*, 115297. doi:https://doi.org/10.1016/j.ssi.2020.115297

Wei, K., Zhou, L., Wang, S., Wei, J., Yan, D., Cheng, Y., & Yu, Z. (2021). Watermelon-like texture lithium titanate and silicon composite films as anodes for lithium-ion battery with high capacity and long cycle life. *Journal of Alloys and Compounds, 885*, 160994. doi:https://doi.org/10.1016/j.jallcom.2021.160994

Yan, J., Huang, S., Lim, Y. V., Xu, T., Kong, D., Li, X., . . . Wang, Y. (2022). Direct-ink writing 3D printed energy storage devices: From material selectivity, design and optimization strategies to diverse applications. *Materials Today, 54*, 110-152. doi:https://doi.org/10.1016/j.mattod.2022.03.014

Yan, Z., Sun, T., Li, W., Long, Z., Zhang, R., Wang, K., . . . Qiao, H. (2025). Advances in Metal Sulfides Anode for High-Performance Sodium-Ion Batteries. *CrystEngComm*.

Yang, X., Zhan, C., Ren, X., Wang, C., Wei, L., Yu, Q., . . . Huang, Z.-H. (2021). Nitrogen-doped hollow graphite granule as anode materials for high-performance lithium-ion batteries. *Journal of Solid State Chemistry, 303*, 122500. doi:https://doi.org/10.1016/j.jssc.2021.122500

Yi, T.-F., Xie, Y., Wu, Q., Liu, H., Jiang, L., Ye, M., & Zhu, R. (2012). High rate cycling performance of lanthanum-modified Li4Ti5O12 anode materials for lithium-ion batteries. *Journal of Power Sources, 214*, 220-226. doi:https://doi.org/10.1016/j.jpowsour.2012.04.101

Yi, T.-F., Yang, S.-Y., & Xie, Y. (2015). Recent advances of Li4Ti5O12 as a promising next generation anode material for high power lithium-ion batteries. *Journal of Materials Chemistry A, 3*(11), 5750-5777. doi:10.1039/C4TA06882C

Yu, H., Chen, X., Zhou, J., Wang, H., & Qiu, S. (2023). Premium defect-enriched graphite from spent anodes of lithium ion batteries. *Journal of Alloys and Compounds, 960*, 170876. doi:https://doi.org/10.1016/j.jallcom.2023.170876

Yu, Y., Zhu, J., Zhang, J., & Jiang, M. (2026). Bridging conductivity and stability: challenges and progress in organic ionic-electronic conductors for overcoming Si anodes degradation in high-energy lithium-ion batteries. *Progress in Materials Science, 156*, 101546. doi:https://doi.org/10.1016/j.pmatsci.2025.101546

Zacharias, M., & Giustino, F. (2016). One-shot calculation of temperature-dependent optical spectra and phonon-induced band-gap renormalization. *Physical Review B, 94*(7), 075125.

Zare, Y., Naqvi, M., Rhee, K. Y., & Park, S.-J. (2025). Simulation of electrical conductivity for polymer carbon nanofiber composites assuming an extended nanofiber by interphase depth and tunneling distance. *Scientific Reports, 15*(1), 31623. doi:10.1038/s41598-025-17613-x

Zhang, B., Liu, Y., Huang, Z., Oh, S., Yu, Y., Mai, Y.-W., & Kim, J.-K. (2012). Urchin-like Li4Ti5O12–carbon nanofiber composites for high rate performance anodes in Li-ion batteries. *Journal of Materials Chemistry, 22*(24), 12133-12140. doi:10.1039/C2JM31308A

Zhang, K., Li, D., Wang, X., Gao, J., Shen, H., Zhang, H., . . . Chen, Z. (2024). Dry Electrode Processing Technology and Binders. *Materials, 17*(10). doi:10.3390/ma17102349

Zhang, Q., Soham, D., Liang, Z., & Wan, J. (2025). Advances in wearable energy storage and harvesting systems. *Med-X, 3*(1), 3. doi:10.1007/s44258-024-00048-w

Zhang, S., Cao, X. Y., Ma, Y. M., Ke, Y. C., Zhang, J. K., & Wang, F. S. (2011). The effects of particle size and content on the thermal conductivity and mechanical properties of Al2O3/high density polyethylene (HDPE) composites. *Express Polymer Letters, 5*, 581-590. doi:10.3144/expresspolymlett.2011.57

Zhang, X., Lu, W., Zhou, G., & Li, Q. (2020). Understanding the Mechanical and Conductive Properties of Carbon Nanotube Fibers for Smart Electronics. *32*(5), 1902028. doi:https://doi.org/10.1002/adma.201902028

Zhang, Z., Deng, X., Sunarso, J., Cai, R., Chu, S., Miao, J., . . . Shao, Z. (2017). Two-Step Fabrication of Li4Ti5O12-Coated Carbon Nanofibers as a Flexible Film Electrode for High-Power Lithium-Ion Batteries. *ChemElectroChem, 4*(9), 2286-2292. doi:https://doi.org/10.1002/celc.201700351

Zhao, W., Zhao, C., Wu, H., Li, L., & Zhang, C. (2024). Progress, challenge and perspective of graphite-based anode materials for lithium batteries: A review. *Journal of Energy Storage, 81*, 110409. doi:https://doi.org/10.1016/j.est.2023.110409

Zhao, Y., Liu, G., Liu, L., & Jiang, Z. (2009). High-performance thin-film Li4Ti5O12 electrodes fabricated by using ink-jet printing technique and their electrochemical properties. *Journal of Solid State Electrochemistry, 13*(5), 705-711. doi:10.1007/s10008-008-0575-6

Zhong, C., Weng, S., Wang, Z., Zhan, C., & Wang, X. (2023). Kinetic limits and enhancement of graphite anode for fast-charging lithium-ion batteries. *Nano Energy, 117*, 108894. doi:https://doi.org/10.1016/j.nanoen.2023.108894

Zhou, X., Xu, Y., Chen, Y., & Tian, F. (2025). Mechanism on lattice thermal conductivity of carbon-vacancy and porous medium entropy ceramics. *Scripta Materialia, 259*, 116568. doi:https://doi.org/10.1016/j.scriptamat.2025.116568

Zhu, M., & Vesely, D. (2007). The effect of polymer swelling and resistance to flow on solvent diffusion and permeability. *European Polymer Journal, 43*(10), 4503-4515. doi:https://doi.org/10.1016/j.eurpolymj.2007.07.012

Ziemian, C., Sharma, M., & Ziemian, S. (2012). Anisotropic mechanical properties of ABS parts fabricated by fused deposition modelling. *Mechanical engineering, 23*, 159-180.

Abbreviations

LIBs	Lithium ion batteries
V2G	Vehicle-to-grid
LTO	Lithium titanate oxide
ESS	Energy storage systems
IEA	International Energy Agency
EVs	Electric vehicles
BESS	Battery energy storage systems
NMC	Nickel-manganese-cobalt
LFP	Lithium Iron Phosphate
SOC	State-of-charge
C-rate	Charging rate
SEI	Solid electrolyte interphase
DFT	Density functional theory
D_{li}	Lithium-ion diffusion coefficient
ΔH	Enthalpy of lithiation
DSC	Differential scanning calorimetry
ΔG_decomp	Gibbs free energy of decomposition
EIS	Electrochemical impedance spectroscopy
NCL	Near-constant loss
CVD	Chemical vapor deposition
CNTs	Carbon nanotubes

ESS	Energy storage systems
LCOS	Levelized cost of storage
CAD	Computer-aided design
DIW	Direct Ink Writing
IJP	Inkjet Printing
FFF	Fused Filament Fabrication
SLA	Stereolithography
ABS	Acrylonitrile butadiene styrene
EA	Ethyl acetate
RM	Room temperature
H_2SO_4	Sulfuric acid
H_3PO_4	Phosphoric acid
DCM	Dichloromethane
Tg	Glass transition Temperature
KMnO4	potassium permanganate

Supporting Video Document

The supporting videos associated with this thesis are available online through the links provided below. For reviewers or readers who are unable to access the online material, the video files can be made available upon reasonable request.

1. Flow of the composite material.mp4
2. 3D Printing of LTO based composite material.mp4

Another video (3) highlights that, during the 3D printing of ceramic-based materials, challenges such as incomplete material deposition and missing printed regions can occur. These issues are common in ceramic additive manufacturing and represent important aspects that should be addressed in future optimization studies.

3. Pellet 3D printer (Anode).mp4

Abstract (English)

Additive manufacturing (AM) offers unprecedented design flexibility for electrochemical energy storage systems, enabling customized architectures and direct integration of functional materials into structural components. However, the application of AM to lithium-ion batteries remains in its infancy, primarily constrained by material compatibility and processing challenges. This research addresses these limitations by developing and electrochemically characterizing 3D-printed composite electrodes based on LTO, CNFs, and PLA as the polymeric matrix, with the inclusion of a biodegradable plasticizer to tailor rheological performance for extrusion-based printing. A printable feedstock containing 52 wt.% LTO was formulated through systematic rheological optimization. Blends of PLA, plasticizer, and LTO were tuned to achieve extrusion-grade viscosities in the range of 10^3–10^4 Pa·s at 180 °C, ensuring both filament continuity and layer adhesion during material extrusion. Conductivity measurements performed on composite discs containing 4, 8, and 12 wt.% CNF revealed a percolation threshold near 8 wt.%, where electronic conductivity sharply increased to ~10^{-1} S cm^{-1} without compromising filament strength or printability. These results demonstrate that a balanced CNF content can simultaneously optimize electronic transport and mechanical integrity—an essential requirement for 3D printable energy storage materials. Disk-shaped electrodes (15–18 mm diameter, 0.5 mm thickness) were printed directly from the optimized filament using a custom-designed extrusion printer and assembled into half cells versus lithium metal. Galvanostatic cycling at C/25 exhibited an initial discharge capacity of 138 mAh g^{-1}, achieving >99% coulombic efficiency after five formation cycles. When cycled at C/10, capacity retention remained above 85% over 50 cycles, and stable rate performance was observed up to C/2. These electrochemical metrics confirm the potential of CNF/LTO/PLA composites as viable candidates for lightweight, mechanically stable, and customizable 3D-printed electrodes. Beyond materials performance, this work demonstrates the feasibility of "one-shot" fabrication of battery components, wherein current collectors, electrodes, and supporting structures can be integrated in a single print. Such an approach minimizes assembly steps, reduces manufacturing waste, and enables the production of bespoke, on-demand energy storage devices. The insights gained from this research provide a foundational framework for the embedding of functional energy systems within 3D printed smart structures, advancing the vision of autonomous, structurally integrated, and sustainable electronic devices.

Keywords: Additive Manufacturing; 3D Printed Lithium-Ion Batteries; Electrochemical Energy Storage; Composite Electrodes; Carbon Nanofibers (CNF); Lithium Titanate (LTO); Polymer-Based Nanocomposites; Extrusion-Based Printing; Structurally Integrated Energy Systems; One-Shot Fabrication; Functional Polymers; Printed electronics.

Abstract (Italian)

La manifattura additiva (Additive Manufacturing, AM) offre una flessibilità di progettazione senza precedenti per i sistemi di accumulo elettrochimico dell'energia, consentendo architetture personalizzate e l'integrazione diretta di materiali funzionali all'interno di componenti strutturali. Tuttavia, l'applicazione dell'AM alle batterie agli ioni di litio è ancora in una fase iniziale, principalmente limitata da problematiche legate alla compatibilità dei materiali e ai processi di fabbricazione. Il presente lavoro affronta tali limitazioni mediante lo sviluppo e la caratterizzazione elettrochimica di elettrodi compositi stampati in 3D basati su LTO, nanofibre di carbonio (CNF) e PLA come matrice polimerica, con l'aggiunta di un plastificante biodegradabile finalizzato alla modulazione del comportamento reologico per processi di estrusione. È stato formulato un materiale di alimentazione stampabile contenente 52% in peso di LTO attraverso un'ottimizzazione reologica sistematica. Le miscele di PLA, plastificante e LTO sono state opportunamente regolate per ottenere viscosità idonee all'estrusione nell'intervallo 10^3–10^4 Pa·s a 180 °C, garantendo continuità del filamento e adeguata adesione tra gli strati durante la deposizione del materiale. Le misure di conducibilità elettrica eseguite su dischi compositi contenenti 4, 8 e 12% in peso di CNF hanno evidenziato una soglia di percolazione prossima all'8% in peso, alla quale la conducibilità elettronica aumenta bruscamente fino a valori dell'ordine di $\sim 10^{-1}$ S·cm^{-1}, senza compromettere la resistenza meccanica del filamento né la stampabilità. Tali risultati dimostrano che un contenuto bilanciato di CNF consente di ottimizzare simultaneamente il trasporto elettronico e l'integrità meccanica, requisito essenziale per materiali di accumulo energetico stampabili in 3D. Elettrodi di forma discoidale (diametro 15–18 mm, spessore 0,5 mm) sono stati stampati direttamente a partire dal filamento ottimizzato mediante una stampante a estrusione appositamente progettata e successivamente assemblati in celle semicella contro litio metallico. I test di ciclabilità galvanostatica a C/25 hanno mostrato una capacità di scarica iniziale di 138 mAh·g^{-1}, con un'efficienza coulombiana superiore al 99% dopo cinque cicli di formazione. A C/10, la ritenzione di capacità si è mantenuta superiore all'85% dopo 50 cicli, mentre una risposta stabile è stata osservata fino a C/2. Tali prestazioni elettrochimiche confermano il potenziale dei compositi CNF/LTO/PLA come candidati validi per elettrodi stampati in 3D leggeri, meccanicamente stabili e altamente personalizzabili. Oltre alle prestazioni dei materiali, questo lavoro dimostra la fattibilità della fabbricazione "one-shot" di componenti per batterie, in cui collettori di corrente, elettrodi e strutture di supporto possono essere integrati in un'unica fase di stampa. Tale approccio riduce le fasi di assemblaggio, minimizza gli scarti di produzione e consente la realizzazione di dispositivi di accumulo energetico personalizzati e on-demand. Le conoscenze acquisite forniscono un quadro di riferimento fondamentale per l'integrazione di sistemi energetici funzionali all'interno di strutture intelligenti stampate in 3D, contribuendo allo sviluppo di dispositivi elettronici autonomi, strutturalmente integrati e sostenibili.

Parole chiave: Manifattura additiva; Batterie agli ioni di litio stampate in 3D; Accumulo elettrochimico di energia; Elettrodi compositi; Nanofibre di carbonio; Titanato di litio; Nanocompositi polimerici; Stampa a estrusione; Sistemi di accumulo energetico integrati strutturalmente; Fabbricazione one-shot; Polimeri funzionali; Elettronica stampata..